Studies of Helium-rich and Hydrogen-deficient stars to explain their origin and evolution

A Thesis Submitted to

The Department of Physics

Pondicherry University, Puducherry - 605 014, India

For the Award of Degree of

Doctor of Philosophy

Submitted by

Anirban Bhowmick

Thesis Supervisor

Dr. Gajendra Pandey

Indian Institute of Astrophysics

Bengaluru - 560 034, India

December 2020

Title of the thesis	:	**Studies of Helium-rich and Hydrogen-deficient stars to explain their origin and evolution**
Name of the author	:	**Anirban Bhowmick**
Address	:	Indian Institute of Astrophysics II Block, Koramangala Bengaluru - 560 034, India
Email	:	anirban@iiap.res.in
Name of the supervisor	:	**Prof. Gajendra Pandey**
Address	:	Indian Institute of Astrophysics II Block, Koramangala Bengaluru - 560 034, India
Email	:	pandey@iiap.res.in

Declaration

I hereby declare that the material presented in this thesis, submitted to the Department of Physics, Pondicherry University, for the award of a Ph.D. degree, is a result of the investigations carried out by me at Indian Institute of Astrophysics, Bangalore, under the supervision of Professor Gajendra Pandey. The results presented herein have not been subject to scrutiny for the award of a degree, diploma, associateship or fellowship whatsoever, by any university or institute. Whenever the work described is based on the findings of other investigators, due acknowledgment has been made. Any unintentional omission is sincerely regretted.

Anirban Bhowmick
(Ph.D. Candidate)
Indian Institute of Astrophysics
2nd Block, Koramangala
Bengaluru 560 034
India
December 2020

Certificate

This is to certify that the thesis entitled **'Studies of Helium-rich and Hydrogen-deficient stars to explain their origin and evolution'** submitted to the Pondicherry University by Mr. Anirban Bhowmick for the award of the degree of Doctor of Philosophy, is based on the results of the investigations carried out by him under my supervision and guidance, at the Indian Institute of Astrophysics. This thesis has not been submitted in whole or part for the award of any other degree, diploma, associateship, fellowship, etc. of any other university or institute.

Prof. Gajendra Pandey
Thesis Supervisor
Indian Institute of Astrophysics
2nd Block, Koramangala
Bengaluru 560 034
India
December 2020

Dedicated to

Ma, Baba and Rony

Acknowledgements

First of all, I would like to express my sincere gratitude to my supervisor, Prof. Gajendra Pandey, for his continuous support and encouragement during my entire tenure of PhD. I am deeply indebted to him for introducing me to the exciting branch of Hydrogen-Deficient Stars and teaching me Observational Astronomy and Stellar Spectroscopy. He always encouraged me to work independently, while at the same time providing timely guidance whenever necessary. His positive approach towards a scientific problem and constructive feedback helped in shaping me as a researcher. Without his valuable insights and sincere efforts, this thesis wouldn't have been possible.

I am extremely grateful to Prof. David L. Lambert for his valuable comments and suggestions during my thesis, which improved my understanding of this subject. I especially thank Prof. Simon Jeffery, Prof. Geoffrey Clayton, Prof. Falk Herwig and Prof. N. Kameswara Rao for organizing the *Fourth Conference on Hydrogen Deficient Stars, HDEF4,* and giving me an opportunity to present my work and interact with the stalwarts of the field. I am grateful to the conference organizers for ensuring a comfortable and enjoyable stay in North Ireland. I especially thank K. Sriram for helping in the installation and running of SYNSPEC and TLUSTY. I thank Sriram, Raghubar, Sushmita and Avrajit for fruitful discussions on stellar spectroscopy. My heartfelt thanks to J.P. Ninan for helping me in NIR observations.

I sincerely thank my Doctoral Committee members Prof. T. Sivarani and Prof. V. V. Ravikanth, for their valuable suggestions regarding the improvement of my thesis. I would like to thank the Dean, School of Physical, Chemical & Applied Sciences, Pondicherry University (P.U.), Head of the Department of Physics, PU, and also staff members of P.U. for their help and cooperation during various occasions.

I am grateful to the Director, IIA, Prof. Annapurni Subramaniam, the Dean, IIA, Prof. G. C. Anupama, the Chairperson, Board of Graduate Studies (BGS), Prof U. S. Kamath, and members of BGS, for providing all the necessary research facilities and support required for my thesis work. I thank the former Directors of IIA, Prof. Sreekumar and Prof. Jayant Murthy, former Chairpersons of BGS, Prof. Aruna Goswamy, Prof. R. T. Gangadhara and Prof. Annapurni Subramaniam for their support in various academic matters. I thank the foreign travel committee of IIA for providing sufficient financial support for attending conferences.

I am thankful to the IIA observing facilities and the htac (HCT time allocation committee) members for providing me with the opportunity to obtain high-quality scientific data that led to my research publications. I thank all the observing staffs at CREST and IAO, Hanle for their dedication and support during observations. Many thanks to IIA library staff for helping me to access necessary books and journals. I thank IIA computing centre for their help in computer and network-related issues. I sincerely thank all the administrative staffs for their timely assistance in related administrative work. I specially thank K. Shankaranarayanan for taking care of the administrative affairs between Pondicherry and IIA. I am extremely grateful for all the support provided by IIA and Bhaskara staff during the coronavirus outbreak. I sincerely thank the Bhaskara supervisors, cooks and all the housekeeping staffs for taking care during my stay.

I want to thank the IIA Outreach Committee, for providing me with a platform to interact and teach basic physics and astronomy to high school students. I would specially thank Prasanna Deshmukh, Mayuresh, Sandeep, Nirmal, Phanindra and Megha for inspiring me to participate in many exciting outreach activities.

I sincerely thank all the teachers of IIA, IIT Guwahati, Presidency College, and my school teachers for inspiring me to follow my goals.

I thank all my wonderful friends in Bhaskara with whom I spent a wonderful time. I heartily thank my seniors Samyaday and Sajal for their guidance and inspiration. I would like to thank my roommates Samyaday, Pralay and Satabdwa for making my stay in Bhaskara comfortable. I thank my batchmates Megha, Dipanweeta, Chayan, Samrat, Snehalata and Tridib for making the coursework memorable and for supporting me throughout the entire duration of PhD. I cherish memorable footballing moments with Samrat, Chayan, Avinash, Souvik and Satabdwa. I thank my juniors Pralay, Amit and Satabdwa for making the environment lively. I will always remember the cheerful musical sessions with Chayan, Samyaday, Shubham, Megha, Samrat, Dipa, Sneha and Satabdwa. I am especially grateful to my friends Megha, Tanya, Avinash, Sneha and Samrat for giving me company and providing emotional support during the pandemic.

I heartily thank my M.Sc. batchmates at IIT Guwahati who gave me the confidence to pursue research in physics. I would specially thank Arghya, Banibrata, Tamal, Mangesh and Sandip for the enlightening discussions on different topics of physics which helped me in developing my physics concepts. I want to thank all my friends from school and college days who gave me the confidence to face the challenges. I would like to thank Ankur, Reet, Aritro, Sayantan, Saurav, Arijit, Souransu and Chitradeep for playing an important role in my life.

I do not have enough words to express my love and gratitude towards my family without whom I am nothing. I am extremely grateful to my parents, my dear Ma and Baba (Mrs. Lipika Bhowmick and Mr. Ashis Kumar Bhowmick) for believing in me and providing me unflinching support throughout my every step of life. Special thanks to my younger brother, Rony (Mr. Sandipan Bhowmick) for being a continuous source of joy in my life. Being an elder brother to you is the best thing that happened to me. I would also like to thank my uncle and aunt, Boromama and Chhotopishi (Mr. Swapan Kumar Saha and Mrs. Anuradha Saha) for your continuous support and prayers. Lastly, I want to thank Megha for being a constant pillar of support throughout the difficult times.

List of Publications

In International Refereed Journals

1. *Are DY Persei Stars Cooler Cousins of R Coronae Borealis Stars?*
Anirban Bhowmick, Gajendra Pandey, Vishal Joshi, & N. M. Ashok, 2018, **ApJ**, 854, 140 (8 pages)

2. *Detection of Fluorine in Hot Extreme Helium Stars*
Anirban Bhowmick, Gajendra Pandey, & David L. Lambert, 2020, **ApJ**, 891, 40 (18 pages)

Conference Proceedings

1. *Fluorine detection in hot Extreme Helium Stars*
Anirban Bhowmick, Gajendra Pandey, & David L. Lambert, 2020, in **JAA**, "Online special issue of the conference: *150yrs of the Periodic Table*" (In Press)

Under preparation

1. *Quantitative analysis of the Extreme Helium Star, V2205 Oph*
Anirban Bhowmick, Gajendra Pandey, 2020, in preparation

a

Abstract

The existence of hydrogen-deficient stars in a hydrogen-dominated universe in itself, sparks a considerable curiosity to explore their origin and evolution. Very rare in nature, the peculiar characteristics of these enigmatic objects suggest an evolutionary path very different from that of a normal star. However, due to the extreme rarity of these exotic objects, it is difficult to arrive at a definitive evolutionary history. A thorough knowledge about their chemical composition across the different samples of hydrogen-deficient stars enables us to tackle this issue. In this thesis, we mainly focus on finding an evolutionary connection between different groups of low mass, carbon-rich hydrogen-deficient stars through spectroscopic analyses of their observed spectra.

The low-mass, carbon-rich, hydrogen-deficient supergiants are divided into four groups − the extreme helium stars or the EHes, the R Coronae Borealis Stars or the RCBs, the hydrogen-deficient carbon stars or the HdCs, and the DY Persei variables. They span a wide range of effective temperature − from the coolest DY Persei variables ($T_{eff} \sim 3500$ K) to the hot extreme helium stars (EHes) ($T_{eff} > 14000$ K). Apart from hydrogen-deficiency, the majority of these stars are also characterized by peculiar chemical abundances connecting them in a common evolutionary sequence. The two most notable chemical peculiarities observed in these stars are (i) enhancement of ^{18}O with relative to ^{16}O and depletion of ^{13}C with respect to ^{12}C in the atmosphere of HdCs and cool RCBs (Clayton et al. 2007) and, ii) enrichment of fluorine (F) with respect to iron (Fe) by 800-8000 times than solar in the atmospheres of warm RCBs and cool EHes (Pandey 2006; Pandey et al. 2008). Based on the observed surface properties, two formation scenarios were proposed − 1) The Double Degenerate (DD) merger scenario involving the merger of two low mass double-degenerate white-dwarfs and, the 2) FF scenario involving a late or final He shell flash in a post-AGB star. However, the observed chemical

peculiarities favour the DD scenario. The status of these chemical peculiarities was not explored in cool DY Persei variables and hot EHes. Hence the main aim of this thesis is to investigate the evolutionary connection of the hot EHes and cool DY Persei variables with the rest of the group by exploring the chemical signatures pertaining to the abundance anomalies. If the abundance peculiarities are found to be common across the entire range – DY Persei, HdCs, RCBs and EHes, a common formation scenario can be finally established. Below, we briefly describe the studies undertaken.

In the first investigation, we perform a comparative, low-resolution NIR spectroscopic study on a sample of cool RCBs, HdCs, DY Persei variables and few DY Persei suspects with data obtained using TIRSPEC, mounted on 2m Himalayan Chandra Telescope (HCT). We obtain estimates of ^{12}C/^{13}C and ^{18}O/^{16}O from the relative strengths of the ^{12}C^{16}O, ^{13}C^{16}O and ^{12}C^{18}O molecular bands observed in the NIR K- band region. The results confirm high ^{12}C/^{13}C and ^{18}O/^{16}O ratios in the sample of RCBs and HdCs. Among the samples of DY Persei variables, a quartet including DY Persei itself shows isotopic ratios consistent with RCBs and HdCs indicating that DY Persei variables may be related to RCBs and HdCs in the sense of their evolution. However, high-resolution spectroscopic analysis on a larger sample of DY Persei variables is required for firmly confirming their status as the cooler counterparts of RCBs.

In the second study, we investigate the status of fluorine abundances in hot extreme helium stars (EHes) through high-resolution optical spectroscopic analyses. The spectroscopic data were obtained using HESP mounted on HCT and from ESO archives for ten hot EHes. Fluorine estimates were obtained using the F II lines in two windows centered at 3505 Å and 3850 Å . The results show that six of the ten stars have significant enhancement of fluorine similar to the cool EHes. Two carbon-poor hot EHes show no signature of fluorine and have a significant low upper limit for the F abundance. We find a surprising relation between F enrichment and the trend of N (nitrogen) with Ne (neon) abundances. Nevertheless, theoretical predictions suggest that Ne and F are both produced from N through different nucleosynthetic processes. However, while the observed Ne abundances suggest that Ne is a result of a complete conversion of N through successive α captures, the simultaneous enrichment of Ne and F without any visible depletion of N raises a need for further theoretical studies.

In the third project, we carry out an LTE abundance analysis of the high-resolution optical spectrum of the extreme helium star, V2205 Oph, obtained using HESP. Using a grid of LTE model atmospheres, we determine the atmospheric parameters of V2205 Oph: T_{eff} = 23900 ± 900 K, $\log g = 2.65 \pm 0.1$ (cgs) and ξ = 28 ± 2 kms^{-1}, from the imposition of ionization equilibrium of ion pairs such as C II/C III and N II/N III and using spectroscopic indicators like He I line profiles. We report chemical abundances of 12 elements from H to Fe, which agrees with previous determinations. By exploring the discrepancy of abundances determined from ionic pair of same species, we infer that ions of Si and S are heavily affected by departures from LTE. Hence, future studies using non-LTE abundance analysis of this star is recommended.

With the results obtained from observational spectroscopic studies dedicated mainly to two extreme members of the group, the cool DY Persei variables and the hot EHes, we successfully establish the evolutionary connection between the entire sequence of H-deficient supergiants − the DY Pers, the HdCs, the RCBs, the cool and hot EHes. Below, we mention a brief structure of the thesis.

In Chapter 1, we give a brief introduction to different groups of hydrogen-deficient stars. We discuss in detail the observed properties of the low mass hydrogen deficient stars and review the two proposed formation scenarios − the DD merger and the FF scenario, in light of the evolutionary sequence followed by H-normal, low and intermediate-mass stars. In Chapter 2, we discuss the spectroscopic observations, data acquisition, and processing techniques. In Chapter 3, we discuss about the investigation of ^{12}C/^{13}C and ^{18}O/^{16}O ratios in low-resolution NIR spectra of DY Persei variables. In Chapter 4, we report about the spectroscopic investigation of F abundances from high-resolution optical spectra of hot EHes. In Chapter 5, we discuss about the LTE abundance analysis of the hot EHe, V2205 Oph. In Chapter 6, we conclude and provide some future prospects.

Contents

Acknowledgements **i**

List of Publications **v**

Abstract **vii**

List of Figures **xv**

List of Tables **xxi**

1 Introduction **1**

- 1.1 Classification of H-deficient star groups: 2
  - 1.1.1 Population I and Massive Hydrogen-Deficient Stars: 2
  - 1.1.2 Low mass Hydrogen-Deficient Supergiants: 3
  - 1.1.3 H-deficient hot subdwarfs: 5
  - 1.1.4 H-deficient Central Stars of Planetary Nebulae: 6
  - 1.1.5 H-deficient white dwarfs with AM CVn binaries: 8
- 1.2 Characteristics of low-mass H-deficient supergiants: 8
  - 1.2.1 R Coronae Borealis Stars (RCBs) and cool Hydrogen-deficient Carbon Stars (HdCs): 9
  - 1.2.2 Extreme Helium Stars(EHes): 13
  - 1.2.3 DY Persei variables: 16
  - 1.2.4 Common chemical peculiarities and clues to their evolution: 18
- 1.3 Evolution of low and intermediate-mass stars. 19
- 1.4 Evolutionary scenarios of H-deficient supergiants: 27
  - 1.4.1 FF scenario: 28
  - 1.4.2 DD scenario: 30
- 1.5 Aim of this thesis: 33

2 Observations, data acquisition and processing **35**

- 2.1 Spectroscopy: 36
  - 2.1.1 Spectrograph: 36

2.1.2 Échelle spectrograph: 38
2.2 Facilities used: 39
2.2.1 Himalayan Chandra Telescope (HCT): 39
2.2.1.1 TIFR Near Infrared Spectrometer and Imager (TIRSPEC): 41
2.2.1.2 Hanle Échelle Spectrograph (HESP): 43
2.2.2 Archival Data: 44
2.2.2.1 FEROS: 44
2.2.2.2 UVES: 45
2.2.2.3 Robert G. Tull Coudé Spectrograph: 45
2.3 Observing Strategies: 46
2.3.1 Compatibility of scientific goal with instrument capability: . 46
2.3.2 Requirements for data processing: 47
2.3.2.1 Bias correction: 47
2.3.2.2 Dark correction: 48
2.3.2.3 Flat fielding: 48
2.3.2.4 Wavelength Calibration: 49
2.3.2.5 Sky substraction: 49
2.3.3 Data processing: 51
2.3.3.1 Data pre-processing: 51
2.3.3.2 Spectrum extraction and wavelength calibration: . 52
2.3.3.3 Continuum normalization: 53
2.3.3.4 Telluric correction: 53
2.4 Final Reduced science spectrum: 53

3 Are DY Persei stars cooler cousins of R Coronae Borealis stars? 55
3.1 Introduction 56
3.2 Observations and Reductions 59
3.3 CO bands and overview of the spectra 61
3.4 Preliminary results and discussion 61
3.5 Conclusions 68

4 Detection of flourine in hot Extreme Helium Stars 71
4.1 Introduction 72
4.2 Observation 74
4.3 Identification of F II lines 77
4.4 Abundance analysis 81
4.4.1 Fluorine enrichment 96
4.4.2 Fluorine and other elements 98
4.5 Double white dwarf mergers and the fluorine abundance 106
4.6 Concluding remarks 113

5 Quantitative analysis of the Extreme Helium Star, V2205 Oph 115

5.1 Introduction 116
5.2 Observation 118
5.3 Line identification 119
5.4 Quantitative Fine analysis 119
    5.4.1 Atmospheric parameters 121
    5.4.2 Chemical composition 128
5.5 Conclusion 141

6 Summary and Future prospects: 143

Bibliography 151

List of Figures

1.1 The latest light Curve of R Coronae Borealis with the characteristic rapid deep decline with slow recovery. Image courtesy: AAVSO (`https://www.aavso.org/`) 9

1.2 The light curve and photospheric absorption-line radial velocities of RCB during the 1995-96 decline. The light curve (lower panel) is constructed from visual observations kindly supplied by the American Association of Variable Star Observers (AAVSO). Radial velocities (upper panel) were presented for group A (filled circles) and group B (open squares) lines. Group A comprises of high-excitation weak lines of N I,O I,Al II and S I and group B consists of strong lines of C I, O I, Si II, Ca I, K I, Cr II and Ba II. Image courtesy: Kameswara Rao et al. (1999) 10

1.3 $\log g$ − T$_{eff}$ diagram of hot and cool EHes and majority and minority RCBs. Hot EHes are represented by blue solid squares, cool EHes by blue solid circles, majority RCBs by red solid triangles and minority RCBs by orange solid star symbols. Solid lines show the helium main-sequence, the horizontal branch and the dashed line shows the Eddington limit for pure Thomson scattering in a He atmosphere. The data has been collated from LTE analyses of RCBs and EHes taken from multiple sources as mentioned in Section-1.2.1 and Section-1.2.2 14

1.4 Light Curves of RCB (top panel) and DY Persei(bottom panel). RCB shows rapid asymmetric light declines with slow recovery whereas in DY Persei the decline and rise to maximum is more symmetric. Image courtesy: AAVSO (`https://www.aavso.org/` 17

1.5 Evolution of a $1M_{\odot}$ normal star in the Hertzprung-Rusell diagram(HR). Credit: Addison Wisley 19

1.6 Simplistic view of internal chemical structure of a low-mass star, through the major phases of stellar evolution–starting from the main-sequence in top progressing successively through the giant-branch, horizontal branch, asymptotic-giant branch and finally to the white-dwarf phase. Thick lines and filled circles represent nuclear-burning zones. Image courtesy: Simon Jeffery: Principles and Perspectives in Cosmochemistry (2010) . 24

1.7 Evolution of a $2M_{\odot}$ star from Herwig (2005) with different phases of evolution marked in different colours and labeled. The blue line traces the evolutionary path of a ‘born-again’ AGB after experiencing a final He-shell flash. 27

1.8 Illustration of formation for an RCB/EHe through DD merger scenario involving a CO-WD and a He-WD 31

2.1 Schematic diagram of a spectrograph. Image courtesy: *Illustration by George Retseck in `https://www.scientificamerican.com/`* 37
2.2 Schematic diagram of an échelle spectrograph. Image courtesy: *C.R. Kitchin in "Optical Astronomical Spectroscopy", CRC Press, 1995.* . . . 38
2.3 View of HCT. Image courtesy: `http://www.iiap.res.in/` 40
2.4 Design of TIRSPEC from Ninan et al. (2014) 42
2.5 Schematic ray diagram of HESP with marked components. Image courtesy: `http://www.iiap.res.in` 43

3.1 1.52−1.78 μm spectra of RCBs, HdCs, DY Persei, and DY Per affiliated stars. The band head positions of ^{12}C^{16}O ,^{12}C^{18}O and ^{13}C^{16}O and other key features are marked. The stars are ordered according to their increasing effective temperature (approximate) from bottom to top. 62
3.2 1.52−1.78 μm spectra of normal giants/supergiants of different spectral type ranging from K giants on the top to cool N type carbon stars at the bottom. The band head positions of ^{12}C^{16}O , ^{12}C^{18}O and ^{13}C^{16}O and other key features are marked. 63
3.3 2.25−2.42 μm spectra of RCBs, HdC, DY Persei, and DY Per affiliated stars , with wavelengths of ^{12}C^{16}O , ^{12}C^{18}O and ^{13}C^{16}O indicated by vertical lines. The stars are ordered according to their increasing effective temperatures (approximate) from bottom to top. The position of the mean continuum for each spectrum is indicated by the line marked. 64
3.4 2.25−2.42 μm spectra of normal giants of different spectral type ranging from K giants in the top to cool N type carbon stars in the bottom. As in Figure 3 ,wavelengths of ^{12}C^{16}O , ^{12}C^{18}O and ^{13}C^{16}O indicated by vertical lines. The position of the mean continuum for each spectrum is indicated by the line marked. 65

4.1 Comparison of the spectra with key identifications in 3505 Å region. The stars are arranged according to their effective temperature with hottest on the top and coolest at the bottom. The red lines represents the F II lines of RMT 3 in this window. 79
4.2 Comparison of the spectra with key identifications in 3850 Å region. The stars are arranged according to their effective temperature with hottest on the top and coolest at the bottom. The red lines represents the F II lines of RMT 1 in this window. 80
4.3 Observed F II in 3505 Å and 3850 Å wavelength windows of LS IV+6° 2 (solid line) with key lines marked. Synthetic spectra are shown for four fluorine abundanes. 84

4.4 Observed F II in 3850 Å wavelength window of V652 Her (solid line) with key lines marked. Synthetic spectra are shown for four fluorine abundanes. 85

4.5 Observed F II in 3850 Å wavelength window of V2205 Oph (solid line) with key lines marked. Synthetic spectra are shown for four fluorine abundanes. 86

4.6 Observed F II in 3505 Å and 3850 Å wavelength windows of DY Cen (solid line) with key lines marked. Synthetic spectra are shown for four fluorine abundanes. 87

4.7 Observed F II in 3505 Å and 3850 Å wavelength windows of HD 144941 (solid line) with key lines marked. Synthetic spectra are shown for four fluorine abundanes. 88

4.8 Observed F II in 3505 Å and 3850 Å wavelength windows of LSE 78 (solid line) with key lines marked. Synthetic spectra are shown for four fluorine abundanes. Note that the He I line at 3502 Å in the left panel of the above figure is not synthesized due to unavailability of log-gf values in NIST database 89

4.9 Observed F II in 3505 Å and 3850 Å wavelength windows of BD +10° 2179 (solid line) with key lines marked. Synthetic spectra are shown for four fluorine abundanes. 90

4.10 Observed F II in 3850 Å wavelength window of V1920 Cyg (solid line) with key lines marked. Synthetic spectra are shown for four fluorine abundanes. 91

4.11 Observed F II in 3505 Å and 3850 Å wavelength windows of HD 124448 (solid line) with key lines marked. Synthetic spectra are shown for four fluorine abundanes. 92

4.12 Observed F II in 3850 Å wavelength window of PV Tel (solid line) with key lines marked. Synthetic spectra are shown for four fluorine abundanes. 93

4.13 Observed F I in 6856 Å region of V1920 Cyg (solid line) with key lines marked. Synthetic spectra are shown for four fluorine abundances. . . . 94

4.14 Observed F I in 6856 Å region of LSE 78 (solid line) with key lines marked. Synthetic spectra are shown for four fluorine abundances. . . . 95

4.15 logϵ(F) versus logϵ(Fe) for hot EHes, cool EHes, and RCBs. The symbols representing different group of stars are showed. The encircled dot symbol represents the sun and the solid line represents locus of the solar F/Fe ratio. 97

4.16 Observed logϵ(F) versus logϵ(X) for EHes and RCBs from where X = C, N ,O and Ne respectively. The encircled dot symbol represents the sun. . 100

4.17 Observed logϵ(N) and logϵ(Ne) versus logϵ(Fe) for EHes and RCBs. The encircled dot symbol in each plot corresponds to solar value with the solid line giving the locus of solar ratio N/Fe ad Ne/Fe respectively . The dashed line in the plot of logϵ(N) vs logϵ(Fe) is the predicted nitrogen after full conversion of initial C, N and O to nitrogen in CNO cycle where initial O is determined from the relation of [α/Fe] vs [Fe/H] for normal disk and halo stars given by Ryde & Lambert (2004). The dotted line in the same plot is the predicted nitrogen due to conversion of inital C and N to nitrogen in the CN cycle. In the plot of logϵ(Ne) vs logϵ(Fe) the dot-dashed line gives the locus of initial neon values taken from the relation of [α/Fe] vs [Fe/H] for normal disk and halo stars (Ryde & Lambert 2004). In the same figure the dashed line is the locus giving of sum of initial C, N,O and Ne. 102

4.18 Observed logϵ(F) with [Zr/Fe] for EHes and RCBs. The encircled dot symbol represents the sun. 105

4.19 Comparison of the observed surface abundances of RCBs and EHes obtained from Jeffery et al. (2011), with the result of Lauer et al.'s MESA model A1. [X] represents logarithmic number abundances of an element X relative to solar. The symbols represent majority RCB (red stars), minority RCB (blue stars), and EHe (green stars). The black square in each panel is the abundance from model A1. The magenta symbols correspond to results from other sources in the literature: filled triangle and circle symbols correspond to results presented by Menon et al. (2013), plus symbols to results by Longland et al. (2011) and diamond symbols to results by Zhang et al. (2014). The figure is taken from Lauer et al. (2019). 108

5.1 LTE abundances from O II lines for V2205 Oph vs their reduced equivalent widths (log W_λ/λ). A microturbulent velocity of ξ = 28 kms^{-1} is obtained from this figure. 122

5.2 V2205 Oph's observed and synthesized LTE He I line profile at 4026 Å . In the left panel the LTE He I line profiles are synthesized for T$_{eff}$ = 24000 K for two different log g values. Similarly in the right panel the LTE He I line profiles are synthesized for T$_{eff}$ = 25000 K for two different log g – see key on both the panels. 124

5.3 V2205 Oph's observed and synthesized LTE He I line profile at 4387 Å . In the left panel the LTE He I line profiles are synthesized for T$_{eff}$ = 24000 K for two different log g values. Similarly in the right panel the LTE He I line profiles are synthesized for T$_{eff}$ = 25000 K for two different log g – see key on both the panels. 125

5.4 V2205 Oph's observed and synthesized LTE He I line profile at 4921 Å . In the left panel the LTE He I line profiles are synthesized for T$_{eff}$ = 24000 K for two different log g values. Similarly in the right panel the LTE He I line profiles are synthesized for T$_{eff}$ = 25000 K for two different log g – see key on both the panels. 126

5.5 $\log g$ – T_{eff} plane for V2205 Oph. Loci satisfying the ionization equilibrium are plotted–see the keys on the figure. The cross shows the adopted LTE atmospheric parameters, T_{eff} = 23900 ± 900 K, $\log g$ = 2.65 ± 0.1 (cgs), used in this study. 127

5.6 $\log g$ – T_{eff} plane for V2205 Oph with the cross showing the solution, T_{eff} = 22300 ± 1000 K, $\log g$ = 2.55 ± 0.2 (cgs) , obtained if Jeffery & Heber's (1992) procedure of including the ionization balance of Si II/Si IV and S II/S III lines is followed. The loci satisfying the ionization equilibrium are plotted–see the keys on the figure. 129

List of Tables

3.1 Log of observations of RCB and HdC stars as well as DY Persei and the DY Per affiliated stars. 57

3.2 Log of observations of normal cool giants selected from Jorissen et al. (1992); Tanaka et al. (2007) 59

3.3 Absorption depths of first overtone CO band heads and the estimated $^{16}O/^{18}O$ and $^{12}C/^{13}C$ ratios of RCBs, HdC and DY Per affiliate stars. 66

3.4 Absorption depths of first overtone CO band heads and the estimated $^{12}C/^{13}C$ ratios of normal and cool carbon giants. 67

4.1 Log of observations of the EHe stars. 75

4.2 Details of the spectra 76

4.3 F II lines from 3s − 3p and 3p − 3d transition array contributing to the spectra of the analysed stars. The F II lines used in abundance determinations are shown in bold. 78

4.4 Derived abundances of fluorine in hot EHes. 83

4.5 Elemental abundances of hot EHes. 98

5.1 Photospheric LTE Line Abundances with the Line's Measured Equivalent Width (W_λ) in mÅ for V2205 Oph for the adopted model, (T_{eff}, $\log g$, ξ) = (23900, 2.65, 28) 130

5.2 Comparison of stellar parameters and derived photospheric abundances from LTE analysis of V2205 Oph from different studies. . . . 138

Chapter 1

Introduction

Hydrogen (H), the most abundant element in the universe is a major constituent in the atmosphere of a star. Starting right from their birth to the end stages of their evolution, H is the primary source of energy powering the star. Most of the stars are composed of about 72% hydrogen, 27.0% helium(He) by mass, and a small fraction of all the other elements also called the trace elements. With the commonly accepted notion, that H is the most abundant element in the atmosphere of a star, it invokes a great deal of curiosity to know that, there exist a small group of fascinating stars which are *devoid of H!* In an H dominated universe, the existence of such H-deficient objects creates a lot of interest to uncover the governing stellar physics and causes of formation and evolution of these enigmatic stars.

The spectra of H-deficient stars are characterised by very weak or absent H-Balmer lines than commonly expected from H-normal stars with similar effective temperature and surface gravity. These stars are helium (He) rich with hydrogen being underabundant by about 10^6 times in their photospheres. This extraordinary composition was first discovered by Williamina Fleming in 1891 (Fleming 1891) noting that "the spectrum of υ Sgr is remarkable since the hydrogen lines are very faint and of the same intensity as the additional dark lines". Fifteen years later Ludendorff reported that the H-Balmer line, Hγ, is weak in R Coronae Borealis (RCB), one of the most extraordinary, well-studied variable stars at that time (Ludendorff 1906). Though initially there was a reluctance to accept H-deficiency in stars, with the pioneering studies by Berman (1935) on RCB, and Struve & Sherman (1940); Greenstein (1940) on υ Sgr firmly establish the idea that stars can be H-deficient. The discovery of helium by Lockyer (1868), assisted Popper (1942) to discover the first H-deficient, helium star HD 124448, having the presence of strong and sharp neutral helium (He I) lines with an absence of H I-Balmer lines. After years of extensive research and advent of large-scale spectroscopic surveys, today, there exist a plethora of diverse H-deficient stars in which helium and other nucleosynthetic products replace all or most of the hydrogen in their atmospheres. Based on Jeffery (2008a), H-deficient stars can be classified into following five broad groups.

1.1 Classification of H-deficient star groups:

1.1.1 Population I and Massive Hydrogen-Deficient Stars:

The *Wolf Rayet stars*, *He-rich B stars* or *Intermediate Helium Stars* and *H-deficient binaries* belong to this group.

First detected by Wolf & Rayet (1867) **Wolf Rayet (WR) stars** are massive stars that had undergone evolution due to extensive mass loss. Due to mass loss, they have lost most of their outer H-rich envelope, exposing the nuclear burning materials underneath. Their spectra are characterized by strong emission lines, arising from ionized atoms, including helium. Exclusively located in the spiral arms, OB associations, and young clusters suggests that they belong to the young massive star population. Based on their spectra, they can be broadly classified into two groups:- WN-type, whose spectra are dominated by ionised nitrogen lines and WC-type whose spectra are dominated by ionised carbon lines . Another separate class was identified from the WC-sequence in which the emission lines of ionised oxygen dominates emission lines of carbon resulting in C/O < 1. This group of stars are called WO-stars . About 230 are known in Milky Way (van der Hucht 2001), and hydrogen has been detected in half of the well analyzed WR stars.

He-rich B stars or Intermediate Helium Stars are chemically peculiar B-type main sequence stars characterized by strong and variable neutral He lines in the spectra. The observed He/H ratio suggests that the apparent He abundance varies in a period of 1-10 days. It is predicted that diffusion governs the surface abundance distribution. Both radiative and magnetic field plays a vital role to concentrate particular elements in the line-forming region at specific locations on the stellar surface (Hunger & Groote 1999). He-overabundance may be due to He-enriched spots. It is observed in one prominent member, σ Ori E; the helium anomaly is due to strong magnetic field, up to 10^4G inclined at an angle of 90° to the rotation axis. Drilling & Hill (1986) listed 24 such stars which can be further classified into slow and fast rotators.

Five **H-deficient binaries** of υ Sgr type, are known today: υ Sgr, KS Per V426 Car, V1037 Sco and BI Lyn (Jeffery et al. 1996; Jeffery & Aznar Cuadrado 2001). They show large radial velocity variations in orders of several tens of kms^{-1} with orbital periods ranging between 50 to 360 days. Their spectra are dominated by strong helium lines with emission in Hα and Hβ with possible evidence of pulsations. All these stars lying within 200 pc from the Galactic plane suggests that these systems belong to young Population I stars.

1.1.2 Low mass Hydrogen-Deficient Supergiants:

This group consists of *R Coronea Borealis stars (RCBs), Hydrogen-deficient carbon stars (HdCs), Extreme helium stars (EHes)* and *“Born Again” stars.*

R Coronae Borealis Stars or RCBs are F-G type, hydrogen-deficient supergiants which are identified by their extraordinary dimming in brightness at irregular intervals. Their light curves are characterised by sudden drop in brightness of more than 3 magnitudes in a matter of few days and very slow recovery to maximum light which takes months together. The occurance of these rapid dimmings are irregular in nature. Their spectra show weak or no H-Balmer lines and CH bands. It is characterised by strong C_2 swan bands indicating carbon enrichment. RCBs also show infrared excess due to warm dust shell around the star. Till date 117 RCBs are known in Milky Way and 30 in the Large Magellanic Cloud (Tisserand et al. 2020).

The class of non-variable carbon rich cool H-deficient stars are called **hydrogen-deficient carbon stars**, the HdCs. They are spectroscopically very similar to RCBs and share similar chemical composition (Warner 1967; Goswami et al. 2010; García-Hernández et al. 2009, 2010; Clayton et al. 2007; Clayton 2012).

Extreme helium stars or EHes are a rare class of low mass, A- and B-type supergiants, characterised by strong lines of neutral He but weak or no H. Spectroscopically very similar to warm RCBs, they generally show an overabundance of nitrogen (N), carbon (C) and in some cases oxygen (O) in their spectra. Just about 22 EHes are discovered in the Milky Way (Jeffery et al. 1996; Jeffery 2017) till date.

RCBs, HdCs and EHes, share many similarities. They are spectroscopically similar and share extraordinary chemical peculiarities. They also show the same kinematics belonging to the old stellar population, strongly concentrated towards the Galactic centre and does not share the Galactic rotation (Jeffery et al. 1987). Spectroscopic observations suggest they may share a strong evolutionary connection. More about the RCBs, HdCs and EHes are discussed later in Section-1.2 with emphasis on the observational signatures that may connect them in the same evolutionary sequence.

There are three known extraordinary stars – FG Sge, V4334 Sgr and V605 Aql which had undergone a rapid evolution from one corner of the Hertzsprung-Russell(HR) diagram to the other and back within a human lifetime. These stars are called the **"Born-again stars"**. All three of them, show H-deficiency in the spectrum . FG Sge, known as a hot white dwarf in the late 19th century, evolved into a cool supergiant in the late 20th century (van Genderen & Gautschy 1995)! V4334 Sgr commonly known as Sakurai's object (Asplund et al. 1997), evolved from a faint blue star in 1994 to a yellow supergiant two years later and finally in the year 1999 the star disappeared from sight in optical due to a thick dust shell around it (Duerbeck et al. 2000). Later radio measurements showed that star is towards a blueward evolution. V605 Aql underwent a rapid "red-giant excursion" similar to V4334 Sgr (Clayton & De Marco 1997; Clayton et al. 2006, 2013). Due to extreme timescales of evolution, these objects might disappear before proper identification and analyses and three such identifications in one century suggest they may not be rare.

1.1.3 H-deficient hot subdwarfs:

This group consists of *He-sdB stars*, *compact He-sdO stars* and *low gravity He-sdO stars.*

Helium rich subdwarf B stars (He-sdBs) are B-type subdwarfs showing He I lines with weak or no hydrogen in their spectra with a small He II/He I ratio. The H/He ratio covers a wide range indicating they are quite heterogeneous in composition (Naslim et al. 2010). As reported by Ahmad & Jeffery (2004), the double-lined binary PG1544+488 consists of two He-sdBs, the only known double-lined subdwarf binary system. About 50 He-sdBs are known.

Proper classification of **Helium rich subdwarf O stars** (He-sdOs) is difficult as they cover a range in two dex in surface gravity which translates to a range in luminosity-to-mass ratio, L/M (Drilling et al. 2003). The higher gravity or *compact He-sdOs* lie close to extreme horizontal branch/helium main sequence in the log$g$-T$_{eff}$ plane. They are therefore likely to be related to the He-sdBs. Their spectra are dominated by He I and He II with weak H I lines. Similar to the He-sdBs they have a range in surface abundances and exhibit binarity. Based on their carbon abundances, they can be further classified into two groups, carbon-rich and carbon-poor. Most of them are nitrogen-rich. Apart from single stars, there exist several composite binaries, among which, HE0301-3039 (Lisker et al. 2004) is a double He-sdO binary system similar to the double He-SdB system mentioned earlier.

Only 5 in number known so far, the *low gravity* He-sdOs are thought to be the next evolutionary stage of EHes and RCBs while they contract towards the white-dwarf cooling track. The first identification of low gravity He-sdO was obtained by Wolff et al. (1974) from the spectrum of BD +37°1977.

1.1.4 H-deficient Central Stars of Planetary Nebulae:

These group consist of very hot Central stars of Planetary Nebulae that are hydrogen deficient (Mendez 1991). Though they are evolutionary end stages of low mass post AGB stars their spectra are practically indistinguishable from the young and massive O and B type stars mostly, Wolf Rayet stars. They are usually classified according to their spectral signatures into following groups: *[WC], Of-WR(C), O(He)* and *PG1159* stars (Mendez 1991).

The spectra of **[WC] stars** are dominated by broad emission lines from, He I, II , C II - IV, N II, III and other light ions suggesting their similarity to the young and massive WC stars. Though spectroscopically similar to massive WC stars, they are compact and 10-100 times fainter than true Wolf-Rayet-WC stars. They are also characterised by the presence of a bright planetary nebulae formed at the end of their AGB phase, a path that massive Wolf-Rayet stars do not follow. One of the main difference between them is that in the $\log g$ − T$_{eff}$ plane, the young and massive Wolf-Rayet stars lie very close or beyond the classical Eddington limit hence characterised by unstable atmospheres with high mass loss rates whereas the Wolf-Rayet Central stars of Planetary Nebulae follow the stable low-mass stellar trajectory. They consist of both early-type and late-type stars. Though optically thick stellar winds act as a hindrance for effective temperature measurements, yet determinations whenever possible indicate surface temperatures ranging from 22000K -140000K.

The spectra of **Of-WR(C) stars** are dominated by strong C emission lines. The broad He II 4686 Å line is in strong emission whereas He II 4200 Å, 4541 Å are in absorption. Only 2 Of-WR(C) stars are known: Abell 30 and Abell 78 (Mendez et al. 1991).

Lying between [WC] and PG1159 stars, the spectrum of **O(He) stars** are characterized by pure He II absorption and C IV, N V and O VI in emission. Only four O(He)s are known among which two (K1-27 and LoTr4) have planetary nebula whereas the other two don't (Rauch et al. 1998). They don't show pulsations.

PG1159/O(C) stars are H-deficient stars in the transitional phase between the central star of a planetary nebula and hot white dwarf. Spectra is dominated by C, O and He absorptions (Green et al. 1986). They are detected with both the presence and absence of nebula. They are the hottest known stars with effective temperatures of more than 100000 K. Further inclusions in this group brought stars showing sharp emission lines, less broad absorption and no helium (H1504+65, Nousek et al. (1986)). H1504+065 is particularly remarkable because of its extremely high effective temperature of about 200000 K, with its surface completely devoid of He and H and dominated by a mixture of C and O with exceptionally high abundances of Ne and Mg (Werner et al. 2004). Some of them, including the prototype PG1159-035 shows complex pulsations.

1.1.5 H-deficient white dwarfs with AM CVn binaries:

First WD classifications were started following designation “D” introduced by Luyten (1945), followed by DO, DB, DG.. with DC to be used for continuous spectra. Today the classification scheme, which is introduced in Wesemael et al. (1993), is widely used. Around 80% of the known white dwarfs are hydrogen-rich; hence the name DA. **Non-DA WDs** show almost no H in their spectra. DO WDs are very hot helium-rich, with He II dominating the spectra. DB WDs are cooler He-line stars showing just He I lines. DC WDs have a featureless continuum spectrum. The other cool WDs devoid of both H and He but having spectral signatures are – DQ WDs showing strong features of carbon, and DZ WDs showing strong metallic lines.

One of the most exotic of binary stars, **AM CVn** systems are interacting compact WDs in a binary with periods in the range of 5 - 65 min. Some of the spectacular features observed in these objects include photometric variations with periods different to the orbital period with spectra sometimes dominated by broad absorption lines (AM CVn prototype) and in some cases emission lines of He I, HeII (ES Cet). HM Cnc (Ramsay et al. 2002) an AM CVn binary has the shortest known orbital period with P_{orb} = 321 s. They differ from usual cataclysmic variables as in these systems the transferred material impacts directly on the stellar surface. Interesting questions do remain; whether these systems will eventually merge and give rise to an RCB star or a gamma-ray burst? (Solheim 1996, 2010)

1.2 Characteristics of low-mass H-deficient supergiants:

The main scope of this thesis is dedicated to the study of low mass H-deficient supergiants to understand their origin and evolution. Hence we now discuss in

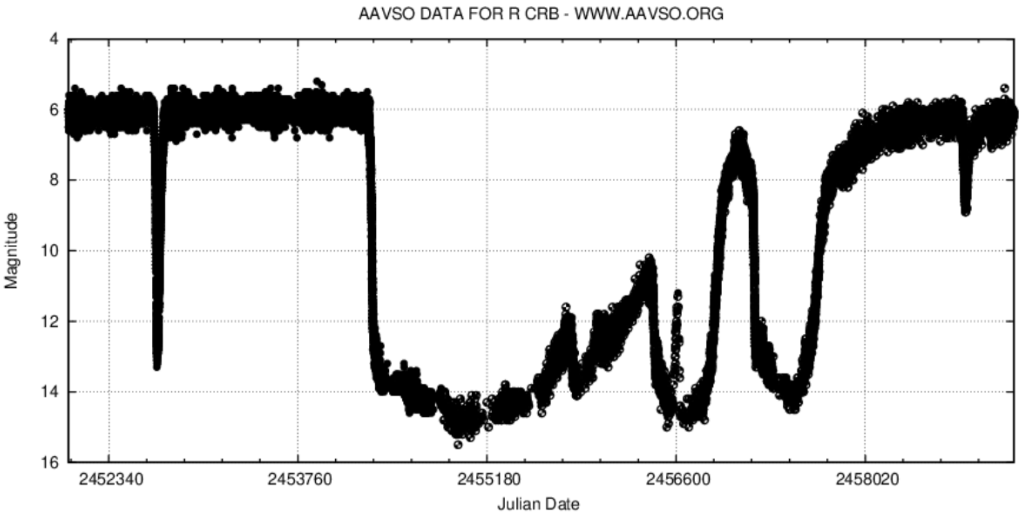

FIGURE 1.1: The latest light Curve of R Coronae Borealis with the characteristic rapid deep decline with slow recovery. Image courtesy: AAVSO (`https://www.aavso.org/`)

detail, the main characteristics observed in these group of stars with the possible evolutionary scenarios resulting in their formation.

1.2.1 R Coronae Borealis Stars (RCBs) and cool Hydrogen-deficient Carbon Stars (HdCs):

One of the most puzzling, variable supergiants are the F-G type, hydrogen-deficient RCB stars. They are dust-producing, post-AGB, carbon-rich supergiants characterized by hydrogen-deficiency and dramatic light variability. After staying in uniform brightness for months or years, they experience a sudden drop in brightness of more than three magnitudes in a matter of few days, followed by a prolonged recovery to maximum light taking months, sometimes years together. For, e.g. the decline of RCB itself, as shown in the given figure, Fig.1.1, it suffered a light decline of seven magnitudes in less than 100 days and stayed in deep decline for almost 2000 days. This erratic light decline results due to formation of carbon dust along the line-of-site at unusual intervals which was proved by the detection of infrared (IR) excess, from near-IR to far-IR wavelengths, in RCBs (Feast et

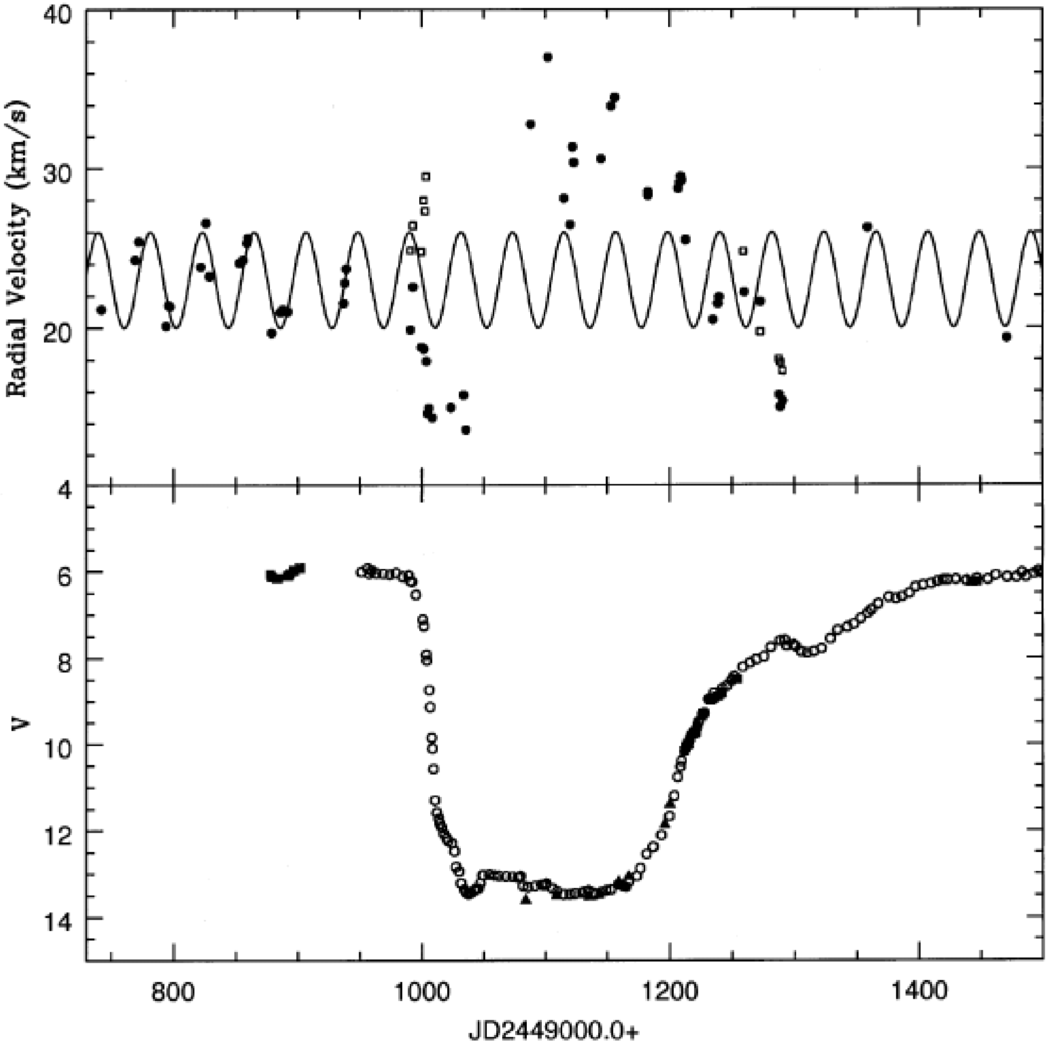

FIGURE 1.2: The light curve and photospheric absorption-line radial velocities of RCB during the 1995-96 decline. The light curve (lower panel) is constructed from visual observations kindly supplied by the American Association of Variable Star Observers (AAVSO). Radial velocities (upper panel) were presented for group A (filled circles) and group B (open squares) lines. Group A comprises of high-excitation weak lines of N I,O I,Al II and S I and group B consists of strong lines of C I, O I, Si II, Ca I, K I, Cr II and Ba II. Image courtesy: Kameswara Rao et al. (1999)

al. 1997). These stars also show semi-regular small-amplitude light and radial velocity pulsations (see Figure- 1.2 with periods of 40-100 days (Percy et al. 2004; Kameswara Rao et al. 1999).

Finding the accurate abundances of H-deficient RCBs is not straightforward due to its atmosphere being H-deficient and showing curious chemical abundances. As explained by Asplund et al. (2000), one of the major complications in the abundance analyses of RCBs, is the presence of *'carbon problem'*. RCBs being H-deficient, their atmospheres are dominated by helium and carbon. For these cool H-deficient stars, the principal source of opacity arises due to continuous absorption from highly excited levels of neutral carbon atom (C I). Now, since many absorption lines of C I arise from marginally lower excited levels, the predicted strength of weak C I lines would be independent of the adopted carbon abundance for stars with similar effective temperature and surface gravity. This fact is supported by observations; where similar strengths of C I lines are observed for RCBs but the strength of other metal lines varied from star to star (Rao & Lambert 1996). However, it was found that the predicted equivalent widths of weak C I lines is a factor of 0.6 dex stronger than the observed (Asplund et al. 2000); for example, model atmospheres computed for a C abundance of 9.5 (equivalent to a C/He ratio of 1%) return a C abundance of 8.9 from the measured equivalent widths of the observed weak C I lines. This mismatch between predicted and observed strengths of C I lines defines the 'carbon problem'. Hema et al. (2012) explored the carbon problem for C_2 swan bands for a sample of cool RCBs and HdCs. Their findings reveal that in contrast to the C I lines, the carbon abundances from C_2 bands do not depend on the adopted C/He ratio of the model atmosphere and the carbon problem can be can be compensated by choice of C/He $< 0.3\%$ for RCBs and 0.1% for HdCs. They do suggest that such a choice of low C/He creates an RCB - EHe mismatch due to EHes having higher observable C/He, and a change in temperature structure of the theoretical atmospheres might resolve the carbon-problems of both C I and C_2. However, Asplund et al. noted, this 'carbon problem' does not affect the elemental abundance ratios, which can be used as clues to explore RCB surface composition.

The principal features of RCB spectra as observed in maximum light (Clayton 1996; Asplund et al. 2000; Alcock et al. 2001; Clayton et al. 2007; Pandey et al.

2008; García-Hernández et al. 2009, 2010; Hema et al. 2012; Hema et al. 2017) can be summarized as follows:

- Extreme H-deficiency, though few RCBs show significant H in their spectra; like V854 Cen. H abundance anti-correlated with iron (Fe) abundance, the metallicity.
- Dominance of C I lines. In RCBs, cool enough to show molecular bands, spectra are dominated by strong absorption bands of C_2; CN bands are present but not strong. The spectra of warm RCBs are dominated by neutral atomic lines, with no Balmer lines, weak He lines and very weak or not detectable molecular bands.
- Extreme abundance ratios mainly high Si/Fe and S/Fe are observed in few of the RCBs. These RCBs having severe enrichment of Si and S relative to Fe are also classified as *minority* RCBs.
- N is surely enriched and Al/Fe, Na/Fe, Ni/Fe exceed solar values.
- Enrichment of s-process elements in some RCBs.
- High values of $^{12}C/^{13}C$ (> 50) observed in most of the RCBs. This is in sharp contrast to the low $^{12}C/^{13}C$ values (~ 4) observed in most of the AGBs.
- High enhancement of ^{18}O relative to ^{16}O such that $^{16}O/^{18}O < 1$ in the cool RCB atmospheres, whereas the observed value of $^{16}O/^{18}O$ is 500 in the solar neighbourhood and 200 in the interstellar medium(ISM).
- Severe fluorine (F) enrichment relative to Fe by a factor 800-8000 times in atmospheres of warm RCBs.
- High lithium (Li) abundance in four RCBs.

With the spectacular light curves and peculiar chemical composition, identification of RCB variables are comparatively easy. Several large-scale photometric and spectroscopic surveys have resulted in an increase of the number of known RCBs from about 50 to about 150 in just a decade (Jeffery 2008a; Tisserand et al. 2020). The growing number of RCBs enable us for a better understanding of this enigmatic variables.

HdCs are the spectroscopic counterparts of cooler RCBs. The term HdCs were explicitly used for non-variables but very similar to RCBs. Only 5 HdCs – HD 137613, HD 182040, HD 175893, HD 148839, HD 173409 (Jeffery et al. 1996) are identified till date, and as they do not possess extraordinary light variation, chances of identification from large surveys are low. HdCs having similar spectra like RCBs also share the abundance anomalies, most notably, high values of ^{12}C/^{13}C and a very high enhancement of ^{18}O. The similar chemical compositions, as well as abundance anomalies, point out clearly that they may be connected in the sense of stellar evolution.

1.2.2 Extreme Helium Stars(EHes):

As mentioned earlier, EHes are low mass A- and B-type H-deficient supergiants showing strong neutral lines of He in their spectra. They have effective temperatures in the range of 8000-35000K. They are highly luminous, with most of them having log(L/M) $>$ 4.0 (see Figure-1.3) lying close to the Eddington limit. However, few of them have log(L/M) $<$ 3.5. Their Galactic distribution, metallicities, the distances and radial velocities, point to an old spherical population concentrated to the Galactic Centre (*bulge population*), (Jeffery et al. 1987). After the discovery of 1st EHe, HD124448 by Popper in 1942, only 21 EHes were reported by Jeffery et al. (1996) until recently, when an additional EHe was discovered by Jeffery (2017). With the galactic surveys for luminous blue stars complete to about B=12 for the Milky Way and for galactic b = $\pm 30^\circ$ and l = $\pm 60^\circ$ (Drilling & Bergeron 1995; Drilling 1996), the detection of so few EHes, which are supposed to be at constant luminosity, suggest that the undetected EHes would either be

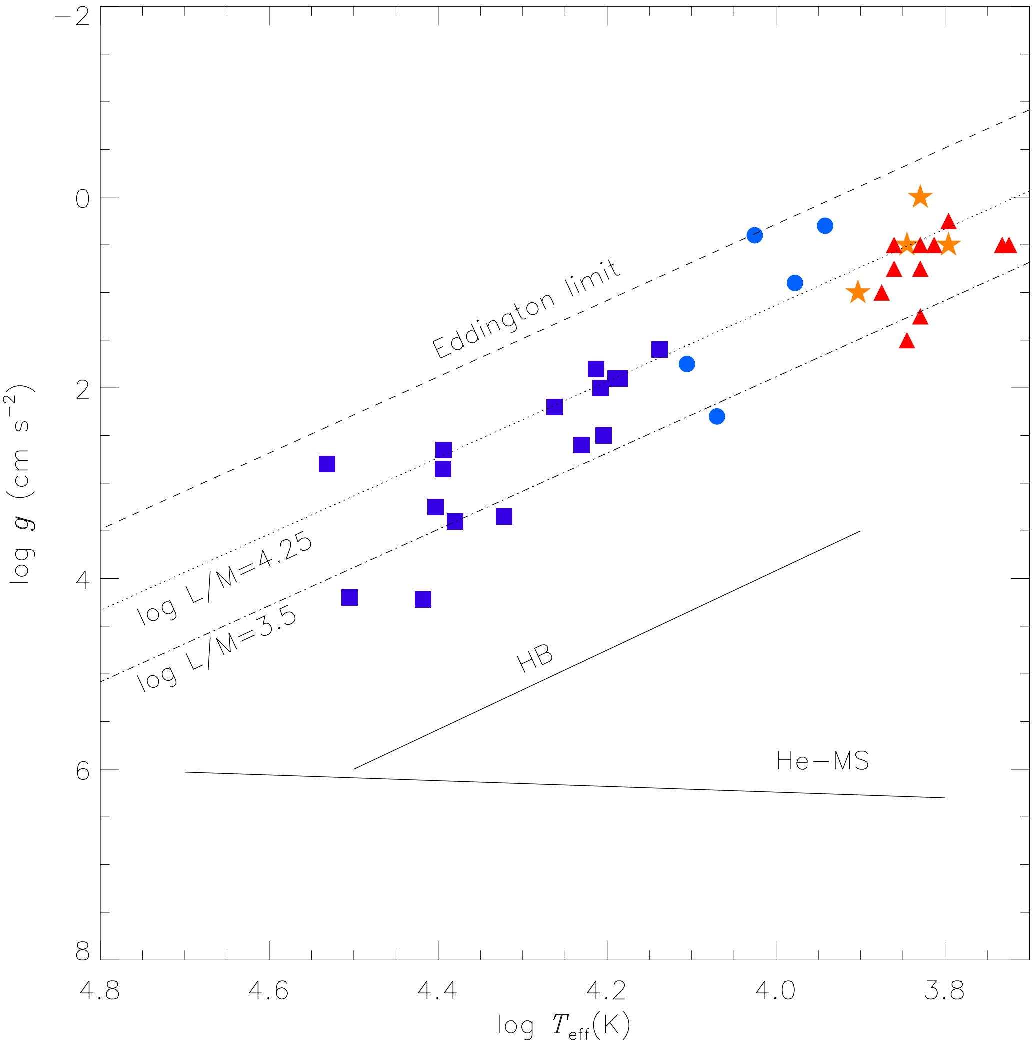

FIGURE 1.3: $\log g$ − T_{eff} diagram of hot and cool EHes and majority and minority RCBs. Hot EHes are represented by blue solid squares, cool EHes by blue solid circles, majority RCBs by red solid triangles and minority RCBs by orange solid star symbols. Solid lines show the helium main-sequence, the horizontal branch and the dashed line shows the Eddington limit for pure Thomson scattering in a He atmosphere. The data has been collated from LTE analyses of RCBs and EHes taken from multiple sources as mentioned in Section-1.2.1 and Section-1.2.2

fainter than B=12 or would be heavily obscured by the central bulge. EHes have a range in effective temperatures with T_{eff} ranging from 9000K to about 35000K. EHes having $T_{eff} < 14000$K are classified as cool EHes (Pandey et al. 2001) and the rest as hot EHes. None of the observed EHes show binarity (Jeffery 2008b, 2017; Jeffery et al. 2020).

The observed chemical composition of EHes suggest an H-deficient atmosphere with materials exposed to both H-and He-burning. Extensive abundance analyses has been carried out in optical and UV mainly using LTE, (Jeffery & Heber 1992; Jeffery 1993; Jeffery & Heber 1993; Jeffery 1998; Pandey et al. 2001, 2006; Pandey, & Reddy 2006; Pandey 2006; Pandey et al. 2004); with some non-LTE analysis (Pandey & Lambert 2011; Pandey et al. 2014; Pandey & Lambert 2017; Kupfer et al. 2017). The spectroscopic analyses revealed the following exciting features that are detailed below:

- H is a trace element in most of the EHes.
- N is overabundant, and the observed N matches with the N predicted from the complete conversion of initial C and N to N or initial C, N, and O to N during H-burning through the CNO cycle.
- Except two-C poor EHes, C is generally enhanced suggesting fresh production of C through triple-α process during He burning.
- O is enriched in most of the EHes suggesting ^{12}C+ α and/or 14N + α product through He burning. Though in some EHes, O scales with initial metallicity.
- Overabundance of Ne suggesting enrichment through 14N + 2α reaction through He burning.
- s-process (Y, Zr) enhancement in some EHes.
- Mg, Si, S scales with initial metallicity.

- High F overabundance relative to Fe in several cool EHes similar to warm RCBs.
- P is overabundant relative to Fe.

Apart from the above listed traits, several EHes are also characterized by the presence of small amplitude light and radial velocity pulsations. They can be clubbed into three major groups, the V652 Her, the FQ Aqr and the V2076 Oph variables (Jeffery 2014). V652 Her and BX Cir belong to the first group characterized by low amplitude light and radial velocity variations with a regular period of a few hours. They undergo radial pulsations driven by the κ mechanism through Z-bump instability. The cooler EHes having quasi-periodic low amplitude pulsations over 5-30 days are the FQ Aqr variables. Here, the radial pulsations are driven by strange-mode instability. The hotter EHes showing low-amplitude quasi-periodic light variations over 0.5 - 5 days belong to the last group of the V2076 Oph variables. One of the interesting features in the V2076 Oph variables is that, apart from light variation, they also exhibit line profile variability in their spectra suggested non-radial pulsations. The non-radial g-mode pulsations are driven by strange mode instability.

Severe enrichment of processed material suggests that these stars are at very late stages of their evolution. Such surface abundances with curious chemical peculiarities beg for a novel formation theory that must be able to explain the co-existence of all of these products including the observed small amplitude light and radial velocity pulsations.

1.2.3 DY Persei variables:

Their is another class of peculiar cool carbon stars thought to be H-deficient, of which DY Persei is the prototype, resembling closely with the RCBs (Alksnis

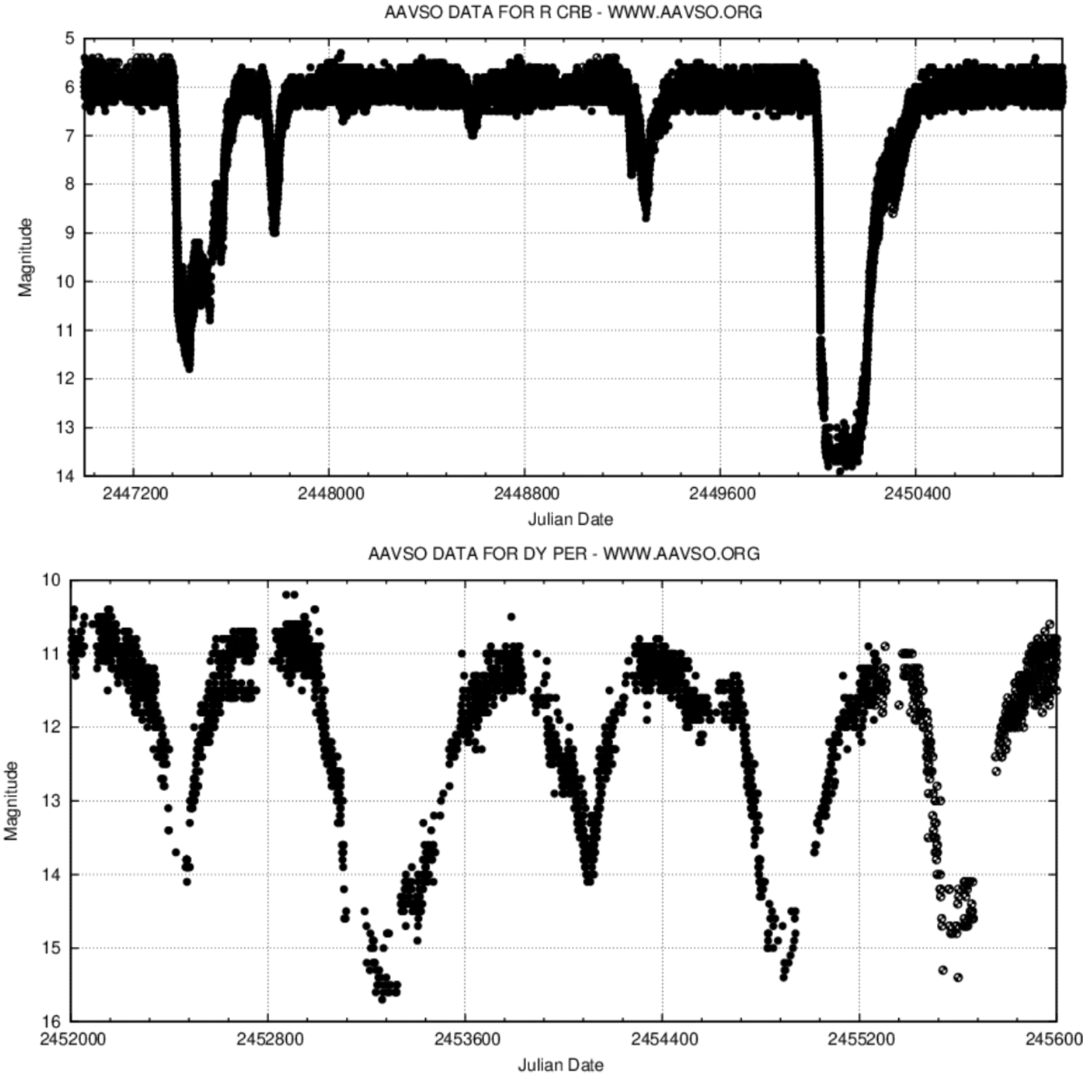

Figure 1.4: Light Curves of RCB (top panel) and DY Persei(bottom panel). RCB shows rapid asymmetric light declines with slow recovery whereas in DY Persei the decline and rise to maximum is more symmetric. Image courtesy: AAVSO (`https://www.aavso.org/`

1994). The DY Per light curve is characterized by deep declines at irregular intervals but they differ from RCBs due to their comparative slow rate of decline with a more symmetrical rise in time (see Fig.1.4) (Alcock et al. 2001). They also show some IR excess, with somewhat warmer circumstellar shells than RCBs (Tisserand et al. 2009). DY Persei variables are significantly cooler than RCBs with $T_{eff} \approx$ 3500 (Keenan & Barnbaum 1997). They may appear H-deficient due to absence of hydrogen Balmer lines in their spectra. However, the status of H-deficiency is yet to be confirmed, due to the absence of flux in the G band of CH at 4300 Å region (Keenan & Barnbaum 1997; Začs et al. 2007; Yakovina et al. 2009) owing to their cooler effective temperatures. Strong carbon features dominate the spectra with relatively high $^{12}C/^{13}C$ ratio. However, the estimates of $^{12}C/^{13}C$ ratios are mixed in the overall identified sample of Galactic and Magellanic DY Persei variables. There are only seven known Galactic DY Per stars with 27 in the Magellanic clouds (Tisserand et al. 2009, 2013). Due to such a small sample of known DY Persei variables, it is difficult to classify these stars and investigate any possible connection with the RCBs. However, due to their characteristic light curves, ongoing surveys are able to detect a growing number of new DY Persei candidates. With the increasing number of DY Persei variables available for analyses, it becomes easy to classify them and look for possible connections with RCBs or with normal carbon stars.

1.2.4 Common chemical peculiarities and clues to their evolution:

It can be inferred from above, apart from H-deficiency, these low mass H-deficient supergiants share some extreme abundance anomalies which may suggest their possible evolutionary connection. These include high values of $^{12}C/^{13}C$ ratios shared by HdCs and RCBs, enhancement of ^{18}O in HdCs and cool RCBs, and finally severe enrichment of F in warm RCBs and cool EHes. Such common chemical peculiarities surely hint towards an evolutionary connection between HdCs, RCBs and cool EHes. To explore the possibility of an evolutionary connection with this group, for other similar H-deficient star groups, for, e.g. hot EHes or cool DY Persei variables, estimates of these abundance anomalies play a very vital role. If the nature of the chemical peculiarities is found to be common across the entire sequence of DY Per, HdCs, RCBs, and EHes, primarily a sequence of increasing effective temperature, then a common formation scenario is highly probable.

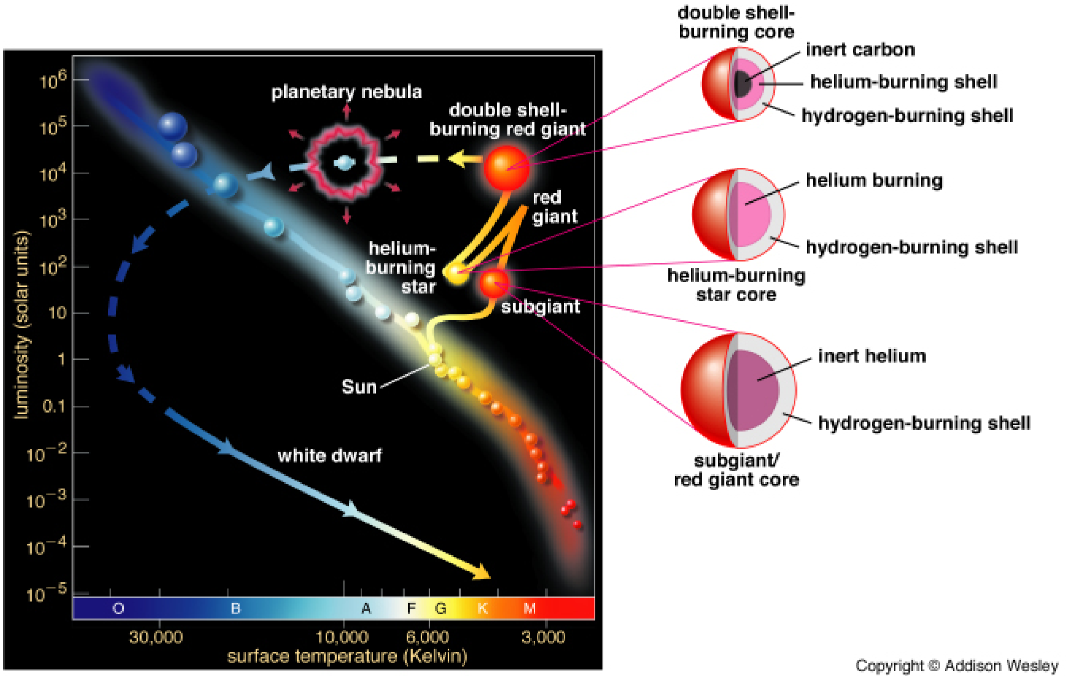

Copyright © Addison Wesley

FIGURE 1.5: Evolution of a $1M_{\odot}$ normal star in the Hertzprung-Rusell diagram(HR). Credit: Addison Wisley

The primary question that arises in the studies of these H-deficient stars is *how does this H-deficiency occur? At which stage of stellar evolution, the star might lose a substantial amount of hydrogen from its atmosphere and appear H-deficient?* For investigating this problem, a thorough knowledge about the evolution of a normal star single as well as in a binary is necessary. Again, the position of these hydrogen-deficient stars in the $\log g - \mathrm{T}_{eff}$ plane strongly suggest their progenitors are low to intermediate-mass stars. Hence, we will briefly discuss the evolutionary processes of normal, low to intermediate-mass stars.

1.3 Evolution of low and intermediate-mass stars.

According to Iben & Renzini (1983), the low and intermediate-mass stars are classified as stars having an initial mass between 0.8 to 8 $M_{\odot}$. Low mass stars have initial mass in the range of 0.8 to 2.3 $M_{\odot}$ whereas intermediate-mass stars have initial masses in the range of 2.3 to $8M_{\odot}$.

All the single stars spend most of their lifetime in the evolutionary phase known as *Main Sequence (MS)*. In this phase through nuclear fusion, hydrogen is converted to helium in the core of the star. A low-mass star will spend about 10^{10} years on the main sequence whereas an intermediate-mass star of $5M_\odot$, the main-sequence lifetime is 10^8 years (Bowers & Deeming 1984). As all the stars spend most of their lifetimes in this evolutionary phase, hence, the region in the Hertzsprung-Russell (HR) diagram representing the main sequence phase is most populated. Depending on the star's mass and core temperature, nuclear fusion of hydrogen to helium takes place through two different processes: PP chain and CNO cycling. PP (proton-proton) chain takes place in the stars having mass less than 1.3 $M_\odot$ (Salaris & Cassisi 2005) having a lower central temperature. The CNO(Carbon-Nitrogen-Oxygen) cycling is more dominant in stars having a mass greater than 1.3 $M_\odot$ having a higher central temperature.

PP-chain

$$^1_1\mathrm{H} + {}^1_1\mathrm{H} \rightarrow {}^2_1\mathrm{H} + e^+ + \nu_e$$

$$^2_1\mathrm{H} + {}^1_1\mathrm{H} \rightarrow {}^3_2\mathrm{He} + \gamma$$

$$\swarrow \; \searrow$$

$$^3_2\mathrm{He} + {}^3_2\mathrm{He} \rightarrow {}^4_2\mathrm{He} + {}^2_1\mathrm{H} \qquad {}^3_2\mathrm{He} + {}^4_2\mathrm{He} \rightarrow {}^7_4\mathrm{Be} + \gamma$$

(PP I)

$$\swarrow \; \searrow$$

$$^7_4\mathrm{Be} + e^- \rightarrow {}^7_3\mathrm{Li} + \nu_e \qquad {}^7_4\mathrm{Be} + {}^1_1\mathrm{H} \rightarrow {}^8_5\mathrm{B} + \gamma$$

$$^7_3\mathrm{Li} + {}^1_1\mathrm{H} \rightarrow 2{}^4_2\mathrm{He} \qquad {}^8_5\mathrm{Be} \rightarrow {}^8_4\mathrm{Be} + e^+ + \nu_e$$

(PP II)

$$^8_4\mathrm{Be} \rightarrow 2{}^4_2\mathrm{He}$$

(PP III)

CNO cycle

a. $^{12}_{6}\mathrm{C} + ^{1}_{1}\mathrm{H} \rightarrow ^{13}_{7}\mathrm{N} + \gamma$

$$^{13}_{7}\mathrm{N} \rightarrow ^{13}_{6}\mathrm{C} + e^{+} + \nu_{e}$$

$$^{13}_{6}\mathrm{C} + ^{1}_{1}\mathrm{H} \rightarrow ^{14}_{7}\mathrm{N} + \nu$$

$$^{14}_{7}\mathrm{N} + ^{1}_{1}\mathrm{H} \rightarrow + ^{15}_{8}\mathrm{O} + \gamma$$

$$^{15}_{8}\mathrm{O} \rightarrow ^{15}_{7}\mathrm{N} + e^{+} + \nu_{e}$$

$$^{15}_{7}\mathrm{N} + ^{1}_{1}\mathrm{H} \rightarrow ^{12}_{6}\mathrm{C} + ^{4}_{2}\mathrm{He}$$

b. $^{15}_{7}\mathrm{N} + ^{1}_{1}\mathrm{H} \rightarrow ^{16}_{8}\mathrm{O} + \gamma$

$$^{16}_{8}\mathrm{O} + ^{1}_{1}\mathrm{H} \rightarrow ^{17}_{9}\mathrm{F} + \gamma$$

$$^{17}_{9}\mathrm{F} + ^{17}_{8}\mathrm{O} + e^{+} + \nu_{e}$$

$$^{17}_{8}\mathrm{O} + ^{1}_{1}\mathrm{H} \rightarrow ^{14}_{7}\mathrm{N} + ^{4}_{2}\mathrm{He}$$

In the CNO cycle − C, N and O act as catalysts in the conversion of H to He. The N abundance is enhanced at the cost of C and O. Hence the total sum of CNO nuclei remains the same throughout the cycle. The reaction also increases the abundance of ^{13}C, and the CN-cycle equilibrium ratio of $^{12}\mathrm{C}/^{13}\mathrm{C}$ reaches a value of 3.4. This ^{13}C acts as a neutron source and hence plays a vital role in the latter stages of stellar evolution and nucleosynthesis. Since the nuclear-processed material is not mixed in the outer atmosphere, thus, the photosphere of an MS star has the same initial composition as it acquired during birth.

Even after the formation of the complete helium core, the central temperature is not sufficient enough to trigger He fusion. Hence due to continuous depletion of nuclear-fuel, i.e. H, the radiation pressure cannot balance gravity, triggering gravitational collapse and contraction of the He core. This, in turn, heats up the contracting helium core and the surrounding shell of hydrogen around it. It results in the fresh nuclear fusion of hydrogen in the shell, releasing more energy output (i.e. luminosity) than in the MS phase. The fresh hydrogen-burning in the shell, transfers energy to the outer layers of the star, causing it to expand. This expansion causes cooling down of the surface. This phase of the evolution of the star experiencing a subsequent increase in luminosity and a decrease in effective surface temperature is called *Red Giant phase.* It is depicted in the HR diagram (see Fig.1.5) by the track moving right and upward from the main sequence phase and is known as *Red Giant Branch* (Iben 1974). During this phase, the radius of the star expands 10 to 100 times its original size. During the ascent of the red giant branch due to expansion and subsequent cooling, higher rates of ion recombination happen, increasing the opacity. High energy generation with high opacity results in energy transfer by convection. The convection zone extends inwards till the deeper layers of hydrogen shell burning. This allows mixing of by-products of hydrogen fusion via CNO cycling with the outer atmosphere, resulting in a change of composition of the photosphere. This process is known as *First Dredge Up* (FDU). Due to the mixing of CNO cycled products, there is an increase in the photospheric abundance of ^{14}N and ^{13}C, decreasing the ^{12}C/^{13}C and ^{12}C/^{14}N abundance ratios (Iben 1974).

The evolutionary path of the collapsing core depends on the initial mass of the star. The collapsing He core consists of a mixture of He nuclei and electrons. Due to core contraction, there is sufficient rise in density such that lowest electron energy levels are filled, and the electrons are forced into higher energy levels. This gives rise to electron degeneracy pressure which prevents further gravitational collapse of the core, and the core becomes degenerate. This degeneracy of the helium core at the tip of the RGB phase is experienced by all low mass stars having mass less than about $1.8M_{\odot}$ (Herwig 2005). Once the core becomes degenerate, rapid heating occurs until the central temperature reaches 10^8K, which is sufficient enough for igniting helium fusion via the $triple-\alpha$ process.

Triple-α process

$$^{4}_{2}\mathrm{He} + ^{4}_{2}\mathrm{He} \rightarrow ^{8}_{4}\mathrm{Be}$$

$$^{8}_{4}\mathrm{Be} + ^{4}_{2}\mathrm{He} \rightarrow ^{12}_{6}\mathrm{C} + \gamma$$

The temperature rise in the degenerate core favours higher rates of nuclear reactions which in turn increases the temperature rapidly until the degeneracy is lifted. Thus, core He ignition in all low mass stars is a thermonuclear runaway, which is also known as *helium core flash* in which a large amount of helium fuses to carbon in a matter of few seconds. In more massive stars, the collapsing core reaches central temperatures sufficiently high enough for He ignition, before it gets the density to be degenerate. Hence core He burning proceeds steadily without producing any helium flash. This stage of evolution involving core He fusion is called *Horizontal Branch* (HB), characterized by near-constant luminosity. As the core He burns, the core contracts and to maintain hydrostatic equilibrium, the stars shrink in radius, ensuring almost constant luminosity with a rise in temperature.

With time helium gets depleted in the core leaving behind He-burning ashes (carbon and oxygen) in the core. Subsequently He fusion switches from the core to the surrounding He shell. At this point, the star consists of a carbon-oxygen core, a surrounding helium-burning shell, a He rich intershell region, a dormant hydrogen-burning shell and a large hydrogen-rich envelope in the outer part of the star (see Fig.1.6). Due to He shell burning, and subsequent energy transfer to the outer layers of the star, there is again an expansion and cooling, very similar to the red-giant phase. This stage of evolution is known as the *Early Asymptotic Giant Branch* (E-AGB) phase (Herwig 2005). The atmosphere of the star becomes convective again resulting in mixing of nucleosynthetic products from the deeper layers with the outer H-rich envelope. The mixing in this phase is known as *Second Dredge Up* (SDU) that alters the surface composition of the star. This phase is more prominent in an intermediate-mass star.

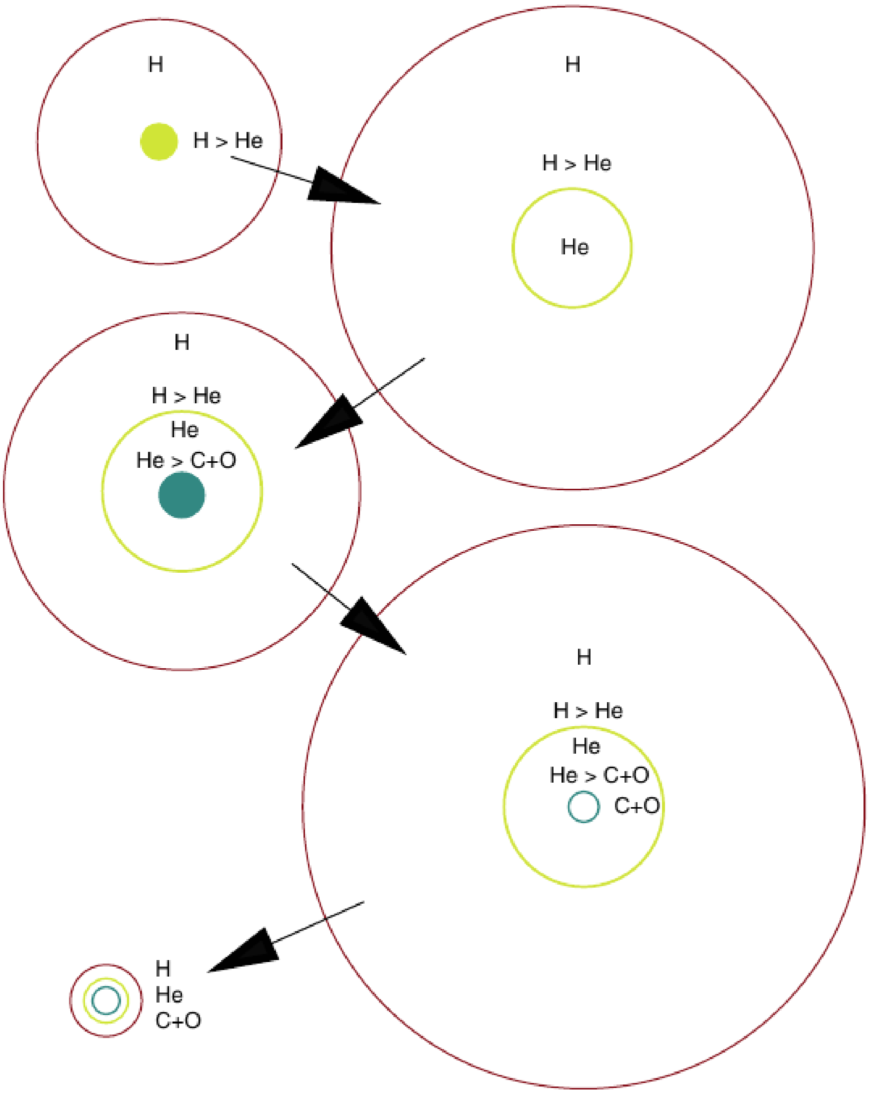

FIGURE 1.6: Simplistic view of internal chemical structure of a low-mass star, through the major phases of stellar evolution–starting from the main-sequence in top progressing successively through the giant-branch, horizontal branch, asymptotic-giant branch and finally to the white-dwarf phase. Thick lines and filled circles represent nuclear-burning zones. Image courtesy: Simon Jeffery: Principles and Perspectives in Cosmochemistry (2010)

Once the helium burning is exhausted in the shell, hydrogen burning re-ignites in the outer shell, marking the beginning of *Thermally Pulsating AGB* (TPAGB) (Herwig 2005) phase (see Fig.1.7). In this phase, the star experiences a series of thermal pulses due to episodes of thermonuclear runaway undergone by the inner He-shell. The H-burning in the shell gradually deposits freshly synthesized He in the He-rich intershell region. After a certain time when the amount of He reaches the *critical mass* it ignites explosively − a phenomenon called *helium shell flash.* The explosive He-shell ignition happening in non-degenerate conditions transfers all the energy for heating the surrounding layers. This causes rapid expansion and subsequent cooling of the above layers, shutting off the outer H-shell burning. A strong convection zone is established. Nearing the end of this thin He-shell burning, as the fusion nears the H-shell, due to high temperatures, H-burning reignites in the shell, and the cycle continues. Due to the thermal pulses and the presence of strong convection zones, there is significant mixing of the photosphere of the star with the freshly synthesized nuclear burning products from both H- and He-shell burning, changing the stellar surface composition altogether. All the mixing events following the thermal pulses are called *Third Dredge Up* (TDU). The TDUs are usually deepest and even circulates material of the core to the surface. The TDUs result in enrichment of the stellar atmosphere with nuclear burning products like He, C, N, O and the *s-process* elements. During the thermal pulse, the mixing of remnants of H-burning shell into He-burning shell results in the formation of free neutron sources. In case of low mass AGBs, the injection of ^{13}C, an end product of H-burning through CNO cycle, into the He-burning shell, results in the production of neutrons via the reaction $^{13}\mathrm{C}(\alpha,\mathrm{n})^{16}\mathrm{O}$. Similarly for more massive AGBs, ^{22}Ne, a result of successive α capture on ^{14}N, acts as a major neutron source via the reaction $^{22}\mathrm{Ne}(\alpha,\mathrm{n})^{25}\mathrm{Mg}$ (Iben & Renzini 1983). These free neutrons are captured by the Fe-seed nuclei often accompanied by a β-decay, a process known as *slow neutron capture or s-process*, giving rise to light and heavy s-process elements like Yttrium (Y), Zirconium (Zr), Strontium(Sr), Barium(Ba) etc.

The initial mass of the star again determines whether the AGB star will be C -rich or N- and O- rich stars. Lower mass AGBs (M $\leq$ 4 $M_{\odot}$) become C-rich (C/O $\geq$ 1) as fresh *triple*-α processed carbon(^{12}C) is pumped up to the surface. More massive AGBs (M > 4 $M_{\odot}$) experience a phenomenon known as *hot bottom burning* (HBB) which makes them O-rich or N-rich stars. In the massive stars, the convection zone can extend till the region of fresh nucleosynthesis where the fresh CNO cycle converts much of the primary carbon into nitrogen. This reduces C abundance in the envelope, and hence the AGB becomes N-rich or O-rich (C/O < 1) (Lattanzio & Forestini 1999; García-Hernández et al. 2013).

The thermal pulses in the AGB stage are responsible for star's massive mass-loss. The mass-loss rate which increases towards the end of AGB phase proceeds at a rate of $10^{-7} - 10^{-4}$ $M_{\odot}$ yr^{-1}. The heavy mass-loss through high-velocity stellar winds results in the formation of dusty envelope around the star. During the end of the AGB phase, most of the outer H-rich envelope is ejected. As the inner hot zones of nucleosynthesis approach the thinning photosphere, the effective surface temperature shoots up by about 10^5K at a constant luminosity. This period of evolution is called the *Post AGB* phase. Soon the temperature of the surface gets sufficiently high enough to ionize the ejected circumstellar material via UV radiation. The ionized, ejected, circumstellar material is known as *Planetary Nebulae*, which slowly dissipates in the interstellar medium (ISM). The planetary nebulae are rich in heavier elements that were synthesized in the interiors of the stars. Hence it plays a vital role in the chemical evolution of the galaxy, by mixing these elements into the ISM (Kwok 2000).

The hot central star (comprising of thin He- and H-shells around the degenerate CO-core) starts to cool down after nuclear burning has ceased. Due to the absence of a nuclear source, the star shines dimly through heat radiation. These end-stage stellar remnants are called *White-Dwarfs* (WD) which finally fades away after all the heat energy is radiated.

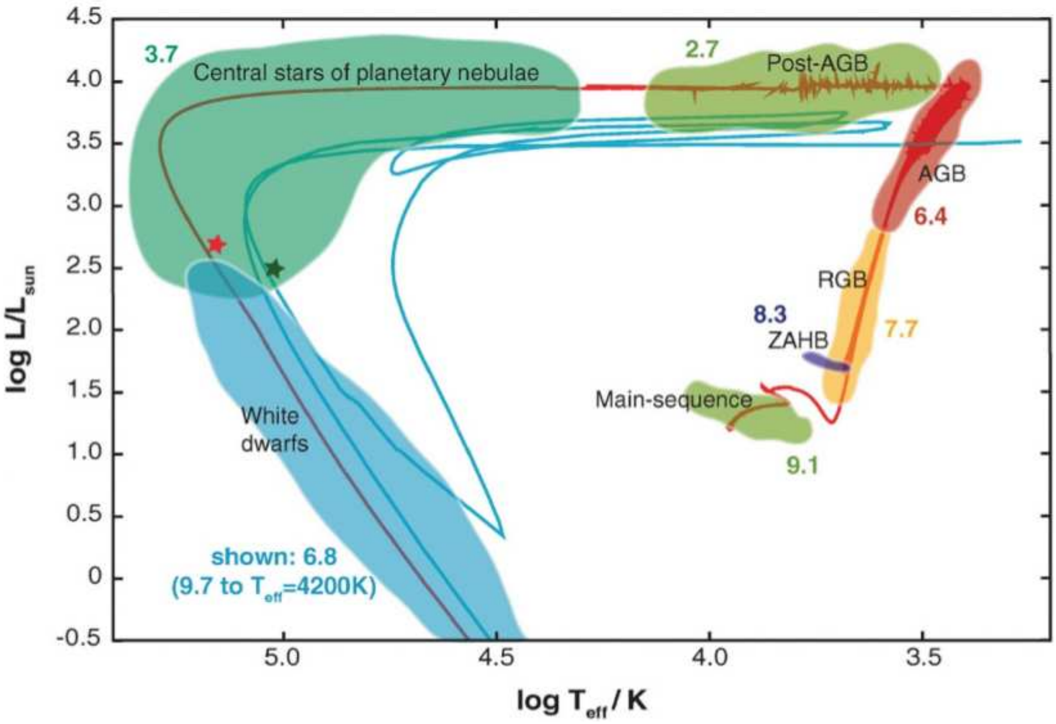

FIGURE 1.7: Evolution of a $2M_\odot$ star from Herwig (2005) with different phases of evolution marked in different colours and labeled. The blue line traces the evolutionary path of a 'born-again' AGB after experiencing a final He-shell flash.

1.4 Evolutionary scenarios of H-deficient supergiants:

From the evolutionary processes as described above, it is clear that a low or intermediate-mass star remains H-rich even till the end phases of their lives. Only in the TP-AGB phase, the star has a possibility of becoming H-deficient by loosing H-rich outer envelope, through mass-loss events. Yet, loosing the entire H-rich envelope, while maintaining the characteristics and dimension of a supergiant is a question that perplexed astronomers for decades. In addition to the H-deficiency, the observed chemical peculiarities in these stars necessitated out-of-the-box evolutionary scenarios explaining their formation. Two evolutionary scenarios that stood out the test of rigorous observational and theoretical analysis for decades are the *final flash* (FF) scenario and the *double-degenerate merger* (DD) scenario.

1.4.1 FF scenario:

In the FF scenario (Iben et al. 1983) a single star evolving into PN phase or post-AGB phase, on the white dwarf cooling track, experiences a *final helium shell flash* and the resulting heat baloons the star to a supergiant size (Fujimoto 1977; Renzini 1979). The ignition of the helium shell in the post-AGB phase results in what is known as late or *Very Late Thermal Pulse* (VLTP) (Herwig 2001) resulting in ingestion of the thin H-rich outer envelope making the star appear H-deficient. Predicted to occur in 20% of all AGB stars (Clayton 2012), the ingestion of the surface hydrogen during the final flash, release sufficient energy to inflate the star to supergiant dimensions for a brief period of time. The expansion is followed by cooling of the surface, resulting in the star moving up-right in the HR diagram and appearing as AGB star again for a second time in its course of evolution (see Fig.1.7). Hence, these stars are called *born again AGBs.* Three well known 'born-again AGBs' observed to undergo FF outbursts transforming them into hydrogen-deficient supergiants are Sakurai's Object (Asplund et al. 1997; Pavlenko et al. 2004), V605 Aql (Clayton & De Marco 1997; Lundmark 1921; Clayton et al. 2006), and FG Sge (Gonzalez et al. 1998).

Limitations of FF scenario:

Though the predicted abundances shortly after the outburst might appear similar to that observed in RCB stars, yet there are key differences. Renzini (1990) predicted Li-production in FF scenario during ingestion of H-rich envelope through the Cameron-Fowler mechanism (Cameron & Fowler 1971). Along with Sakurai's Object, some RCB stars do show enhanced Li abundances (Lambert 1986; Asplund et al. 1998) and according to Herwig & Langer (2001), the Li enhancements appear consistent with the FF scenario. Yet Li enhancement is not common across the majority of RCB/HdC stars. Apart from that, there are certain chemical peculiarities observed in the majority of RCBs and HdCs, that cannot be satisfactorily explained by FF scenario.

- In FF scenario, due to ingestion of H-rich layer and operation of the CNO cycle, there is a fresh production of ^{13}C reducing the ^{12}C/^{13}C ratio. Presence of enhanced ^{13}C is confirmed in the born-again star, Sakurai's Object, having ^{12}C/^{13}C $\sim$ 4, (Pavlenko et al. 2004; Hema et al. 2012) which is similar to the CNO equilibrium value. Since most of the RCBs have ^{12}C/^{13}C $\geq$ 100, FF scenario fails to account for their abundances. However, few RCBs do show detectable ^{13}C in their atmospheres (Rao & Lambert 2008; Hema et al. 2012).
- FF scenario cannot explain the enhanced ^{18}O as observed in atmospheres of the cool RCB and HdC stars (Clayton et al. 2007). According to Warner (1967), ^{18}O is produced by α capture on ^{14}N (the dominant ash of H burning) $-$ ^{14}N(α,γ)^{18}F(β^+,ν)^{18}O. However, higher temperature for prolonged periods, as observed in FF scenario results in the destruction of ^{18}O via ^{18}O(α,γ)^{22}Ne (Clayton et al. 2007). Even if an alternate condition for ^{18}O overproduction exist, during the ingestion of the H-rich layer ^{18}O will be efficiently destroyed by proton capture. Hence they don't predict ^{18}O overabundance in FF scenario. This is confirmed by the absence of detectable ^{12}C^{18}O bands in IR in Sakurai's object (Eyres et al. 1998).
- As reported by Pandey et al. (2008), Sakurai's object doesn't show enhancement of F. However, enhancement of F is another important chemical peculiarity observed in the atmosphere of hot RCBs and EHes Pandey (2006); Pandey et al. (2008). F depletion is actually predicted in final flash(FF) objects due to the same reason mentioned as above. High temperature due to helium shell flash will lead to the complete conversion of ^{14}N to ^{22}Ne, reducing ^{14}N and destroying ^{18}O, the suspected seed for F overproduction (Menon et al. 2013; Clayton et al. 2007).

- FF scenario cannot satisfactorily explain the observed low C/He ratio ($\approx$ 1% by number) in EHes and RCBs. In the FF scenario the predicted C/He ranges around 30% (Schönberner 1996; Iben & MacDonald 1995; Herwig et al. 1999).

Apart from the failure to explain the key abundance anomalies, the observed surface composition in evolved FF object, like V605 Aql ($\sim$ 55% He $\sim$ 40% C), is similar to those seen in central stars of PNe rather than RCBs or EHes (C/He $\sim$ 1%) (Clayton et al. 2006). Though the surface abundances of Sakurai's object resembles that of RCBs (Asplund et al. 1998), there are indications that it is evolving along a similar path as V605 Aql (Hajduk et al. 2005; Clayton et al. 2006). Though the enhancement of Li in few RCBs supports FF scenario, the detection of enhanced F in the majority of these stars effectively rules out FF scenario (Pandey et al. 2008). Even when the atmosphere of FF objects resembled an RCB star, their evolutionary time scales were too short to account for even the small number of known RCB stars in the Galaxy.

1.4.2 DD scenario:

Introduced by Webbink (1984) and Iben & Tutukov (1984), the DD merger scenario, involves the merger of a pair of low mass degenerate white dwarfs (WD) in a close binary system. Merger events in a binary system take place after orbital decay due to gradual loss of angular momentum via gravitational wave radiation. In the DD scenario, the double degenerate (DD) WD binary system should be close enough (a period of two hours or less) such that a merger is possible within a Hubble time. The principal version involves a merger of a He-WD with a more massive CO-WD. In the less favoured version mergers involve two He WD (Zhang & Jeffery 2012b). They indicate that production of RCB and EHe stars via the He+He channel may be 1470 times smaller than from the CO+He channel.

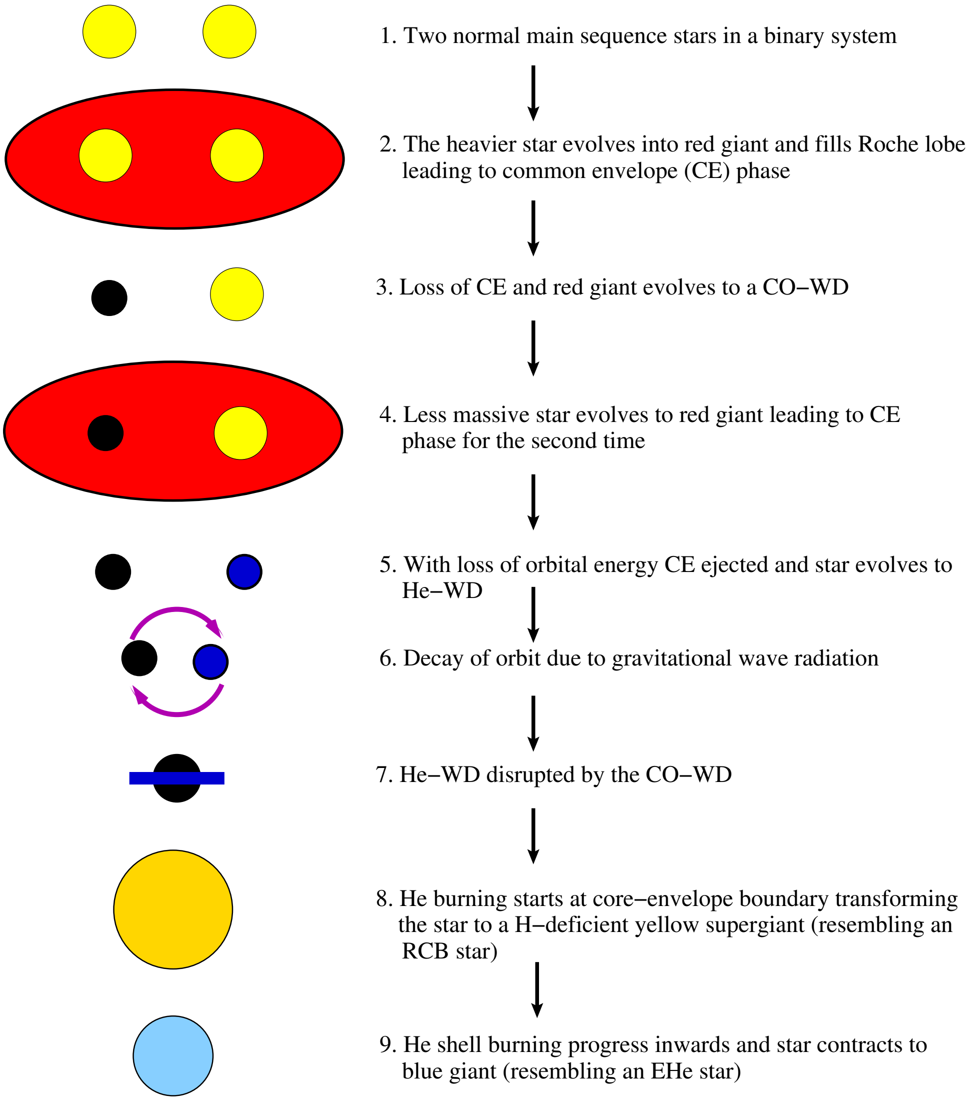

FIGURE 1.8: Illustration of formation for an RCB/EHe through DD merger scenario involving a CO-WD and a He-WD

In the binary system, starting with two main-sequence stars, the more massive star evolves first into red-giant phase and fills its Roche Lobe, leading to common envelope (CE) phase via unstable mass transfer. Roche Lobe is a region around a star in a binary system within which the material is bound to the star by gravity. With friction and subsequent loss of orbital energy and hence, a decay of the binary orbit the common envelope is ejected, and massive star evolves into a CO-WD. The less massive star evolves into a red giant leading to another CE, resulting in further shrinking of orbit. The successive CE phases are necessary to reduce the orbit sufficiently enough for the merger to take place within a Hubble time. The lower mass star will evolve into He-WD. Note that isolated He-WD will take more than a Hubble time to form, however, formation of He-WDs in a binary system is possible in less than a Hubble time - observed He-WDs are found always in a binary (Althaus & Benvenuto 1997; Zhang & Jeffery 2012c). As the orbit of the system decays due to gravitational-wave radiation, the He-WD fills its Roche Lobe and starts transferring mass to the CO-WD. In the process, the He-WD is finally disrupted by tidal forces in a matter of few minutes and engulfed by the CO dwarf. The system consists of a CO-WD core with a hot corona inside a rapidly rotating disk, with the disrupted He-WD being the principal contributor to both the corona and the disk (Menon et al. 2013). He-rich material is accreted by the CO-WD at a rate of $10^{-5}M_{\odot}\text{yr}^{-1}$. With enough He-accretion, He-shell burning initiates causing the star to expand and cool to supergiant dimensions. The structure, with a He burning shell and extended hydrogen-deficient envelope, resembles an RCB/HdC star (Clayton 1996). He-shell burning around the CO WD core is stable and maintains the star as a supergiant for a considerable amount of time $\sim 10^5$ years (Iben 1990). He-burning proceeds outwards gradually thinning the outer envelope resulting in an increase of surface temperature and the star evolves horizontally blueward at a constant luminosity in the HR diagram resembling an EHe star (see Fig.1.8).

The final product of the merger depends on the mass and composition of the participating WDs. If the total mass exceeds the Chandrasekhar limit of 1.4 $M_{\odot}$, the merger will explode as a Supernova Ia instead of evolving into a hydrogen-deficient supergiant. With a plethora of calculations on DD mergers, it is well established that the merger products can account for the observed surface abundance of an RCB/EHe star (Saio & Jeffery 2002; Clayton et al. 2007; Pandey et al. 2006, 2008; Pandey & Lambert 2011; Longland et al. 2011; Jeffery et al. 2011; Menon et al. 2013; Zhang et al. 2014; Menon et al. 2019; Lauer et al. 2019) . Apart from that, the chemical peculiarities like enhanced ^{18}O in the atmosphere of cool RCBs and HdCs, enhanced F in warm RCBs and cool EHes, absence of ^{13}C, are somewhat successfully explored by the above references predicting DD merger abundances. While the observed surface composition of carbon-rich RCBs/HdCs/EHes are well accounted by CO+He WD merger models, Zhang & Jeffery (2012a) showed that He+He WDs mergers could explain the exceptional C-poor EHes. Though a lack of clarity might remain regarding the nature of episodes of nucleosynthesis taking place during the merger or post-merger phases, giving rise to such peculiar chemical composition, yet it is not in doubt that the DD merger scenario is currently the most acceptable theory regarding origin and evolution of an RCB/HdC/EHe star.

1.5 Aim of this thesis:

The principal aim of this thesis is to understand the origin and evolution of the H-deficient supergiants. However, due to the extreme rarity of these exotic H-deficient stars a conclusive formation and evolutionary history is difficult to establish without a thorough knowledge about their chemical composition. Abundance anomalies if present, play a vital role in classifying these enigmatic objects. Since the status of the chemical peculiarities were not available for the two extreme groups, the cooler DY Persei variables and the hot EHes, hence we mainly focussed in exploring the existance of possible abundance anomalies in these two groups. The main motivation for my thesis can be divided into two broad aspects:

- to look for presence of ^{18}O in the cool DY Persei variables and subsequent comparison of their observed ^{16}O/^{18}O and ^{12}C/^{13}C ratios with those of the HdCs, the cool RCBs alongwith the hydrogen normal cool carbon stars. The status of ^{16}O/^{18}O and ^{12}C/^{13}C ratios in DY Persei variables would throw a significant light about their closest relatives, whether they have a evolutionary connection to hydrogen-deficient HdCs and RCBs or whether they are more similar to hydrogen normal cool carbon stars.

- to detect and estimate fluorine (F) abundances in hot EHes in order to investigate the evolutionary connection between the hot EHes with its counterparts– the cool EHes and the warm RCBs for which enhanced F has been previously reported. The abundance estimates of F in hot EHes, if present, would build a strong platform for establishing their evolutionary history by comparison with the predicted F abundances for different theoretical formation scenarios.

Chapter 2

Observation, data acquisition and processing

An overview

To explore the secrets of the universe, astronomical observations played a very crucial role from time immemorial. To have an idea about the evolution of our universe, the knowledge about the composition of the celestial objects, their formation history becomes essential. Stellar spectroscopy is a very important tool that helps us to unravel these secrets. Through spectroscopy, we can determine the composition of a star, the processes leading to the formation of elements in the periodic table, and hence, investigating the driving forces and events that shaped our origin and evolution.

The study in this thesis is mainly based on extensive use of stellar spectroscopic observations and techniques. In this chapter, we describe low and high resolution spectroscopic observations, data acquisition, and processing techniques.

2.1 Spectroscopy:

Stellar spectroscopy involves the study of absorption and emission lines arising in the spectrum of a star. The absorption lines occur when the photons coming from the hotter interior of the star get absorbed in their cooler atmospheres. These absorption lines are a unique fingerprint of the element causing them, as the discrete energy levels of transitions for the atoms of a particular element are unique. The strength of the absorption feature also gives an idea about the relative proportion of that particular element in the stellar atmosphere.

These lines can be detected and analyzed by splitting the starlight using a dispersive element. In general, the incoming star light from the telescope is fed to a spectrograph that disperses the light into its constituent wavelengths by use of dispersive elements like a prism, a grating, or grism (combination of grating and prism). Finally, the dispersed light is recorded by an appropriate detector like charged-coupled devices (CCDs) or Infrared (IR) arrays. The resolving power of the system is given by,

$$R = \frac{\lambda}{\Delta\lambda} \tag{2.1}$$

where $\Delta\lambda$ is the smallest wavelength interval that can be resolved at the reference wavelength λ.

2.1.1 Spectrograph:

The basic components of a spectrograph consist of the following.

Slit: Slit is an aperture at the focal plane of the telescope, used to limit and identify the chosen field of observation in the sky. The slit width defines the spectral resolution and that approaches the limiting resolution for a narrow slit width.

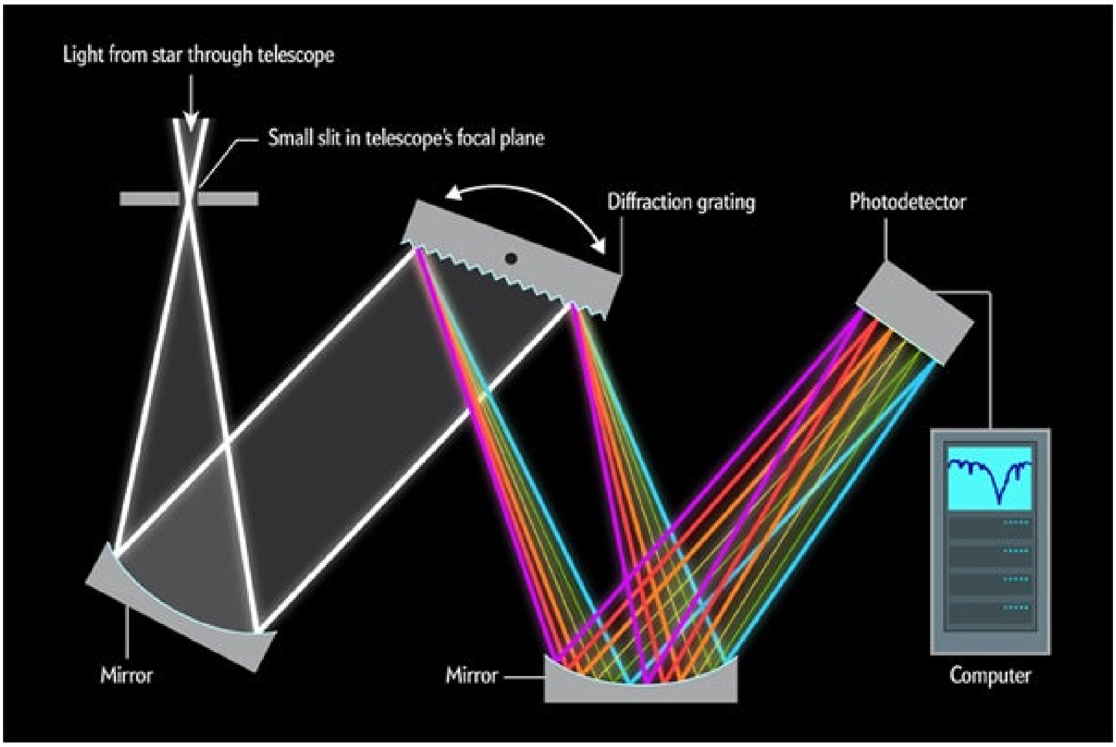

FIGURE 2.1: Schematic diagram of a spectrograph. Image courtesy: *Illustration by George Retseck in* `https://www.scientificamerican.com/`

Collimator: Collimeter is an optical element used to collimate the diverged beam of light coming from the slit into parallel rays and directing them to the dispersive element. Lenses, mirror or a combination of both can be used as a collimator.

Dispersive element: The parallel beam from the collimator is dispersed into its constituent wavelengths using a dispersive element, which can be a prism, a grating, or a combination of prism and grating called grism. While a prism which uses the refraction principle, disperses the light more in the blue, in a grating which uses diffraction, the dispersion is more in the redder side. A grism, which is a combination of grating and prism is designed in such a way that the diffraction angle of the grating is complemented by the refraction angle of the prism such that the dispersed beam, will be in-line with the incoming beam. In high-resolution spectroscopic studies, *é*chelle grating is used as a dispersion element, along with a cross disperser to separate the overlapping orders.

Camera: It is used to converge the parallel beam of light from the grism to

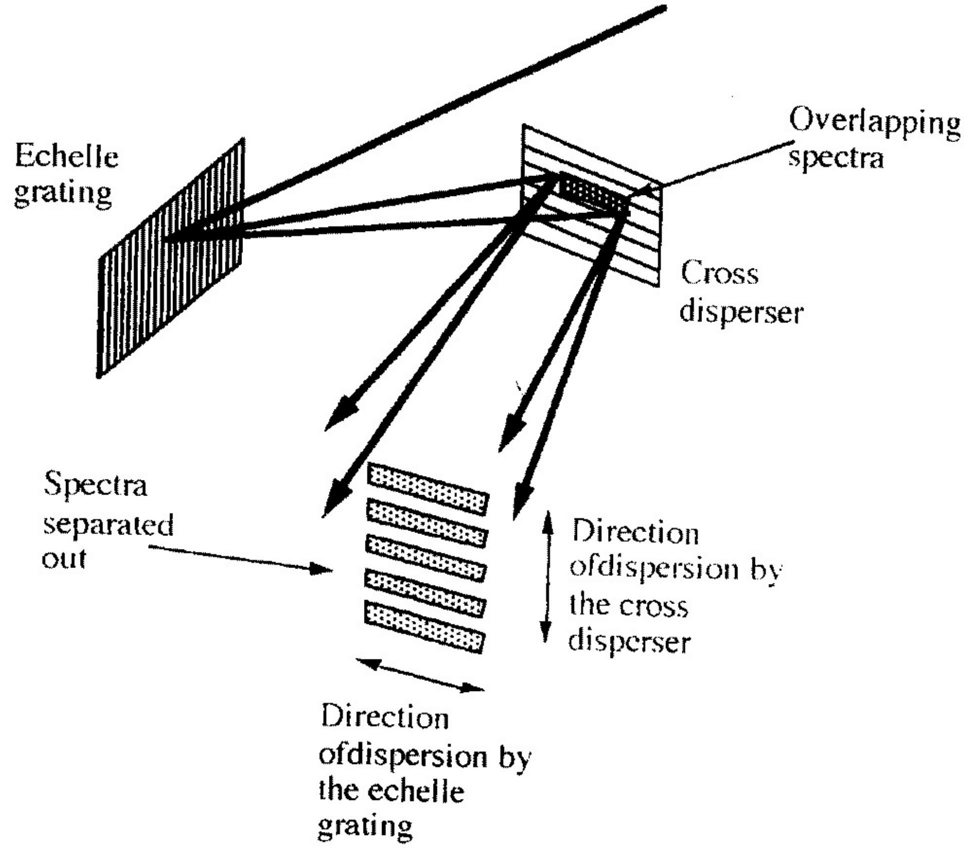

FIGURE 2.2: Schematic diagram of an échelle spectrograph. Image courtesy: *C.R. Kitchin in "Optical Astronomical Spectroscopy", CRC Press, 1995.*

the focal plane of the detector. Usually, a camera consists of a lens, mirror, or catadioptric systems (systems that combine both reflection and refraction).

Detectors: The detectors where the two-dimensional (2D) spectrum is recorded are mainly CCDs for optical spectroscopy, whereas infrared spectroscopy involves diode arrays.

2.1.2 *É*chelle spectrograph:

*É*chelle spectrograph is a type of spectrograph specifically designed to give simultaneous high-spectral resolution and broad spectral bandpass. It uses the principle of dispersion of the light into two orthogonal directions using two dispersive elements resulting in a 2D spectrum of the object. The incident beam will be first dispersed using a coarse-ruled (*é*chelle) grating, which again will be cross-dispersed using a prism or a grating in the orthogonal direction. Because of the high orders of the *é*chelle grating, the dispersed light from different orders of the *é*chelle grating overlap, hence to resolve this overlapping a cross disperser is used that disperses the light in the direction perpendicular to the dispersion direction of the *é*chelle grating. The main advantage of *é*chelle spectrograph is its wide wavelength coverage with high-spectral resolution. Using an *é*chelle spectrograph one can operate in orders ranging to 100.

2.2 Facilities used:

2.2.1 Himalayan Chandra Telescope (HCT):

The main astronomical observations used in this study are carried out using the 2-m class optical-infrared telescope, known as the Himalayan Chandra Telescope (HCT). This telescope is installed in the Indian Astronomical Observatory (IAO), on Mt. Saraswati, Hanle, Ladakh, India and operated by the Indian Institute of Astrophysics (IIA). The site having relatively high altitude of 4500m above sea level boasts of good seeing condition throughout the year due to lower levels of humidity, aerosols and light pollution. Due to the location of the observatory at a latitude and longitude of $32°46'46''$ N and $78°57'51''$ E respectively, it enables the astronomical observation in the entire northern hemisphere till the limit of the north of $-25°$ declination. Our sample selection is heavily influenced by this allowed limit of observation offered by the observatory. HCT is remotely operated by IIA using a dedicated satellite link, from the Centre for Research in Education, Science and Technology (CREST), Hoskote which is just 35 km away from Bengaluru.

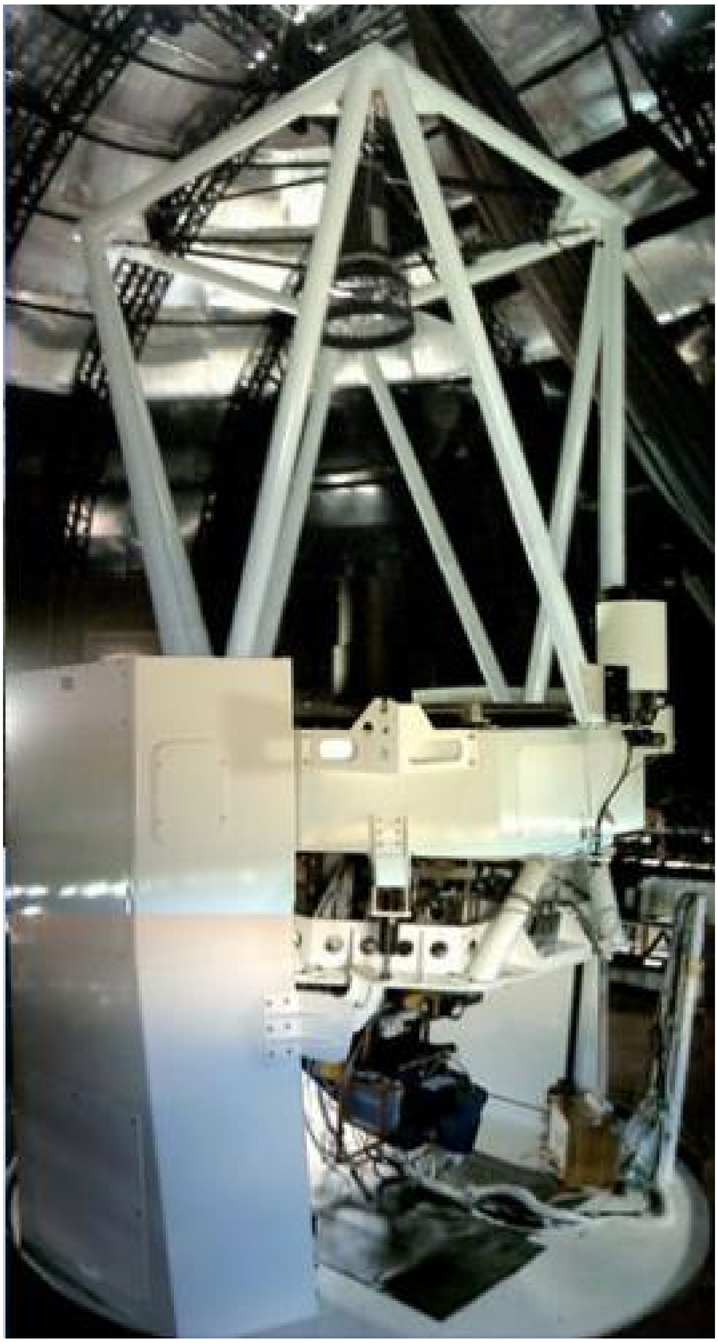

Figure 2.3: View of HCT. Image courtesy: `http://www.iiap.res.in/`

HCT has Ritchey-Chr$\acute{e}$tien configuration with Cassegrain focus set up in an alt-azimuth mount. It has 3 main science instruments

- **Hanle $\acute{E}$chelle Spectrograph (HESP)**
- **TIFR Near Infrared Spectrometer and Imager (TIRSPEC)**
- **Hanle Faint Object Spectrograph and Camera (HFOSC)**

All the instruments can be accessed in the same observing night which is made possible by mounting them on an instrument mount cube having four side ports and an on-axis port, at the Cassegrain focus of the telescope. For our project, we have extensively used HESP for optical high resolution studies and TIRSPEC for near-IR low resolution studies.

2.2.1.1 TIFR Near Infrared Spectrometer and Imager (TIRSPEC):

TIRSPEC is a near-infrared imager cum spectrograph developed in TIFR in collaboration with Mauna Kea Infrared (MKIR), Hawaii. Having a wavelength coverage of $1-2.5$ μm (Ninan et al. 2014), it is used for near-IR imaging as well as low resolution near-IR spectroscopy with maximum resolving power, R $\sim$ 1200. In imaging mode it provides a image scale of $0.3''$/pixel with a field of view of approximately $307'' \times 307''$. In spectroscopy it has single order modes covering $1.02-1.20$ μm (Y order), $1.21-1.48$ μm (J order), $1.49-1.78$ μm (H order) and $2.04-2.35$ μm (K order). It also provides cross disperse modes that provides simultaneous wavelength coverage of $1.02-1.49$ μm (YJ) and also $1.50-2.45$ μm (HK). The single order modes employ long slits, whereas for cross disperse mode short length slits are used. There are 5 slit settings each for both long slit ($300''$) and short slit ($10''$) configuration in the slit wheel, mounted at the telescope focal plane (TFP). Collimated image from telescope aperture is passed through two filter wheels (see Figure 2.4); The first one has broad band filters (J, H, K_s), order sorter filters (Y, J, H, K) and two cross dispersing grisms (HK and YJ). The second filter wheel

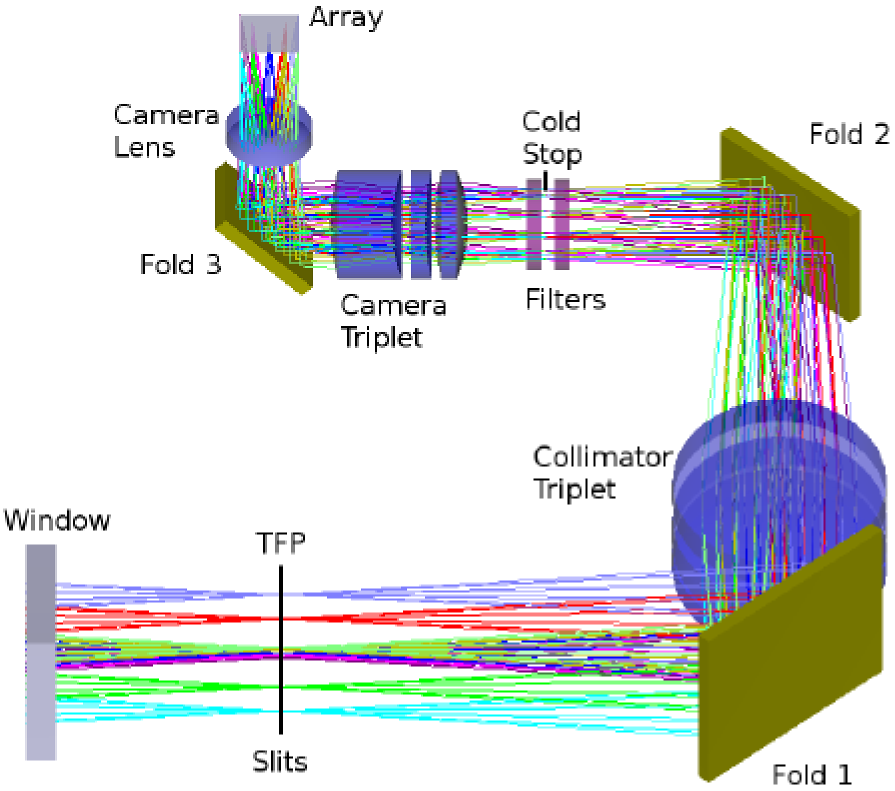

FIGURE 2.4: Design of TIRSPEC from Ninan et al. (2014)

consist of seven narrow band filters, one grism, block for taking dark frames and an open position. The final collimated beam is imaged onto the focal plane array detector with system of lenses. The focal plane array is a HgCdTe Astronomy Wide Area Infrared Imager (HAWAII-1) PACE Array manufactured by *Teledyne Scientific & Imaging, LLC, USA* having an array size of 1024×1024, with a pixel size of 18 μm square and cutoff wavelength of 2.5 μm. The array consists of HgCdTe detector layer on top with a silicon readout layer at the bottom. The detector is generally operated at a temperature of 76-77 K.

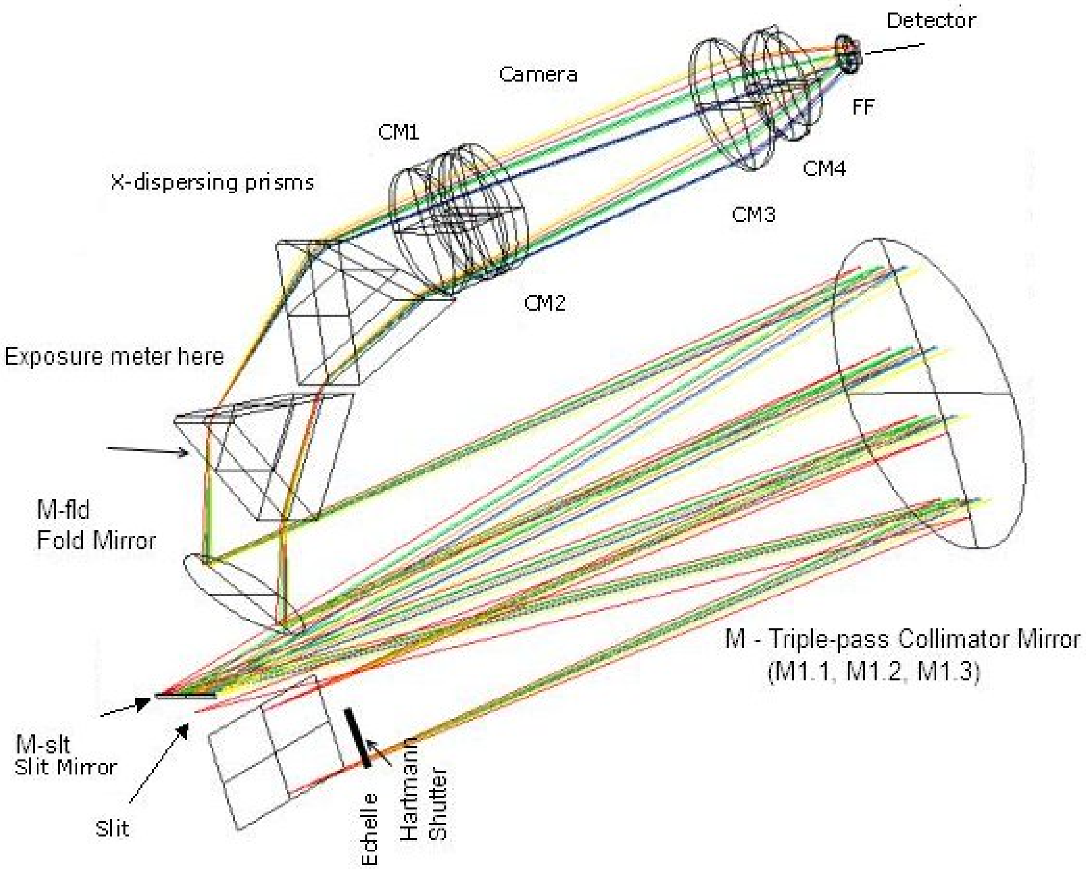

FIGURE 2.5: Schematic ray diagram of HESP with marked components. Image courtesy: `http://www.iiap.res.in`

2.2.1.2 Hanle *É*chelle Spectrograph (HESP):

HESP is a bench mounted, dual fibre-fed, high resolution, *é*chelle spectrograph designed on the concept of a white pupil (Sriram et al. 2018). It provides continuous spectral coverage from 3500 Å to 10000 Å and uses an R2 grating and 4K×4K CCD detector. It operates in two resolution modes; R = 30,000 and R = 60,000 using the image slicer. The spectrograph was built by Callaghan Innovation, New Zealand and the instrument control interface was developed by IIA. It provides both dual and single fibre modes. The availability of dual fibre mode enables to observe simultaneously the target star and a calibration source which assists in precise Radial Velocity (RV) measurements. The spectrograph layout of HESP is shown in Figure 2.5. It is thermally controlled to ΔT = ± 0.1 °C at a set point of 16 °C throughout the year providing long term stability of $\simeq 200$ ms^{-1}, which lowers the systematic errors, substantially.

2.2.2 Archival Data:

Apart from using the observational facilities of IIA, we have also used optical high resolution *é*chelle data from the European Southern Observatory (ESO) Data Archives[1]. These observations were made with ESO Telescopes at the La Silla and the Paranal Observatory under programme IDs 077.D−0458, 284.D−5048, and 074B−0455. The spectra were recorded using FEROS mounted on ESO 2.2m telescope in La Silla, Chile and UVES on ESO Very Large Telescope (VLT) at Paranal, Chile.

2.2.2.1 FEROS:

The Fibre-fed, Extended Range, *É*chelle Spectrograph (FEROS) instrument, is a high-resolution, environmentally controlled, *é*chelle spectrograph mounted on MPG/ESO 2.2m telescope located at the European Southern Observatory (ESO) in La Silla, Chile. Due to its high efficiency ($\sim$ 20%), broad continuous wavelength coverage of 3530 Å to 9200 Å and high spectral resolution, (R = 48000), it enables a large variety of stellar and extra-galactic spectroscopic observations requiring high spectral stability. FEROS has dual fibre mode providing simultaneous spectra of target star plus either sky background or one of the two calibration lamps. The fibres are illuminated via $2.0''$ apertures on the sky separated by $2.9''$. Spectrum of resolving power (R) of 48,000 is obtained, with a two-slice image slicer, spread over 39 *é*chelle orders.

---

[1] `http://archive.eso.org/wdb/wdb/adp/phase3_main/form`

2.2.2.2 UVES:

UVES (UV-Visual *é*chelle spectrograph) is a high resolution *é*chelle spectrograph mounted at 8.2m Kueyen (UT2) telescope of the ESO Very Large Telescope (VLT) at Paranal Observatory in Chile, which is designed to operate within the wavelength range 3000 Å − 11000 Å . The incoming light beam is separated into the two arms of the instrument, which are known as the Blue Arm with a wavelength coverage of 3000 Å − 5000 Å and a Red Arm ranging from 4200 Å − 11000 Å . These two arms can either operate separately or in parallel with the help of a dichroic beam splitter. For a $1''$ slit the typical resolving power is 40,000. Using narrower slits, higher resolving powers can be achieved (up to 110,000). The maximum (two-pixel) resolution is 80,000 in the Blue Arm and 110,000 in the Red Arm. Three additional image slicers also enable to obtain high resolving power without excessive light loss. The combination of the two arms with the image slicers provide observation in the wavelength windows of 3050 Å − 3870 Å, 3280 Å − 4560 Å and 5655 Å − 9460 Å, 6650 Å − 8540 Å and 8650 Å − 10240 Å . It is designed for obtaining maximum mechanical stability for obtaining accurate wavelength calibration.

2.2.2.3 Robert G. Tull Coud*é* Spectrograph:

Previously analysed *é*chelle spectrum of an EHe V1920 Cyg (Pandey et al. 2006) was available for analysis. The spectrum was observed from the Robert G. Tull Coud*é* Spectrograph (Tull et al. 1995) mounted on W.J. McDonald Observatory's Harlan J. Smith 2.7-m telescope. It also offers a wavelength coverage of 3400 Å − 10900 Å but the spectral coverage is incomplete having gaps in the echelle order longward of about 5500 Å.

2.3 Observing Strategies:

A well-planned observing strategy is very crucial in astronomical observation. It enables to obtain high quality scientific data in a time-sensitive observing run. Appropriate choice of science and calibration frames reduces the data processing time, providing the opportunity to devote substantial time into exploration of science cases. The observing strategies are mainly decided by keeping in mind the scientific objectives of the project and the degree of capability of the instrument to achieve it, and the required processing measures of raw data that will turn it into a useful scientific data. The plan required for optical and near infrared (NIR) spectroscopic observations are very similar except for few additional steps to be done in NIR. Below we discuss in detail the motivations we employed for perfect spectroscopic observations in this study.

2.3.1 Compatibility of scientific goal with instrument capability:

The main aim of a successful observation is to finally obtain scientific frames and calibration frames with high signal-to-noise ratio (SNR). To obtain frames having the best possible SNR, determination of the exposure time, and the number of exposures required becomes very important. It again depends on the apparent brightness of the star, the seeing conditions, duration of availability of the star in the field, etc. For e.g., while observing through HESP in good seeing conditions, a star having apparent magnitude, V-mag = 10, requires a combination of 3 frames of 40 minutes exposure each to obtain an SNR of $\sim$ 200 at $\lambda \sim 4500$ Å, whereas a star having V-mag = 2 requires single exposure of 1 minute to obtain similar SNR. Care should be taken not to overexpose the detector to avoid saturation. Even very faint sources do not necessitate very long exposure times (>1hr) at one go, as it invites a multitude of additional problems like more cosmic ray hits in the spectrum, possibility of change of sky condition and seeing, loss of track of the object, etc. So an optimum exposure time with multiple frames are generally obtained which can be combined later to improve the SNR. For NIR spectroscopic observation with TIRSPEC, the main difference lies in the NIR brightness and variation of the sky background, which greatly limits the exposure time. While the optical night sky brightness, V-mag, at IAO, Hanle $\sim$ 21.2 (Stalin et al. 2008) the average NIR brightness is, K-mag $\sim$ 13.3 (Ninan et al. 2014) almost 1500 times brighter than the optical. Hence, due to higher degree of saturation by the NIR sky background, the exposure time of a single frame is generally kept limited to maximum 100 secs even for an object having K-mag $\simeq$ 7. For improving SNR, multiple exposures of 100 secs are obtained.

2.3.2 Requirements for data processing:

To convert raw data into scientifically usable form, certain transformation or processing techniques are required also known as data reduction. This includes CCD processing to remove instrumental response, obtaining calibration frames, procedures to minimize the effect of sky background in the raw data. The contributions from the instrument response can be rectified using additional calibration frames which are observed along with the targets. Below we mention the corrections required and the steps followed by us in both optical and NIR spectroscopic observations to obtain the same.

2.3.2.1 Bias correction:

The bias level is an induced electronic offset to the CCD signal so that the Analog to Digital Converter ADC always receives a positive value. That background offset has to be corrected from all CCD data which can be done by subtracting the bias frames obtained by closed shutter zero second exposure. Due to the presence of the readout noise in the bias frames, several of them are taken in the course of an observing night that are then combined together (master bias) to minimise the noise.

2.3.2.2 Dark correction:

The noise resulting due to thermal excitation in CCD is also known as Dark current, which is a function of exposure time. Thus, dark frames are obtained having the same exposure time as object science frames with the shutter closed. Due to continuous cooling of optical CCDs by liquid nitrogen, the thermal noise is minimal hence, dark count can be ignored. In the case of NIR observations, the effect of dark current is more prominent, and hence, dark correction is applied.

2.3.2.3 Flat fielding:

The sensitivity of every CCD shows a pixel-to-pixel variation due to design and manufacturing limitations resulting in a noise. In order to make the CCD response uniform across all pixels, flat field correction is necessary. For this purpose, calibration frames known as flat frames have to be obtained. The main aim is to normalize the combined flat frame by dividing each pixel count by the average value in the array i.e., any sensitive pixel will be assigned a number slightly above 1, and any pixel that is less sensitive will be assigned a number slightly below 1. By dividing this normalized flat frame from an object science image, the sensitivity variations across the pixels get eliminated from the object's image. To obtain a flat frame, the CCD is uniformly illuminated by a featureless quartz halogen lamp for different spectrograph focus (in focus and out of focus) settings. Any variation in counts from pixel-to-pixel of the CCD for a uniform illumination gives an account of the sensitivity variation in each pixel including the wavelength. Multiple such flat field exposures are obtained, which has to be further combined to create a master flat. The normalized master flat containing the sensitivity response of the CCD has to be finally divided from the object frame. As the normalised master flat is divided from the object frame, a master flat frame having poor SNR, can introduce artefacts and hence result in degradation in the object frame. Hence the master flat with very high signal-to-noise ratio, substantially higher than the object frame is taken.

2.3.2.4 Wavelength Calibration:

Each extracted spectrum contains information in the form of counts vs pixels, i.e. a list of intensity corresponding to a series of positions along the central locus of the spectrum. To make the spectrum useful, the next step is to convert these positions into genuine wavelength units. This calibration is achieved using wavelength calibration frames. The principle is to obtain a set of spectra of arc lamps containing known emission features using the same instrumental setup as used for object frame. The emission features whose wavelength values are well-known are used to establish a relation between pixel and wavelength by fitting a low-order polynomial. This relation is applied to the spectra of the target objects to calibrate them into wavelength. We obtain wavelength calibration frames by illuminating the CCD with a Thorium-Argon lamp for HESP after each science frame without disturbing the instrumental setup for maximum accuracy. For TIRSPEC the same procedure is carried out with an Argon wavelength calibration lamp.

2.3.2.5 Sky substraction:

Astronomical spectra obtained from a ground based telescope will have the signatures of earth's atmosphere. The molecules in the terrestrial airmass, through which the starlight is travelling to the telescope, generate some absorption and emission features which are also known as telluric lines. Presence of these telluric lines hinders the accuracy with which the spectrum of the target star can be determined. Hence, even a bias and dark corrected, flat-fielded, and wavelength calibrated spectrum of the target has to be further corrected for the sky absorption and emission. In optical, the telluric absorption lines are present at all wavelengths but start becoming prominent beyond 6000 Å while in NIR the contribution is significant enough to affect the atmospheric transmission.

In order to tackle this problem, the spectrum of a rapidly rotating ($v \sin i$ $>$ 100 km/s) bright and hot subdwarf star of O- to B-type, observable in the same direction as the target star, is obtained. Such stars are also known as telluric standards and are chosen from Kitt Peak National Observatory (KPNO) Bright Star Catalogue[2]. These hot rapidly rotating bright stars will have very few stellar spectral features which again gets doppler broadened and smeared out into the continuum due to very high rotation. Thus, the only strong lines prominent in the observed spectrum of such hot star are atmospheric telluric lines. These identified telluric lines are then removed from the target star. For optical, the sky being not so significantly variable, observation of telluric standard is not always stringent. But in NIR, due to huge variability of NIR sky and the subsequent variability of the amount of water-vapour(H_2O) in the atmosphere, the strength of the telluric lines due to H_2O which dominates in NIR wavelengths varies rapidly. Hence, care should be taken to observe telluric standards immediately before and after each science observation to capture similar airmasses for telluric standards and science frames.

Atmospheric emission features are not so prominent in the stellar spectra in optical, but in NIR it gives a significant challenge due to strong and variable background emission. To remove the background emission in NIR, the spectrum of the sky background has to be subtracted from object spectra. Using cross-dispersal mode of TIRSPEC we employ this principle by adopting *classical ABBA dithering technique*. It involves observing the object at two slit positions on the sky (A and B) within the timescales small enough to neglect the variability of the sky emission lines. The two frames taken at the two different positions are then subtracted to form A-B, B-A etc resulting in an image with two spectra, one

---

[2] `http://www-kpno.kpno.noao.edu/Info/Caches/Catalogs/BSC5/catalog5.html`

positive and one negative removing the background emission lines. The positive images are extracted from both of the A-B and B-A frames and then combined to improve the signal-to-noise ratio.

2.3.3 Data processing:

The data were processed using standard software packages of IRAF (Image Reduction and Analysis Facility). IRAF is distributed by the National Optical Astronomy Observatory, which is operated by the Association of Universities for Research in Astronomy (AURA) under a cooperative agreement with the National Science Foundation. The data processing consists pre-processing of the CCD images, extraction of one dimensional spectrum from the images, and the subsequent wavelength calibration.

2.3.3.1 Data pre-processing:

Data pre-processing involves bad-pixel correction, trimming, bias subtraction, dark subtraction, and flat-fielding. The data pre-processing tasks heavily involve usage of the package *ccdproc* of IRAF. For every CCD there are certain pixels, known as bad pixels which will be insensitive to light. The identified bad pixels are replaced by the average count of neighbouring pixels. The bad-pixel corrected images are trimmed using *ccdproc* to ensure only the exposed part of CCD image remains. The combined master bias frame and dark current are subtracted from all object and calibration frames using *ccdproc.* The bias/dark corrected master flat frame is normalised using the task *apnormalize.* All the bias/dark corrected object frames are then divided by this normalised flat frame using *ccdproc.*

2.3.3.2 Spectrum extraction and wavelength calibration:

The spectrum extraction is an interactive process that is used to convert a 2D image into 1D spectrum. It involves locating and fixing the aperture of the object, identifying the background region to eliminate scattered light, tracing the aperture along the dispersion axis using a cubic spline function, and finally extraction of the 1D spectrum by summing up the counts within the defined apertures. This entire process is carried out using the task *apall* in IRAF. Now due to the presence of many orders in an *é*chelle spectrum it is difficult to identify positions of faint orders in the object spectra. For this purpose, a very well exposed frame of any bright object is used to locate all the orders. This is used as a reference to define the aperture or the extraction window of different orders of object frames as well as calibration frames. Flats or a bright star spectrum can be used for order tracing. As in our case, the flats in HESP have lower counts in the blue, we use the spectrum of a bright hot star, which provides sufficient counts in blue as well as red, as a reference for the order extraction.

Like the object frame, the spectrum of the wavelength calibration lamp, Thorium-Argon, is extracted in a similar way. Emission lines of the extracted lamp spectrum is identified using a Th-Ar spectrum atlas and wavelengths are assigned using the task identify. A polynomial relation is identified between the known wavelength and corresponding pixel positions which is also known as dispersion solution. This dispersion solution is finally applied to the extracted object and standard star spectrum using the task *refspec* and *dispor* to get a wavelength calibrated spectrum. The accuracy of the dispersion solution is verified by cross-checking with wavelengths of known atmospheric emission or absorption lines across the spectrum.

2.3.3.3 Continuum normalization:

The continuum level of the wavelength calibrated spectrum of the target and the standard star is determined by choosing the points devoid of any absorption or emission features, which is then further then normalised to unity using the IRAF task *continuum.* In the above-mentioned task the continuum points in the wavelength calibrated spectrum are chosen interactively and then a smooth spline function is fit through this points defining the continuum which is further used for normalising the spectra.

2.3.3.4 Telluric correction:

The continuum normalised spectrum of the target star is then cross-correlated with the spectrum of the telluric standard stars to identify telluric lines. These telluric lines are then removed by division of the target star spectrum by the telluric standard star spectrum using the task *telluric.*

2.4 Final Reduced science spectrum:

The continnum normalised, telluric corrected spectrum of the target star is ready for further analyses involving equivalent width measurement of absorption lines, radial velocity determination and correction. Multiple such extracted spectra of the same object are combined to improve the SNR ratio, and identify and remove stray cosmic ray hits. Note, before combining the spectra obtained through different instrumental set-ups or different telescopes, the spectral resolution of each spectrum is determined from the FWHM of weak telluric lines. Finally they are rebinned to a common wavelength resolution before combining. Spectra were also smoothened further to increase SNR, keeping in mind that the limit of smoothing is up to the level such that no stellar profiles should be altered.

The final science spectrum is reduced and ready to be used for a plethora of scientific studies like abundance analysis, radial velocity measurements, pulsation and variability studies, etc. The strength of a spectral line of a particular ionic state of a species can be used to determine the atmospheric parameters of the star as well as the chemical composition. Binarity of a stellar system can be identified by observing periodic wavelength shifts in the stellar spectrum observed at different times. Asymmetric absorption line profiles as well as variability of a known spectral feature with multiple exposures, can tell us about the pulsating nature of the star. Thus the spectrum of a star gives a comprehensive idea about the nature of the star, its age, chemical properties etc, helping us to explore their evolutionary history. In broader terms the stellar spectrum gives a glimpse to the evolution of the universe through ages, whose signatures are imprinted on the stellar atmosphere in form of the unique spectral features.

Chapter 3

Are DY Persei stars cooler cousins of R Coronae Borealis stars?[1]

An overview

In this work we present for the first time, the study of low resolution *H*- and *K*- band spectra of 7 DY Per type and suspects stars as well as DY Persei itself. We also observed *H*- and *K*- band spectra of 3 R Coronae Borealis (RCB) stars, 1 hydrogen-deficient carbon (HdC) star and 14 cool carbon stars including normal giants as comparisons. High ^{12}C/^{13}C and low ^{16}O/^{18}O ratios are characteristic features of majority RCBs and HdCs. We have estimated ^{16}O/^{18}O ratios of the programme stars from the relative strengths of the ^{12}C^{16}O and ^{12}C^{18}O molecular bands observed in *K*- band. Our preliminary analysis suggest that a quartet of the DY Per suspects along with DY Persei itself seems to show isotopic ratio strength consistent with the ones of RCB/HdC stars whereas two of them do not show significant ^{13}C and ^{18}O in their atmospheres. Our analysis provides further indications that DY Per type stars could be related to RCB/HdC class of stars.

---

[1] The contents of this chapter is based on the publication (Bhowmick et al. 2018)

3.1 Introduction

R Coronae Borealis (RCB) stars are low mass, hydrogen deficient carbon rich yellow supergiants characterised by their unusual light variability showing a rapid aperiodic light dimming of several magnitudes in the optical with a slow return to their maximum light, and exhibit IR excess (Payne-Gaposchkin & Gaposchkin 1938; Clayton 1996). Six hydrogen deficient carbon stars (HdCs) are known which are spectroscopically similar to RCBs but most of them do not exhibit light declines or show IR excess (Warner 1967; Clayton 2012), the exception being HD 175893 that shows IR excess (Tisserand 2012).

DY Persei and DY Persei type (DY Per type) stars are a peculiar class of cooler carbon stars showing also dramatic light declines but the light decline rate is slower than RCBs with a symmetry in the rate of light decline and the light growth. DY Per type star candidates are the stars having similar light curve and position in $J - H$ and $H - K$ diagram like DY Per type stars found so far, but without any spectroscopic observations or confirmations. In this work we introduce the term DY Per suspect, i.e. cool carbon stars showing spectroscopic features similar to DY Per type stars but whose light curve has not shown characteristic symmetrical decline events but rather large photometric variations that can also be due to dust obscuration.

Though DY Per type stars, as mentioned in the Chapter-1, Section-1.2.3, appear to be hydrogen-deficient similar to RCBs due to absence of hydrogen Balmer lines in their spectra, nevertheless, the status of hydrogen deficiency is not properly explored due to their cooler effective temperatures and absence of flux in the G band of CH at 4300Å region (Keenan & Barnbaum 1997; Začs et al. 2007; Yakovina et al. 2009). Due to the small number of known DY Per type stars,(seven Galactic DY Per type stars (Tisserand et al. 2008, 2013; Miller et al. 2012) and 27 Magellanic (Alcock et al. 2001; Tisserand et al. 2004, 2009)), it is a challenge to characterise these stars and investigate any possible connection with the RCBs. We therefore also introduced DY Per suspect stars in our study.

Table 3.1: Log of observations of RCB and HdC stars as well as DY Persei and the DY Per affiliated stars.

Star name (SIMBAD)	Date of observation	K- mag.[*] (SIMBAD)	S/N (2.29 μ)	Star type
HD 137613	16 April 2016	5.25	70	HdC
Z UMi	01 May 2016	7.3	55	RCrB
SV Sge	18 November 2016	5.9	110	RCrB
ES Aql	18 November 2016	7.9	105	RCrB
DY Persei	04 October 2014, 16 January 2016, 17 Jan 2016 , 06 November 2016	4.4	105	DY Per prototype
ASAS J065113+0222.1	16 January 2016, 17 Jan 2016 , 23 February 2017	4.9	80	DY Per type star[a]
ASAS J040907-0914.2 (EV Eri)	16 January 2016, 17 Jan 2016 , 06 November 2016, 23 February 2017	3.6	95	DY Per suspect[b]
ASAS J052114+0721.3 (V1368 Ori)	16 January 2016, 06 November 2016, 23 February 2017	2.19	110	DY Per suspect[b]
ASAS J045331+2246.5	04 October 2014, 16 January 2016, 17 Jan 2016	2.84	80	DY Per suspect[b]
ASAS J054635+2538.1 (CGCS 1049)	16 January 2016, 17 Jan 2016 , 18 March 2016	4.3	90	DY Per suspect[b]
ASAS J053302+1808.0 (IRAS 05301+1805)	16 January 2016, 17 Jan 2016	5.6	90	DY Per suspect[b]
ASAS J191909-1554.4 (V1942 Sgr)	01 July 2016	1.06	105	DY Per type star[a]

[a] Miller et al. (2012)

[b] Tisserand et al. (2013)

[*] *Reported from the Two Micron All Sky Survey Point Source Catalogue (Cutri et al. 2003)*

Apart from hydrogen-deficiency, one of the principal characteristics of RCBs and HdCs that distinguishes them from normal AGB and post-AGB stars are the presence of very high amounts of ^{18}O and weak or no presence of ^{13}C in their atmospheres. Using the NIR, K-band spectra of these stars, Clayton et al. (2005, 2007); García-Hernández et al. (2009, 2010) found that the isotopic ratios of ^{16}O/^{18}O, derived from the relative strengths of the observed ^{12}C^{16}O and ^{12}C^{18}O molecular bands, range from 0.3 to 20. Note that the typical value of $^{16}O/^{18}O \sim 500$ in solar neighbourhood and 200 to 600 in Galactic interstellar medium (Geiss et al. 2002). Also, the $^{12}C/^{13}C$ ratio for several RCBs and all HdCs are significantly higher than the CN-equilibrium value of 3.4 (Alcock et al. 2001; Hema et al. 2012). Thus, the low values of $^{16}O/^{18}O$ and high values of $^{12}C/^{13}C$ in both HdCs and RCBs make it obvious that these two classes of carbon-rich and hydrogen poor stars are indeed closely related.

On the contrary, the possible evolutionary connection of DY Per type stars with RCBs/HdCs or with normal carbon rich AGBs needs to be explored. Začs et al. (2007) reported the high resolution spectrum of the DY Persei showing significant hydrogen deficiency with high $^{12}C/^{13}C$ ratio like most RCBs. It is to be noted that the low resolution spectra of DY Per type variables in the Magellanic clouds show significant enhancement of ^{13}C from the isotopic Swan bands at about 4700Å, but the ^{13}CN band at 6250Å is not seen (Alcock et al. 2001; Tisserand et al. 2009). Also, the enhancement of ^{13}C in the atmospheres of Magellanic DY Per type stars is reported for only 9 cases out of 27 (Alcock et al. 2001; Tisserand et al. 2004, 2009). Hence, there seems to exist a mixed $^{12}C/^{13}C$ isotopic ratio in Magellanic DY Per type stars.

In this work we search for the contributing spectral features involving ^{18}O and ^{13}C in the low resolution H- and K-band NIR spectra of the observed DY Per type stars and DY Per suspects. Note that our DY Per suspects are the cool carbon stars taken from Table-5 of Tisserand et al. (2013) which they rejected as RCB candidates due to enhanced ^{13}C in their spectra and no clear rapid decline events in their light curves. However, we selected these stars based on their similarity with DY Per type stars as given in the description by Tisserand et al. (2013) in their text, verbatim, “Their light curves show variations up to 2 mag, but with no clear signs of a fast decline. Because they all present large photometric oscillations of $\sim$ 0.8 mag amplitude and their spectra do not show clear signs of presence of hydrogen, they should be considered as DY Per star candidates.”

The objective is to explore possible connections between DY Per type stars and DY Per suspects with classical carbon stars or with RCBs/HdCs. Our observations, analysis, and results are discussed in the following Sections.

3.2 Observations and Reductions

H- and *K*-band spectra of our target stars were obtained from TIFR Near Infrared Spectrometer and Imager (TIRSPEC) (see Chapter-2, Section-2.2.1.1) mounted on Himalayan Chandra Telescope (HCT) at Hanle, Ladakh, India. The log of observations is given in Table 3.1 for the RCB and HdC stars as well as all the DY Per affiliated stars, and in Table 3.2 for the normal and cool carbon stars.

Table 3.2: Log of observations of normal cool giants selected from Jorissen et al. (1992); Tanaka et al. (2007)

Star name (SIMBAD)	Date of observation	*K*- mag. (SIMBAD)	S/N (2.29 μ)	Star type
Arcturus	01 May 2016	-2.9	85	K
HD 156074	14 October 2014	5.28	125	R
HD 112127	17 Jan 2016 , 18 March 2016	4.17	170	R
BD+06 2063	16 April 2016	4.1	205	S
HR 337	17 Jan 2016	-1.85	120	M
HD 64332	16 April 2016	2.3	185	S
HD 123821	18 March 2016	6.3	110	R
HR 3639	16 April 2016	-1.7	130	S
HD 58521	18 March 2016	-0.44	140	S
HD 76846	17 Jan 2016 , 18 March 2016	6.6	130	R
V455 Pup	17 Jan 2016 , 16 April 2016, 23 February 2017	5.27	80	C
TU Gem	18 March 2016	0.78	85	N
Y CVn	16 April 2016	-0.81	80	J
RY Dra	16 April 2016	0.19	75	J

Spectra were recorded in *HK* cross-dispersal mode in two dithered positions with multiple exposures in each position having average exposure time of 100s for each frames. The frames were combined to improve the signal-to-noise ratio (SNR) (see Tables 3.1 and 3.2). The recorded spectra in the *H*- band appear noisier than the *K*- band due to lower photon counts. For stars fainter than *K*-magnitude 6, frames of 500s exposure were taken and combined to improve the SNR. After each set of star exposures, three continuum lamp spectra and an argon lamp spectrum were obtained. For removing the telluric lines from the star's spectrum, rapidly rotating O/B type dwarfs (telluric standards) were observed during each observing run in the direction of the programme stars.

The slit setting mode S3 with a slit width of 1.97" was available. For this slit setting the average resolving power at the *H*- and *K*- central wavelength is about ∼900 as measured from the FWHM of the clean emission lines of the comparison lamp spectrum. The data obtained is made available after dark and cosmic ray corrections. Standard procedures for observing and reducing the data as mentioned in Chapter-2, Section-2.3 were followed.

All the 7 DY Per affiliated stars (2 DY Per type stars and 5 DY Per suspects), we observed, were taken from the catalogue of stars presented by Tisserand et al. (2013) and Miller et al. (2012). Our selection was limited by the location of the Observatory (see Chapter-2, Section-2.3). Three cool RCBs: Z UMi, SV Sge and ES Aql and one HdC star HD 137613 were also observed. Except for Z UMi, the other two RCBs were observed at about their maximum light as verified from the AAVSO database(www.aavso.org); Z UMi was in recovery phase (ΔV$\sim$3) and so the observed spectrum is particularly noisy. We have also observed a variety of normal giants/supergiants covering the effective temperature range of the programme stars. The normal giants/supergiants were taken from Jorissen et al. (1992); Tanaka et al. (2007) spanning K giants through N- and J-type cool carbon stars. These stars along with the HdC/RCBs were observed to compare and confirm the presence/absence of ^{13}C^{16}O and ^{12}C^{18}O features in DY Per type stars, and DY Per suspects.

3.3 CO bands and overview of the spectra

The band head wavelengths of $^{12}C^{16}O$ are available in literature for both *H*- and *K*-band region. We have calculated the wavelengths of $^{13}C^{16}O$ and $^{12}C^{18}O$ by using the standard formula for isotopic shift from Herzberg (1950) and the ground state constants of $^{12}C^{16}O$ are taken from Mantz et al. (1975). We have verified our calculated band head wavelengths of $^{13}C^{16}O$ and $^{12}C^{18}O$ for the first overtone transition, with those given by Clayton et al. (2005) and hence, applied the same procedure to calculate the second overtone band head wavelengths of $^{13}C^{16}O$ and $^{12}C^{18}O$.

Figures 3.1 and 3.2 show the *H*-band (1.52−1.78 μm region) spectra of our programme stars and the comparison stars (normal giants/supergiants), respectively; the 2nd overtone features of $^{12}C^{16}O$, $^{12}C^{18}O$ and $^{13}C^{16}O$ including C_2 Balik-Ramsay system (0-0) are marked with other key features. *H*-band spectra of HD 156704 (normal K giant) and Z UMi (RCB) were very noisy, hence, not shown. The *K*-band (2.25−2.42 μm region) spectra of the programme stars and the comparison stars are shown in Figures 3.3 and 3.4, respectively; the first overtone band heads of $^{12}C^{16}O$, $^{12}C^{18}O$ and $^{13}C^{16}O$ are indicated. The spectra shown in Figures 3.1,3.2,3.3,3.4 are normalised to the continuum and are aligned to lab wavelengths of $^{12}C^{16}O$ band heads.

3.4 Preliminary results and discussion

The observed stars show strong 1st overtone bands of $^{12}C^{16}O$ in the *K*-band region (see Figures 3.3 and 3.4). As reported by Clayton et al. (2007), prominent 1st overtone bands of $^{12}C^{18}O$ are seen with no detection of $^{13}C^{16}O$ in the two cool RCBs, SV Sge and ES Aql, and in the HdC star HD 137613 (see Figure 3.3); Z UMi spectrum is particularly noisy but suggests the presence of $^{12}C^{18}O$ bands. As

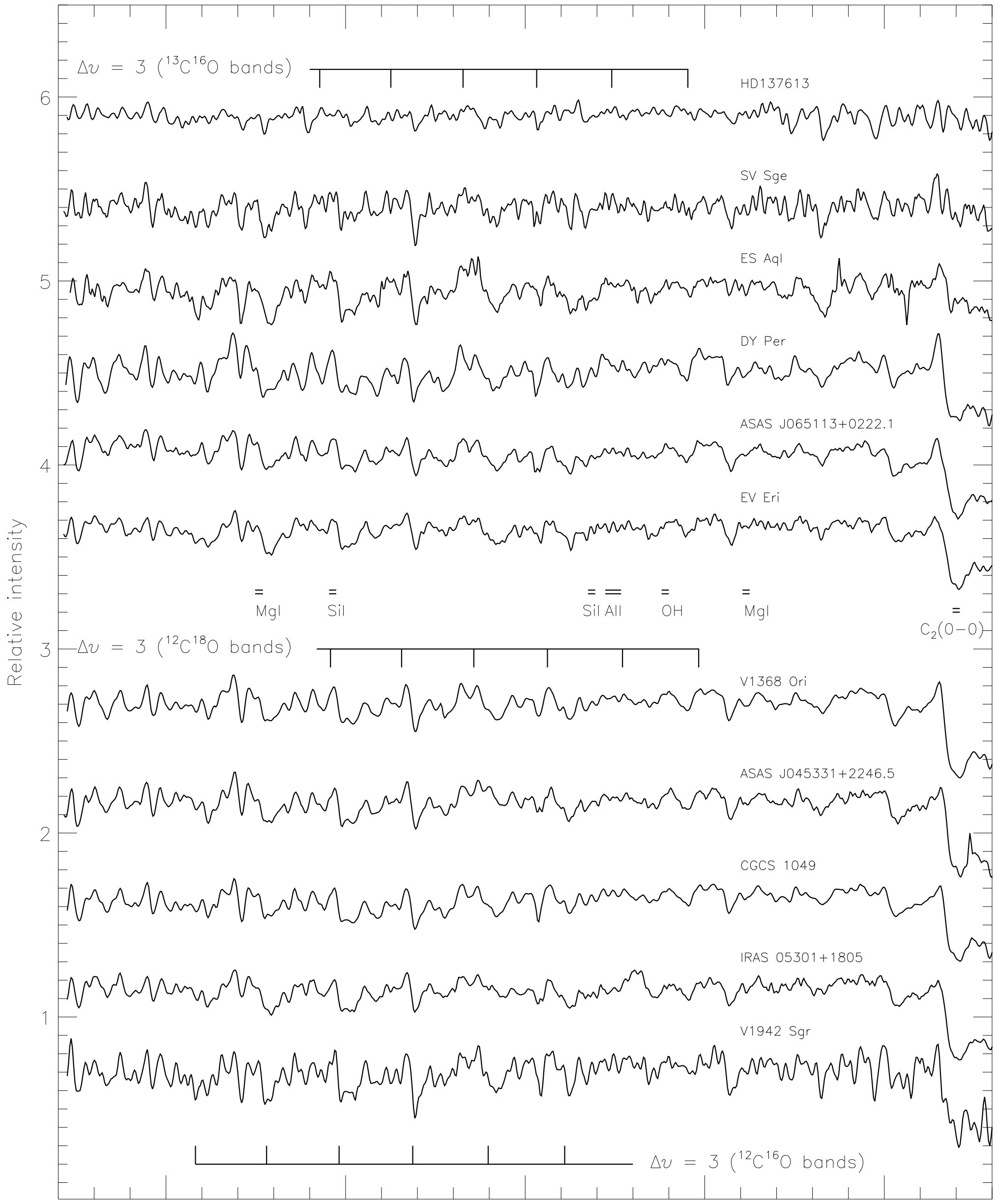

FIGURE 3.1: 1.52−1.78 μm spectra of RCBs, HdCs, DY Persei, and DY Per affiliated stars. The band head positions of $^{12}C^{16}O$,$^{12}C^{18}O$ and $^{13}C^{16}O$ and other key features are marked. The stars are ordered according to their increasing effective temperature (approximate) from bottom to top.

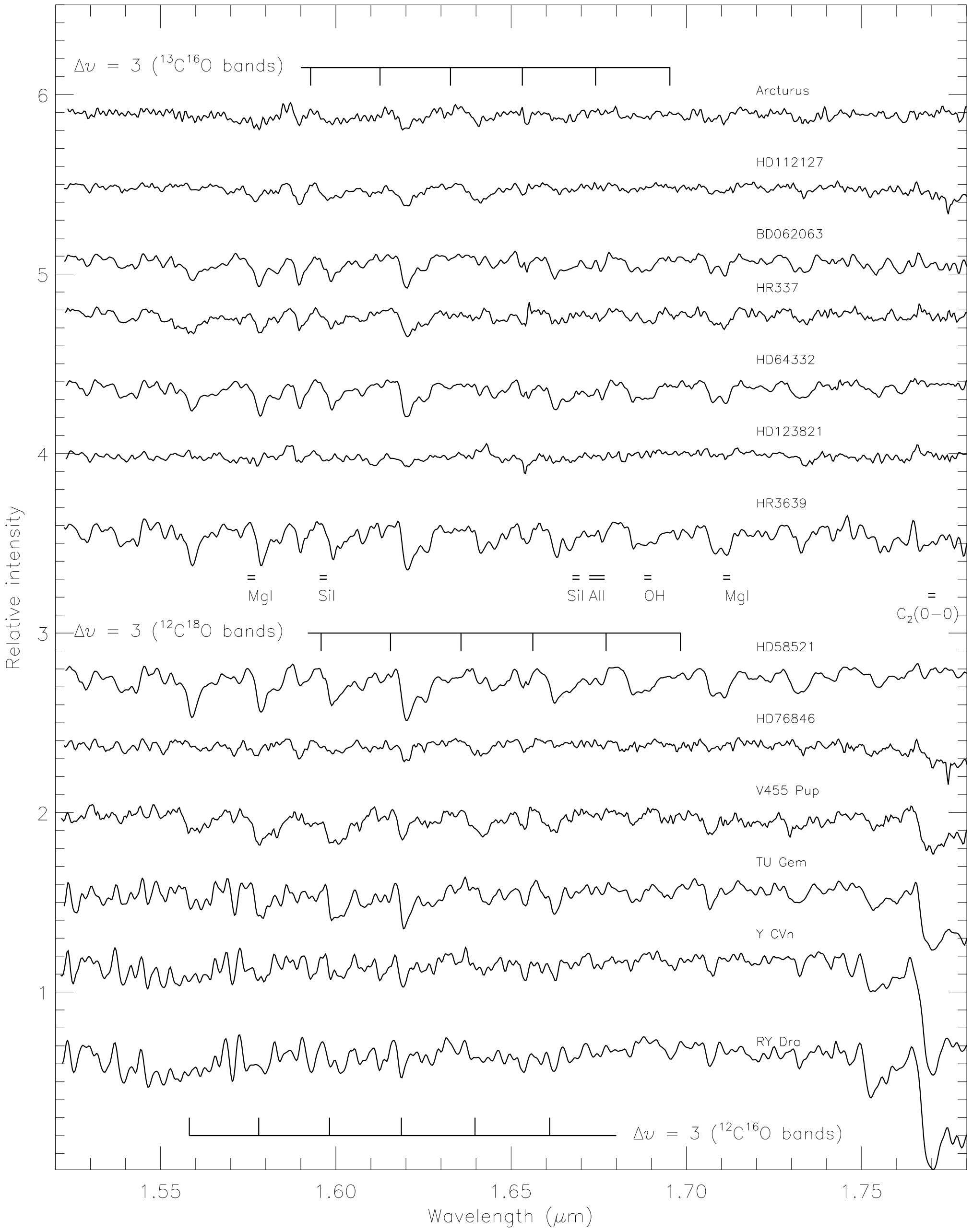

FIGURE 3.2: 1.52−1.78 μm spectra of normal giants/supergiants of different spectral type ranging from K giants on the top to cool N type carbon stars at the bottom. The band head positions of $^{12}C^{16}O$, $^{12}C^{18}O$ and $^{13}C^{16}O$ and other key features are marked.

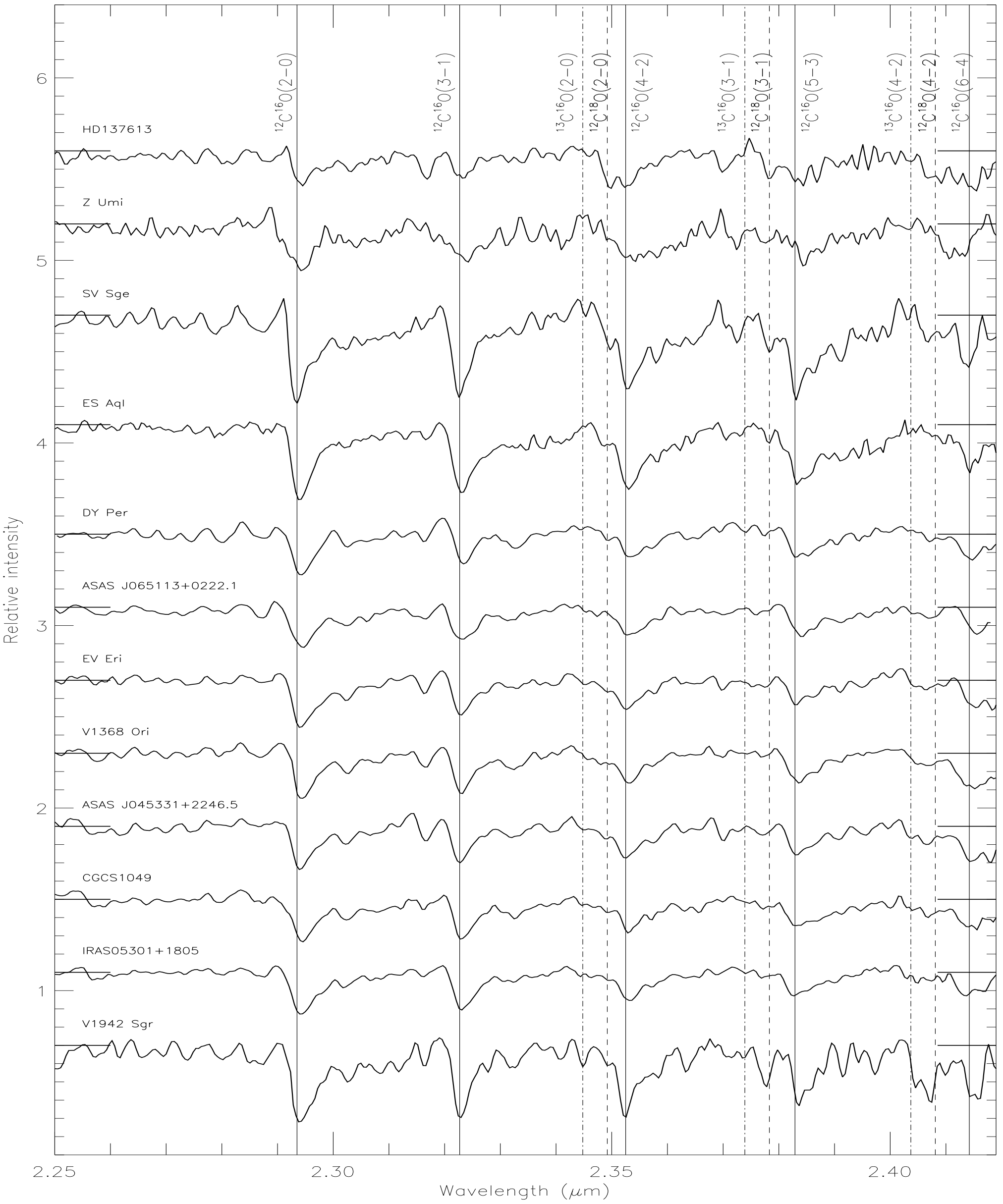

FIGURE 3.3: 2.25−2.42 μm spectra of RCBs, HdC, DY Persei, and DY Per affiliated stars , with wavelengths of $^{12}C^{16}O$, $^{12}C^{18}O$ and $^{13}C^{16}O$ indicated by vertical lines. The stars are ordered according to their increasing effective temperatures (approximate) from bottom to top. The position of the mean continuum for each spectrum is indicated by the line marked.

FIGURE 3.4: 2.25−2.42 μm spectra of normal giants of different spectral type ranging from K giants in the top to cool N type carbon stars in the bottom. As in Figure 3 ,wavelengths of $^{12}C^{16}O$, $^{12}C^{18}O$ and $^{13}C^{16}O$ indicated by vertical lines. The position of the mean continuum for each spectrum is indicated by the line marked.

TABLE 3.3: Absorption depths of first overtone CO band heads and the estimated $^{16}O/^{18}O$ and $^{12}C/^{13}C$ ratios of RCBs, HdC and DY Per affiliate stars.

Star name	Star type	$^{12}C^{16}O$		$^{12}C^{18}O$		$^{16}O/^{18}O$	$^{12}C/^{13}C$
		2-0	3-1	2-0	3-1		
HD 137613	HdC	0.174	0.127	0.2	0.148	$\sim 0.86 \pm 0.02$	> 15
SV Sge	RCB	0.46	0.45	0.225	0.22	$\geq 2.05 \pm 0.01$	> 45
ES Aql	RCB	0.373	0.362	0.093	0.088	$\geq 4 \pm 0.1$	> 37
DY Persei	DY Persei	0.24	0.19	0.06	0.045	$\geq 4 \pm 0.2$	> 24
ASAS J045331+2246.5	DY Per suspect	0.25	0.22	0.052	0.045	$\geq 5 \pm 0.2$	> 19
V1368 Ori	DY Per suspect	0.275	0.25	0.05	0.045	$\geq 5.5 \pm 0.1$	> 25
EV Eri	DY Per suspect	0.29	0.22	0.04	0.03	$\geq 7.5 \pm 0.2$	> 20
CGCS 1049	DY Per suspect	0.25	0.23	0.025	0.024	$\geq 10 \pm 0.5$	> 19
IRAS 05301+1805	DY Per suspect	0.24	0.23	···	···	···	> 19
ASAS J065113+0222.1	DY Per type star	0.22	0.20	···	···	···	> 15

expected, a close inspection of the *K*-band spectra of the observed normal cool giants clearly show the presence of $^{13}C^{16}O$ bands including the prominent $^{12}C^{16}O$ bands with no detection of $^{12}C^{18}O$ bands (see Figure 3.4). We have used these HdC/RCBs and cool giants spectra as comparisons to look for the detection of $^{12}C^{18}O$ and $^{13}C^{16}O$ bands in the observed spectra of DY Persei, DY Per type stars and DY Per suspects.

Among the DY Persei and seven DY Per affiliated stars we find suggestion of $^{12}C^{18}O$ bands with no clear detection of $^{13}C^{16}O$ bands in five of these stars : DY Persei, EV Eri, V1368 Ori, ASAS J045331+2246.5, and CGCS 1049 (see Figure 3.3). In Figure 3.3 spectra of two stars, ASAS J065113+0222.1 and IRAS 05301+1805, do not show any suggestion of $^{12}C^{18}O$ and $^{13}C^{16}O$ bands within the detection limit. In the case of V1942 Sgr's spectrum (see Figure 3.3), numerous features are observed and we could not confirm the presence or absence of both $^{12}C^{18}O$ and $^{13}C^{16}O$ bands.

Based on the observed *K*-band spectra of HdC/RCBs, DY Persei, and DY Per affiliated stars, an attempt is made to estimate $^{16}O/^{18}O$ values by measuring the

Table 3.4: Absorption depths of first overtone CO band heads and the estimated $^{12}C/^{13}C$ ratios of normal and cool carbon giants.

Star name	$^{12}C^{16}O$		$^{13}C^{16}O$		$^{12}C/^{13}C$
	2-0	3-1	2-0	3-1	
Arcturus	0.228	0.205	0.098	0.095	$> 2.25 \pm 0.2$
HD 156704	0.125	0.11	0.04	0.032	$> 3.25 \pm 0.2$
HD 112127	0.215	0.225	0.060	0.08	$> 3.2 \pm 0.4$
BD+062063	0.255	0.268	0.126	0.125	$> 2.05 \pm 0.1$
HR 337	0.24	0.21	0.089	0.087	$> 2.55 \pm 0.2$
HD 64332	0.33	0.332	0.158	0.165	$> 2.05 \pm 0.1$
HD 123821	0.167	0.186	0.052	0.083	$> 2.75 \pm 0.5$
HR 3639	0.33	0.331	0.16	0.145	$> 2.15 \pm 0.2$
HD 58521	0.365	0.322	0.13	0.102	$> 3 \pm 0.2$
HD 76846	0.184	0.186	0.088	0.101	$> 1.9 \pm 0.2$
V455 Pup	0.266	0.243	0.066	0.07	$> 3.75 \pm 0.3$
TU Gem	0.312	0.293	0.068	0.075	$> 4.2 \pm 0.3$
Y CVn	0.262	0.2512	0.1632	0.16	$> 1.6 \pm 0.2$
RY Dra	0.215	0.213	0.123	0.118	$> 1.75 \pm 0.1$

absorption depths of $^{12}C^{16}O$ and $^{12}C^{18}O$ band heads using 2-0 as well as 3-1 bands. This exercise is more difficult for the DY Per type stars since spectra of cool stars are full of absorption features and the blending of these features with the identified $^{12}C^{18}O$ band heads (in such low resolution spectra) is surely a possibility. Yet with the exact wavelength matches we could confirm the presence of $^{12}C^{18}O$ bands. As these bands are not completely resolved and the bands from the more abundant isotopic species are possibly saturated, the estimated $^{16}O/^{18}O$ values are the lower limits in most cases (see Table 3.3). Using synthetic spectra for the analysis is avoided as it is extremely difficult to identify all the contributing features from the observed low resolution spectra.

As all the DY Per affiliate stars observed here were reported to show strong presence of ^{13}C in their respective discovery papers (Miller et al. 2012; Tisserand et al. 2013), we expected enhanced ^{13}C^{16}O depths in the K-band spectra. We have estimated ^{12}C/^{13}C ratios from the K-band absorption depths of ^{12}C^{16}O and ^{13}C^{16}O band heads. Since the observed depth at ^{13}C^{16}O band heads is more or less comparable with the noise levels of the observed spectra, we conclude that there is no clear suggestion of ^{13}C^{16}O in their spectra within the detection limit. However, we have estimated the lower limits of the ^{12}C/^{13}C ratios measured from the K-band spectra of these stars as given in Table 3.3. The depth at ^{13}C^{16}O 2-0 band head region is used due to the better signal than other regions. We find that our estimated lower limit on ^{12}C/^{13}C for DY Persei is in line with the range of values, 20-50, obtained by Keenan & Barnbaum (1997).

We have also estimated the ^{12}C/^{13}C ratios for the observed normal and the cool carbon giants (see Table 3.4) for comparison. These very low lower limits on ^{12}C/^{13}C ratios measured for these carbon giants clearly show enhanced ^{13}C in contrast to the DY Per affiliates. The ^{12}C/^{13}C ratios are expected to be more than the estimated lower limits for the normal and cool carbon giants.

In the H-band region, the observed spectra do show the second overtone bands of ^{12}C^{16}O but most of these are affected by noise. The strength of ^{12}C^{16}O features in H-band is much weaker compared to those in K-band. Hence, detection of ^{12}C^{18}O and ^{13}C^{16}O in the H-band spectra is extremely difficult due to noise issues. For example, Figures 3.1 and 3.2 show the atomic features as well as the wavelength positions of ^{12}C^{18}O and ^{13}C^{16}O band heads.

3.5 Conclusions

Our analysis show the presence of strong ^{18}O band heads in RCB and HdC stars. The HdC star, HD 137613, and the two RCB stars: SV Sge and ES Aql, are common with Clayton et al. (2007). Our ^{16}O/^{18}O estimates for these three stars are in fair agreement with the values given in column (4) of Clayton et al. (2007)'s Table 2.

For DY Persei and the relatively cooler DY Per affiliated stars, our conclusion are less clear, however, there seems to be indication of ^{18}O in the atmosphere of DY Persei and 4 DY Per suspects and no ^{13}C (within the detection limit) which is the main isotopic signature of RCB/HdC stars. In the case of the DY Per type star, V1942 Sgr, numerous features are observed and we could not confirm the presence or absence of both ^{12}C^{18}O and ^{13}C^{16}O bands. Note that, the *K*-band spectra of all the normal carbon stars, with similar S/N spectra of DY Per affiliates, having similar effective temperatures, show prominent ^{13}C^{16}O bands. On the contrary, one DY Per type star ASAS J065113+0222.1, and one DY Per suspect IRAS 05301+1805 show little or no presence of both ^{18}O and ^{13}C in their atmosphere.

So whether DY Per type stars are the cooler cousins of RCBs or just a counterpart of normal carbon rich AGBs suffering ejection events can be better explored through the analyses of high resolution *H*- and *K*-band spectra. Our preliminary analysis suggests that a quartet of suspects along with DY Persei itself show prominent ^{12}C^{18}O bands and no ^{13}C^{16}O bands, which is in sharp contrast to the normal carbon stars and much similar to RCBs, and builds up a strong case to dig deeper into the high resolution spectra of these stars to find their evolutionary origins.

Chapter 4

Detection of flourine in hot Extreme Helium Stars[1]

An overview

The main objective of this work is to explore abundances of fluorine in hot Extreme Helium Stars (EHes). Overabundance of fluorine is a characteristic feature for cool EHes and R Coronae Borealis (RCB) stars and further enforces their close connection. For hot EHes this relationship with the cooler EHes, based on their fluorine abundance is unexplored. We present in this work the first abundance estimates of fluorine determined from singly ionised fluorine lines (F II) for 10 hot EHe stars from optical spectra. Fluorine abundances were determined using the F II lines in two windows centered at 3505 Å and 3850 Å. Six of the 10 stars show significant enhancement of fluorine similar to the cool EHes. Two carbon-poor hot EHes show no signature of fluorine and have a significant low upper limit for the F abundance. These fluorine abundances are compared with the other elemental abundances observed in these stars which provide an idea about the formation and evolution of these stars. The trends of fluorine with C, O, and Ne show that significant helium burning after a CO-He white dwarf merger can

---

[1] The contents of this chapter is based on the publication (Bhowmick et al. 2020)

account for a majority of the observed abundances. Predictions from simulations of white dwarf mergers are discussed in light of the observed abundances.

4.1 Introduction

Extreme helium stars (EHes) are helium rich, A and B-type H-deficient supergiants having observed surface composition similar to the cooler hydrogen deficient stars, namely the R Coronae Borealis (RCB) and hydrogen deficient carbon (HdC) stars. Alongwith sharing extreme hydrogen deficiency, they also exhibit common peculiar aspects of their chemical compositions.

As mentioned in Chapter-1, Section-1.2.4, the two most notable chemical peculiarities shared by these H-deficient stars are (i) the extreme overabundance of ^{18}O in HdC and cool RCBs such that ^{18}O/^{16}O > 1 (Clayton et al. 2007) and (ii) a startling overabundance of F in RCBs and cool EHes such that F relative to Fe is enhanced by 800 to 8000 times(Pandey 2006; Pandey et al. 2008; Hema et al. 2017) with respect to sun. It is of great interest to determine, if these peculiarities extend to the hot EHes. This work addresses the F abundance of the hot EHes.

EHes are rare in the Galaxy with only 22 discovered (Jeffery et al. 1996; Jeffery 2017) till date. There are about 17 known hot EHes with effective temperatures hotter than about 14000 K, the focus of this work. Ten hot EHes are examined here. For the hot EHes, nothing is known about the two notable abundance anomalies of the H-deficient cool stars, i.e., ^{18}O and F. Since the O isotopic abundances are determined from CO lines in the infrared spectrum and CO molecules cannot exist in the atmospheres of hot (or cool) EHes, the O isotopic abundances are unobtainable for EHes. (Isotopic wavelength shifts for O I and O II lines are negligible.) Fluorine abundances are, however, obtainable for EHes.

The chemical compositions derived from their observed spectra suggest a hydrogen-deficient atmosphere including material exposed to both H- and He-burning. Based on their observed surface compositions two principal theories (see Chapter-1, Section-1.4) are in place to explain their origins: the “double-degenerate” (DD) model and the “final-flash” (FF) model. Based primarily on the fluorine, neon, ^{13}C, and ^{18}O abundances, a consensus is now emerging for the DD scenario (Chapter-1, Section-1.4.2), however, a small fraction may be produced by FF scenario (Chapter-1, Section-1.4.1).

Simulations predict that a CO-He white dwarf merger in the DD scenario may produce conditions for partial helium burning which results in production of ^{18}O via $^{14}\mathrm{N}(\alpha,\gamma)^{18}\mathrm{F}(\beta^{+}\nu)^{18}\mathrm{O}$ and of ^{19}F, the sole stable isotope of F (Clayton et al. 2007). Hence, the knowledge of the fluorine abundance and its relation to the other abundant species found in these stars plays an important role in discovering the nucleosynthesis processes taking place during and following helium accretion on to the C-O or He white dwarf in the DD scenario.

If the suite of abundance peculiarities is seen to be common across the HdC, RCB and EHe, primarily a sequence of increasing effective temperature, a common formation scenario would seem a likely scenario. As noted above, the ^{18}O anomaly cannot be investigated in EHes. The F anomaly is determinable across the sequence. For warm RCBs and the cooler EHes, neutral fluorine (F I) lines have provided the high F overabundances (Pandey 2006; Pandey et al. 2008; Hema et al. 2017). For hot EHes, the F I lines are undetectable in optical spectra but lines of ionized fluorine should be present in ultraviolet (3500-3900 Å) spectra if the F abundance is anomalous. To date, the only confirmed detection of F II lines in a H-deficient star is Pandey et al. (2014)’s detection of F II lines at 3500-3510 Å in a spectrum of the hot EHe/hot RCB DY Cen. However, DY Cen is an odd H-deficient star in that it has a relatively high hydrogen abundance. Detection of fluorine in other hot EHes has yet to be explored. Here we report F abundances (or upper limits) for ten hot EHes.

The chapter is organized as follows: Section-4.2 discusses the observations, Section-4.3 addresses the identification of the F II lines, Section-4.4 presents the abundance analysis and discusses the relations between the F and some other elemental abundances. Section-4.5 discusses the compositions of the hot EHes and other H-deficient stars in the light of predictions from simulations of the DD scenario. Section-4.6 concludes the chapter with a few final remarks.

4.2 Observation

High resolution optical *é*chelle spectra of ten hot EHes come from HCT-HESP, ESO-FEROS and ESO-UVES, and McDonald Observatory, as discussed below. All but two stars (DY Cen and V1920 Cyg) were observed with more than one telescope/spectrograph combination (see Table 4.1).

We observed three hot EHes: V652 Her, V2205 Oph and BD +10° 2179 using Hanle Echelle Spectrograph (HESP) (see Chapter-2, Section-2.2.1.2 for details) mounted on the 2-m Himalayana Chandra Telescope (HCT) at the Indian Astronomical Observatory (IAO) in Hanle, Ladakh, India during 2017 and 2018 to look specifically for F II lines in the 3500Å and 3800Å regions. The observing details are in Table 4.1. Standard procedures were followed for observation and processing of data (see Chapter-2, Section-2.3). The final wavelength calibrated spectra of these three stars V652 Her, V2205 Oph and BD +10° 2179 were combined (see below) with spectra from the ESO Data Archives.

We also retrieved high resolution optical spectra of ten hot EHes from the European Southern Observatory (ESO) Data Archives[2]. These observations were made with ESO Telescopes at the La Silla and the Paranal Observatory under programme IDs 077.D−0458, 284.D−5048, and 074B−0455. The spectra were recorded using FEROS (see Chapter-2, Section-2.2.2.1 for details) on ESO 2.2m

---

[2] `http://archive.eso.org/wdb/wdb/adp/phase3_main/form`

TABLE 4.1: Log of observations of the EHe stars.

Star name	Date of observation	Exposure time(secs)	V-mag	S/N (3500Å)	S/N(3800Å)	Source of spectra	$R = \lambda/\Delta\lambda$
LS IV+6° 2	2006-03-31	2000	12.2	120		UVES	40000
	2006-04-21	2980	12.2		175	FEROS	45000
V652 Her	2005-03-01	600	10.5		110	FEROS	45000
	2017-06-04	2700(5)	10.5		65	HESP	28000
	2018-04-22	2700(3)	10.5		40	HESP	28000
DY Cen	2010-02-27	1800	12.5	140	120	UVES	40000
V2205 Oph	2005-02-26	600	10.5		100	FEROS	45000
	2017-06-04	2400(4)	10.5		60	HESP	28000
	2018-05-09	2400(3)	10.5		50	HESP	29000
	2018-05-10	2400(3)	10.5		38	HESP	29000
	2018-05-20	2400(3)	10.5		35	HESP	29000
HD 144941	2006-04-10	780	10.1	270		UVES	40000
	2006-01-08	3000	10.1		250	FEROS	45000
LSE 78	2006-01-10	1500	11.2	155		UVES	40000
	2006-04-09	2400	11.2		170	FEROS	45000
BD +10° 2179	2006-05-10	1000	10.0	220		UVES	40000
	2006-04-12	2820	10.0		210	FEROS	45000
	2018-01-13	2400(3)	10.0		95	HESP	29000
	2018-02-10	2400(3)	10.0		110	HESP	29000
	2018-03-27	2400(3)	10.0		80	HESP	29000
V1920 Cyg	1996-07-25	1800	10.3		110	McDonald	48000
HD 124448	2006-04-10	975	10.0	190		UVES	40000
	2006-04-08	2820	10.0		200	FEROS	45000
PV Tel	2006-04-08	1500	9.3		180	FEROS	45000

telescope in La Silla, Chile and UVES (see Chapter-2, Section-2.2.2.2 for details) on ESO Very Large Telescope (VLT) at Paranal, Chile. The details are given in Table 4.1.

The spectrum of hot EHe star V1920 Cyg was observed using the W.J. McDonald Observatory's Harlan J. Smith 2.7-m telescope with the Robert G. Tull cross-dispersed *é*chelle spectrograph (see Chapter-2, Section-2.2.2.3 for details) during 1996 at a resolving power of about 30,000 (Tull et al. 1995). V1920 Cyg's spectrum is discussed in (Pandey et al. 2006), and the relevant details are also provided in Table 4.1).

Spectra retrieved from archival data and those obtained from HESP were further smoothed to increase the signal-to-noise ratio. Note that the spectra were smoothed to the limit that the stellar line profiles remain unaltered. To ensure this, the smoothed spectrum was compared with the unsmoothed one. The resolving power of the smoothed spectrum was determined by measuring the FWHM of telluric lines in the 6925Å region. If telluric lines were not available for determining the spectral resolution of the smoothed spectra, the reported resolving power in the archives was used by taking into account the smoothening factor.

Table 4.2: Details of the spectra

Star name	Wavelength window			
	3505Å		3850Å	
	S/N	R($\lambda/\Delta\lambda$)	S/N	R($\lambda/\Delta\lambda$)
LS IV+6° 2	225	35000	260	37500
V652 Her	···	···	175	26000
DY Cen	160	33000	210	31000
V2205 Oph	···	···	320	27000
HD 144941	370	38000	340	37000
LSE 78	280	36000	220	36000
BD +10° 2179	320	38000	280	28000
V1920 Cyg	···	···	140	30000
HD 124448	220	39000	240	37500
PV Tel	···	···	220	38000

Frames with symmetric absorption line profiles and with minimum core emission were chosen for analysis; many EHes show variable spectra with radial velocity changes, variable line profiles and even emission features. The spectra obtained from each individual frames were compared to check for the presence of any artifact. The signal in the spectra obtained through HESP was very low in 3500Å region, hence, we have used only the spectral region above 3800 Å region for analysis. To further improve the signal-to-noise, the spectrum from archival data and that from HESP, if available, were co-added for final analysis. Note that the observed spectra are brought to the rest wavelength using well known stellar lines. The details of the final co-added spectra are given in Table 4.2.

4.3 Identification of F II lines

Multiplets numbered 1, 2, 3, 4, and 5 in the Revised Multiplet Table of Moore (1972) and by Wiese et al. (1966) are the potential contributors of F II absorption lines to the spectra of hot EHe stars. A complete list of the transitions that includes their wavelengths, lower excitation potential, and log-gf values for lines of these multiplets was compiled from the NIST database [3].

Four F II lines were identified as the main or significant contributor to stellar lines (see Table 4.3). These four lines consist of all three lines of muliplet 1– 3847.086 Å, 3849.986 Å, and 3851.667 Å and the fourth line centered at 3505.614 Å of multiplet 3. Note that the F II line profile at 3505.614 Å which appears as one, is a blend of 3 components 3505.614 Å, 3505.52 Å, and 3505.37 Å (see Table 4.3). Lines at 3849.986 Å of multiplet 1 and 3505.614 Å of multiplet 3 are relatively free of blends and are best suited for determining the F abundance (see Table 4.3). All the lines of multiplets 1 and 3 are shown in Figures 4.1 and 4.2, where the spectra of hot EHes are ordered from top to bottom in order of decreasing effective temperature. The wavelength windows corresponding to Figures 4.1 and 4.2 are centered around 3505 Å and 3850 Å, respectively. Note that the spectra of V652 Her, V2205 Oph, and V1920 Cyg were not available or were very noisy in the window 3490-3520 Å. Also for the other multiplets of F II lines, a thorough search was conducted for the blending lines and strong blending of lines from other atomic species is noted (see Table 4.3). These multiplets were not selected

---

[3] `https://physics.nist.gov/PhysRefData/ASD/lines_form.html`

Table 4.3: F II lines from 3s − 3p and 3p − 3d transition array contributing to the spectra of the analysed stars. The F II lines used in abundance determinations are shown in bold.

Multiplet No.	λ Å	χ (ev)	log gf	Likely contributors
1	**3847.086**	21.88	0.31	F II, N II λ 3847.38
	3849.986	21.88	0.16	F II, Mg II(weak) λ 3850.40
	3851.667	21.88	−0.06	F II, O II λ 3851.47
2	4024.727	22.67	0.16	F II , He I , λ 4023.986 , 4026.189, 4026.362 (very strong)
	4025.010	22.67	−0.54	F II , He I , λ 4023.986 , 4026.189, 4026.362 (very strong)
	4025.495	22.67	−0.06	F II , He I , λ 4023.986 , 4026.189, 4026.362 (very strong)
3	**3505.614**	25.10	0.676	F II
	3505.520	25.10	0.09	F II
	3505.370	25.10	−0.757	F II
	3503.095	25.10	0.391	F II, Ne II λ 3503.61
	3502.954	25.10	0.187	F II, He I λ 3502.393 (strong)
	3501.416	25.10	0.074	F II, He I λ 3498.659 (very strong) , Fe III λ 3501.767
4	4103.525	25.75	0.559	F II, O II λ 4103.017, N III λ 4103.37 (strong)
	4103.085	25.75	0.289	F II, O II λ 4103.017, N III λ 4103.37 (strong)
	4103.724	25.75	−0.064	F II, N III λ 4103.37 (strong)
	4103.871	25.75	−0.19	F II N III λ 4103.37 (strong)
5	4109.173	26.26	0.45	F II, O II λ 4108.75 , Mg II, λ 4109.54
	4116.547	26.27	0.18	F II, Si IV λ 4116.104 (strong)
	4119.219	26.27	−0.01	F II, O II λ 4119.221 (strong)

for measuring the fluorine abundance: multiplet 2 is heavily blended with a Stark broadened strong He I line profile, multiplet 4 and 5 are blended severely by lines of other elements. The blended lines were identified using the Revised Multiplet Table (Moore 1972), Tables of spectra of H, C, N, and O (Moore 1993), and the NIST Atomic Spectra Database [4] that also provides the line's gf-value.

---

[4] `https://physics.nist.gov/PhysRefData/ASD/lines_form.html`

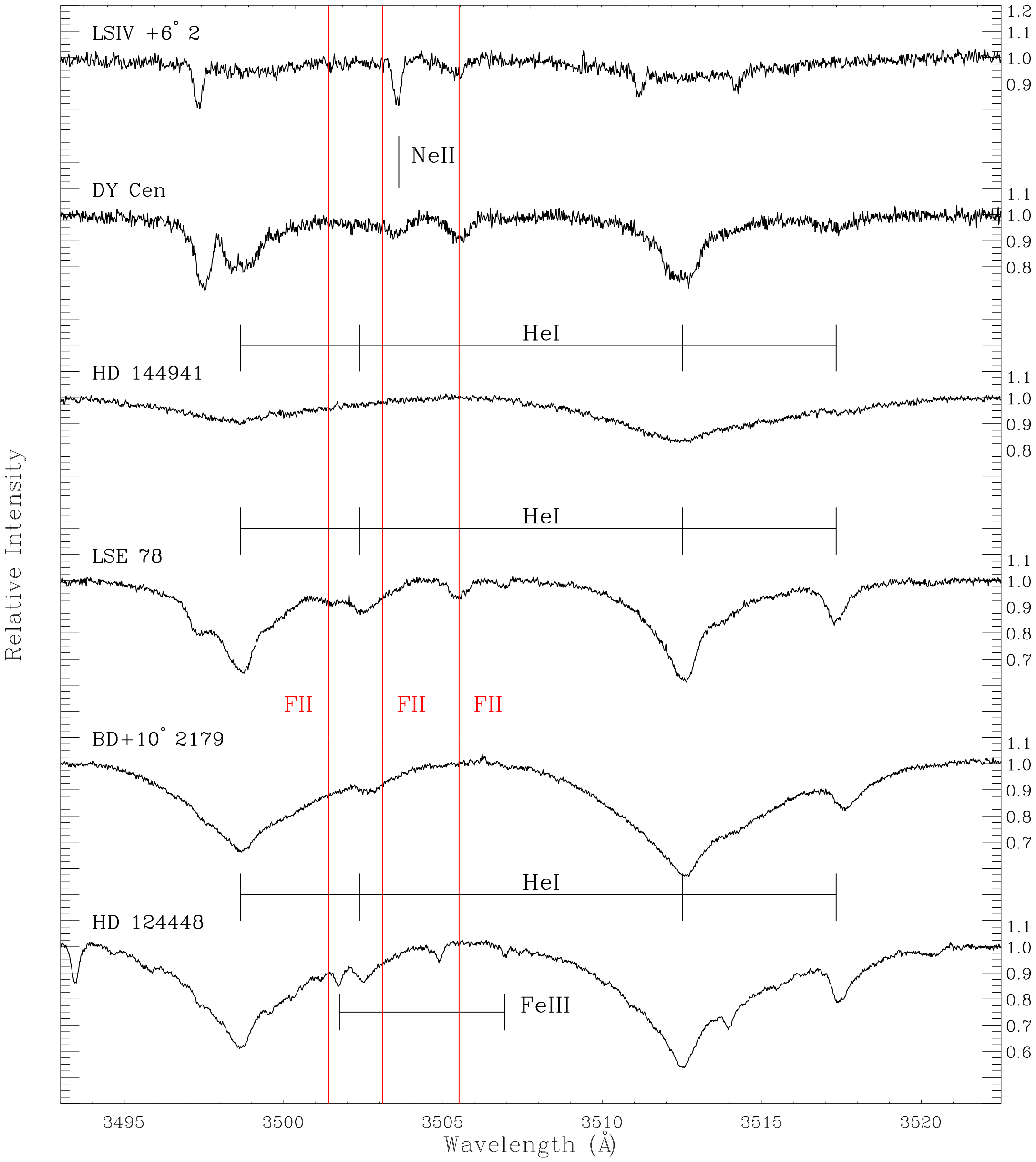

FIGURE 4.1: Comparison of the spectra with key identifications in 3505 Å region. The stars are arranged according to their effective temperature with hottest on the top and coolest at the bottom. The red lines represents the F II lines of RMT 3 in this window.

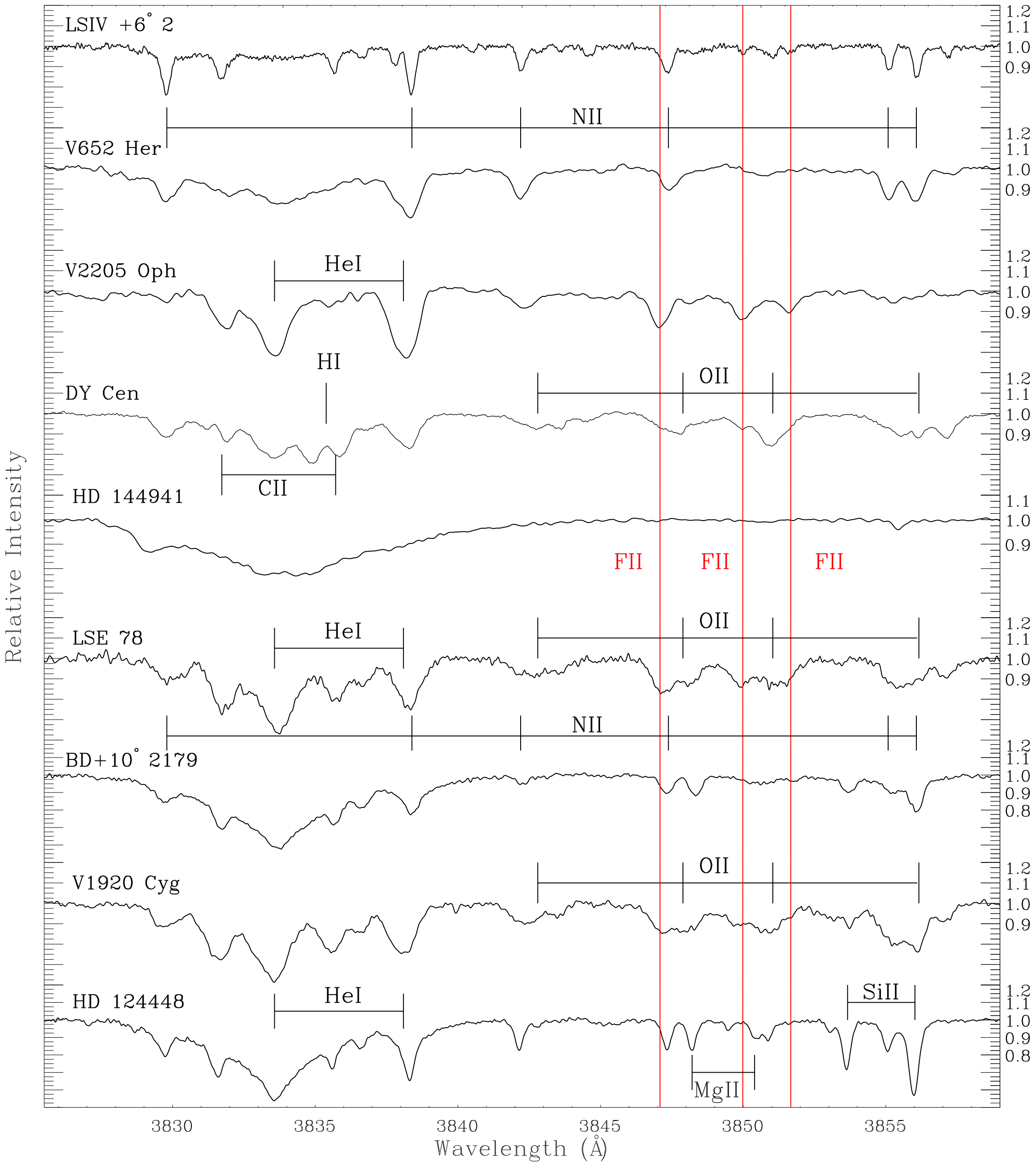

FIGURE 4.2: Comparison of the spectra with key identifications in 3850 Å region. The stars are arranged according to their effective temperature with hottest on the top and coolest at the bottom. The red lines represents the F II lines of RMT 1 in this window.

4.4 Abundance analysis

The abundance of an element X in normal stars is quoted with respect to hydrogen (i.e., X/H) due to hydrogen being the main contributor to the continuous opacity directly or indirectly as well as the most abundant element in their atmospheres. A measure of fractional abundance for the element X is also given by the mass fraction, Z(X) where

$$Z(X) = \frac{\mu_X N_X}{\mu_H N_H + \mu_{He} N_{He} + ... + \mu_i N_i} = \frac{\mu_X N_X}{(\sum \mu_i N_i)} \tag{4.1}$$

$$\simeq \frac{\mu_X A_X}{1 + 4A_{He}} \tag{4.2}$$

where μ_X is the atomic weight of element X, and A$_X$ = X/H. Hence, Z(X) is directly estimated from A$_X$, a result of abundance analysis of the observed spectrum, and an assumption about A$_{He}$ if helium lines are not observable.

For the case of hydrogen-poor stars like the hot EHes, helium may be the main contributor to the continuum opacity directly or indirectly and also the most abundant element in their atmospheres where the H/He ratio has been changed by the addition of nuclear-processed material from H- and He-burning layers. Thus, the abundance of an element X is determined with respect to helium i.e., X/He = A$'_X$, the equation 1 reduces to

$$Z(X) = \frac{\mu_X A'_X}{H/He + 4 + 12C/He + ..\mu_i A'_i} \tag{4.3}$$

Due to hydrogen being very poor in these stars, H/He is very small and like other trace elements can be ignored, then the above equation reduces to,

$$Z(X) \simeq \frac{\mu_X A'_X}{4 + 12C/He} \tag{4.4}$$

The C/He can be spectroscopically determined for hot EHes ($\simeq$ 0.01), and also the abundance of any element X for a hot hydrogen-deficient star like hot EHes, can be directly measured spectroscopically i.e., A'_X = X/He.

Due to the conservation of nucleons during different stages of nuclear burning, the derived abundances are normalised based on the convention that $\log\epsilon$(X) = $\log(X/H)$ + 12.0 to a scale in which $\log\sum\mu_i\epsilon(i)$ = 12.15, where 12.15 is determined from solar abundances with He/H $\simeq$ 0.1. Based on this normalisation convention, and considering X/He as the measure of abundance of an element X in hot H-poor or hot EHe stars, the helium abundance $\log\epsilon$(He) is about 11.54 from equation 4.4.

The F abundance is derived from the four best F II lines (Table 4.3). Since these lines are subject to blending, spectrum synthesis was used to locate a F II line's contribution. The code SYNSPEC (Hubeny et al. 1994) was used with the LTE model atmospheres of individual stars (see Table 4.4) from Pandey et al. (2006); Pandey & Lambert (2011); Pandey et al. (2014); Pandey & Lambert (2017). Synthetic spectra were convolved with the instrumental profile and the broadening corresponding to the rotational velocity derived from weak and symmetric O II or N II lines in the star's spectrum. All the key lines were used to compose a line list for spectrum synthesis. Selected lines of several elements were synthesized. Derived LTE abundances are in fair agreement with those reported in our earlier abundance analyses (Pandey et al. 2006; Pandey & Lambert 2011; Pandey et al. 2014; Pandey & Lambert 2017). Adopted model atmospheres (T_{eff} = effective temperature, log$g$ = surface gravity, ξ = microturbulence) and the F abundances from the individual F II lines and the line-to-line scatter are given in Table 4.4. Abundances of other elements (C, N, O, Ne, Fe and Zr) are given in Table 4.5.

The two spectral regions providing the F II lines are displayed in Figures 4.1 and 4.2 with the EHes arranged in order of decreasing effective temperature from top to bottom. By inspection, it is obvious that the F II lines do not vary smoothly with effective temperature; the F abundance can be greatly different in stars of

TABLE 4.4: Derived abundances of fluorine in hot EHes.

Star name	(T_{eff}, log$g$, ξ)	logϵ(F)						
		3847.086 Å	3849.986 Å	3851.667 Å	3505.614 Å	Mean	σ_1[a]	σ_2[b]
LS IV+6° 2	(32000, 4.20, 9.0)[1]	6.5	6.4	6.4	6.6	6.5	0.1	±0.1
V652 Her	(25300, 3.25, 13.0)[2]	< 5.7	< 5.5	< 5.6	···	< 5.6	···	···
V2205 Oph	(24800, 2.85, 23.0)[1]	7.0	7.0	7.0	···	7.0	0.1	± 0.1
DY Cen	(24750, 2.65, 24.0)[4]	6.7	6.9	6.8	7.0	6.9	0.1	± 0.2
HD 144941	(21000, 3.35, 10.0)[2]	< 5.5	< 5.7	< 5.5	< 5.5	< 5.6	···	···
LSE 78	(18300, 2.2, 16.0)[4]	7.4	7.4	7.4	7.3	7.4	0.1	± 0.2
BD +10° 2179	(17000, 2.6, 7.5)[1]	6.4	6.5	6.4	< 6.5	6.4	0.2	± 0.1
V1920 Cyg	(16300, 1.8, 20)[4]	7.5	7.6	7.5	···	7.5	0.2	± 0.1
HD 124448	(15500, 2.0, 12)[4]	< 6.0	< 6.0	< 6.0	< 6.0	< 6.0	···	···
PV Tel	(13750, 1.6, 25.0)[1]	< 6.5	< 6.5	< 6.5	···	< 6.5	···	···

[a] r.m.s error: $\Delta T_{eff} = \pm$ 500K , Δlog$g$ = ± 0.2 cgs

[b] r.m.s error: line-to-line scatter

[1] (Pandey & Lambert 2011)

[2] (Pandey & Lambert 2017)

[3] (Pandey et al. 2014)

[4] (Pandey et al. 2006)

similar effective temperature. Consider, for example, V652 Her and V2205 Oph in Figure 4.2 with the three F II lines prominent in the spectrum of V2205 Oph but seemingly absent from the spectrum of V652 Her. The two stars have similar atmospheric parameters but F abundances differing by at least 1.5 dex (Table 4.4).

Brief remarks follow on the spectrum syntheses of the F II lines in the individual stars and their F abundances beginning with the hottest star LS IV+6° 002. Observed and synthetic spectra are shown for each star.

LS IV+6° 002. The windows at 3505 Å and 3850 Å are both available for this star. The F abundance is based primarily on the lines at 3849.986 Å and 3851.7 Å with the two weakest lines at 3501.4 Å and 3503.1 Å providing supporting evidence as to the maximum F abundance allowed by these lines (Figure 4.3). The 3847.1 Å line in the blue wing of a strong N II line appears present but assessment of

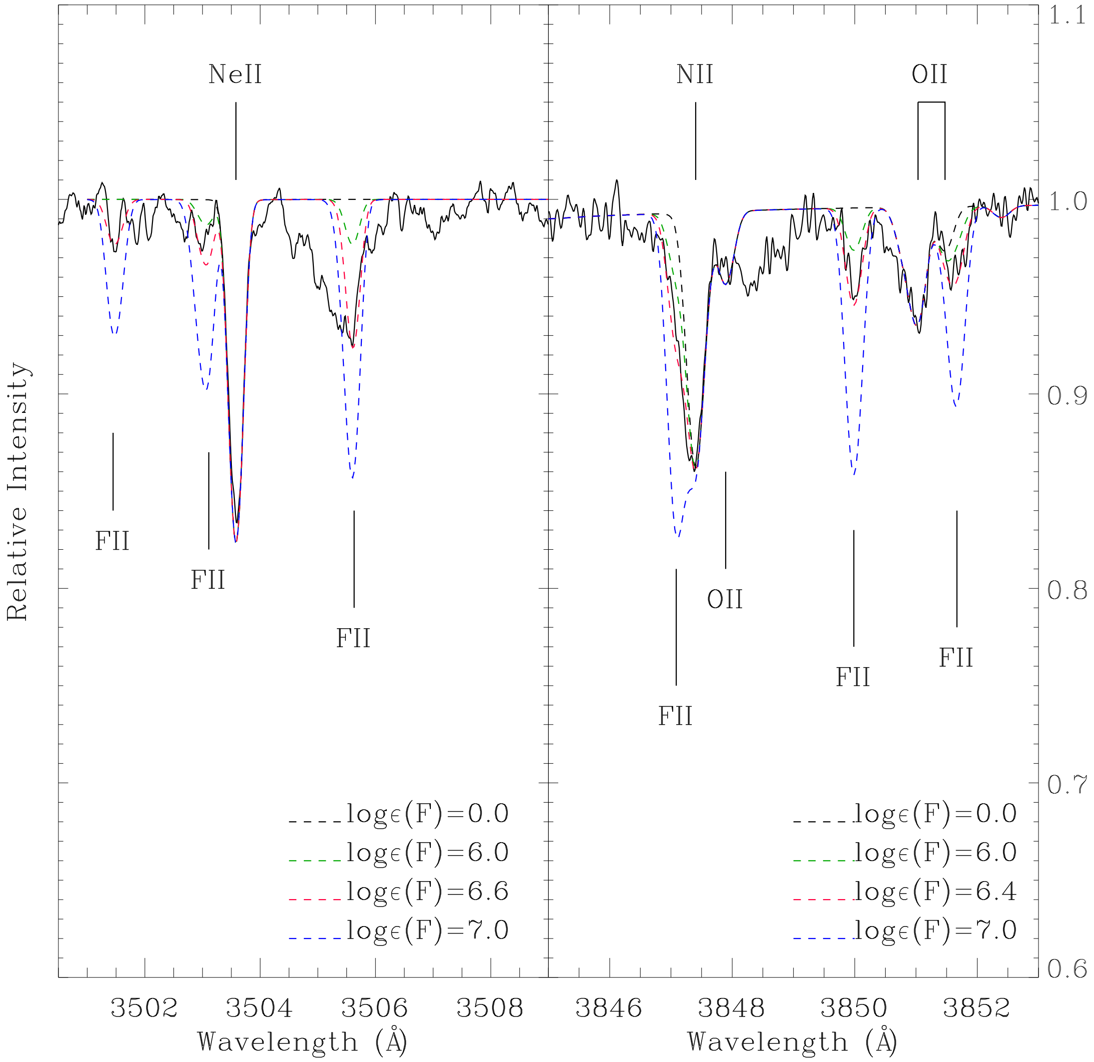

Figure 4.3: Observed F II in 3505 Å and 3850 Å wavelength windows of LS IV+6° 2 (solid line) with key lines marked. Synthetic spectra are shown for four fluorine abundanes.

its strength is dependent on the adopted width of the N II line. The 3505 Å blend of three RMT 3 lines appears to be present at the F abundance provided by other lines but is seriously blended with an unidentified line. The F abundance of $\log \epsilon(\mathrm{F}) = 6.5$ seems appropriate for this star.

V652 Her. Only the 3850 Å window is available. Spectrum synthesis does not provide convincing detection of a F II line (Figure 4.4). An upper limit of $\log \epsilon(\mathrm{F}) = 5.6$ is provided by each of the RMT 1 lines. This star is very clearly

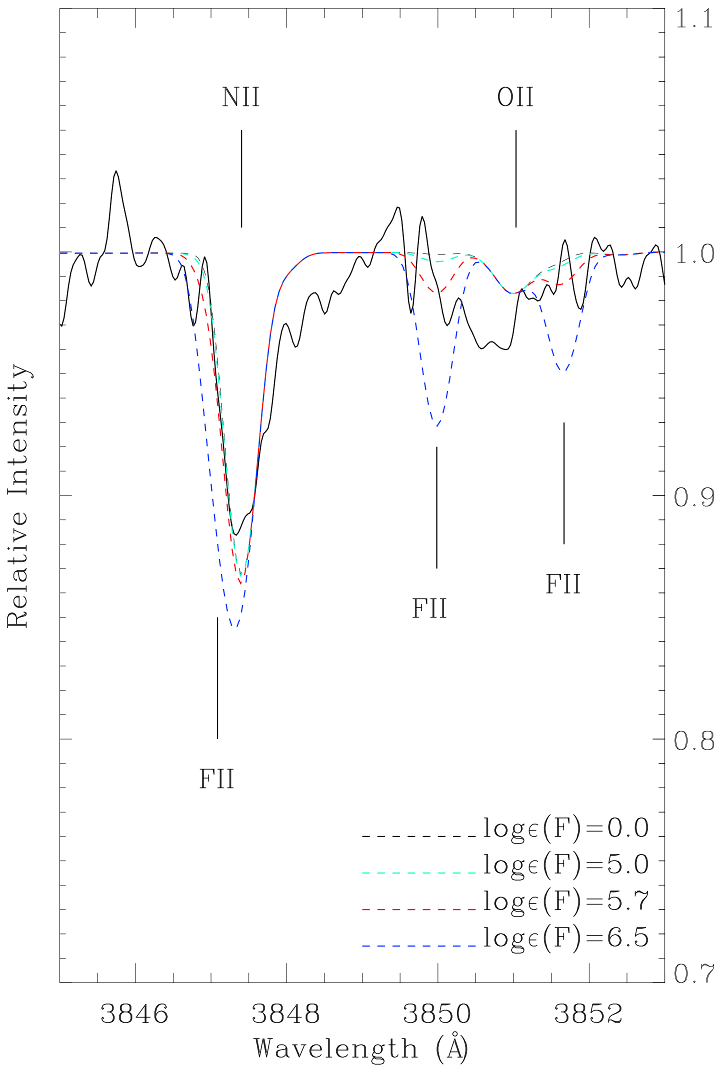

FIGURE 4.4: Observed F II in 3850 Å wavelength window of V652 Her (solid line) with key lines marked. Synthetic spectra are shown for four fluorine abundanes.

F-poor relative to LS IV +6^o 002 (and other F-rich stars).

V2205 Oph. The 3505 Å window is not available. In the 3850 Å window, the three RMT 1 F II lines are clearly present with a consistent abundance of log ϵ(F) = 7.0 (Figure 4.5). Blending lines of N II and O II are pleasingly weak in this star ensuring the consistency of the F abundance from the three lines.

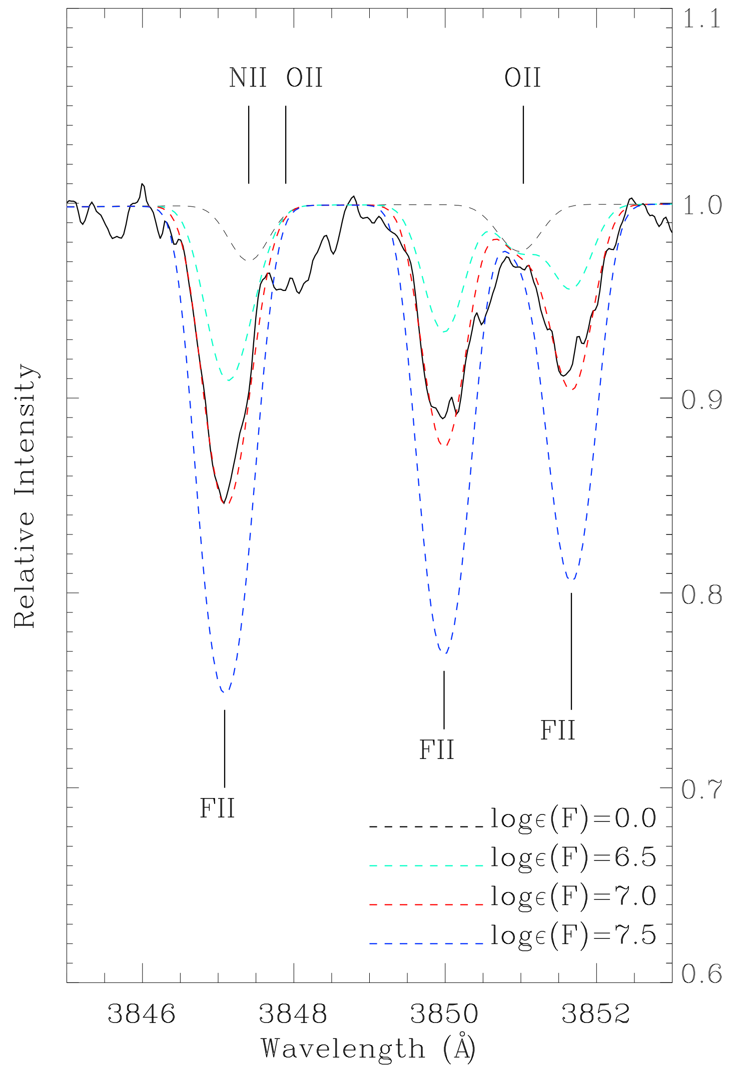

FIGURE 4.5: Observed F II in 3850 Å wavelength window of V2205 Oph (solid line) with key lines marked. Synthetic spectra are shown for four fluorine abundances.

DY Cen. Consistent F abundances are obtained from unblended or relatively unblended lines in both windows (Figure 4.6). The unblended 3505.5 Å line provides the F abundance of $\log \epsilon(\mathrm{F}) = 7$. The other two lines in the RMT 3 are possibly present and consistent with this abundance. In RMT 1, the blending by the N II and O II lines is much stronger than in V2205 Oph (Figure 4.5). The weaker two F II lines of this RMT provide a consistent F abundance which is supported by the 3851.7 Å line now seriously blended with the O II line. A F

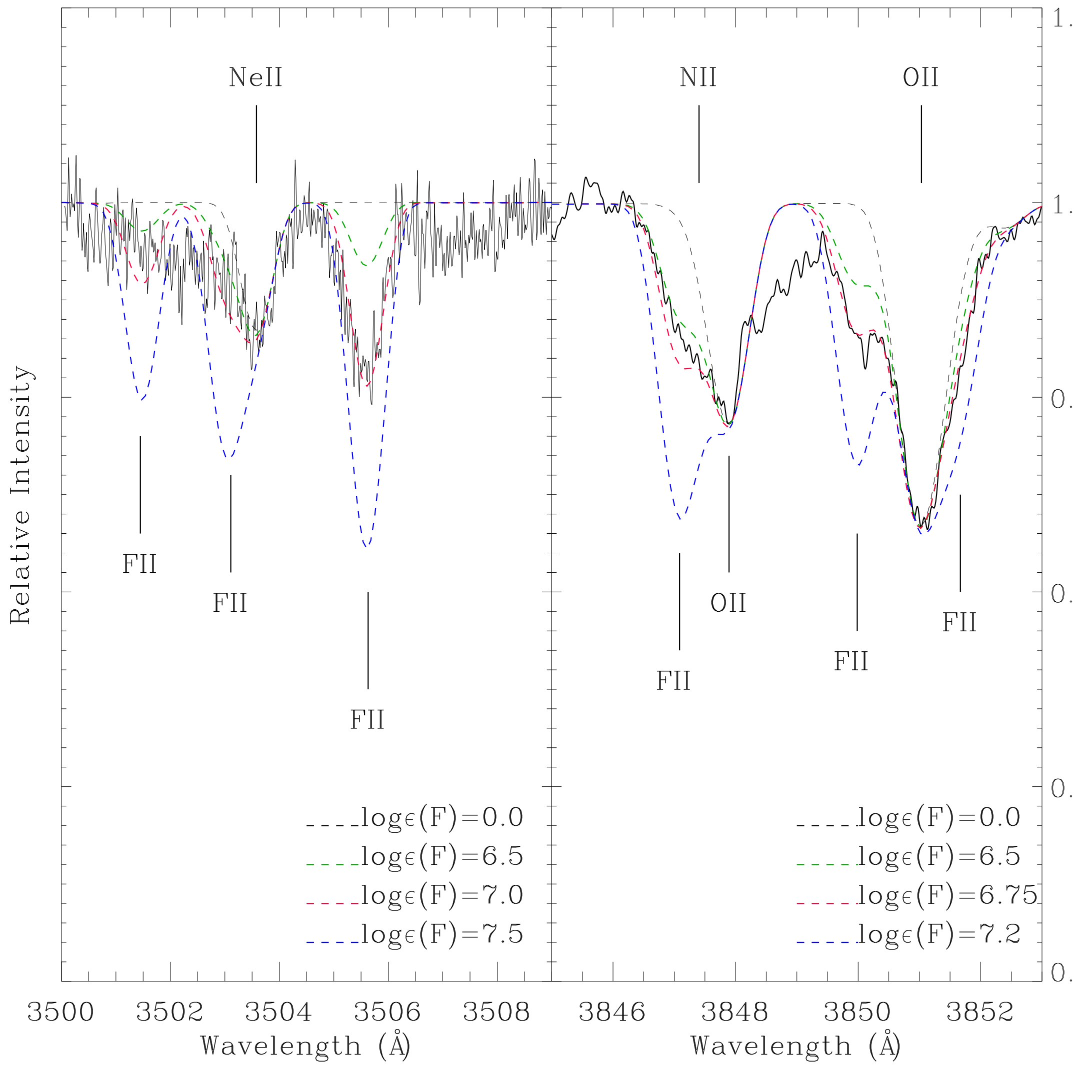

FIGURE 4.6: Observed F II in 3505 Å and 3850 Å wavelength windows of DY Cen (solid line) with key lines marked. Synthetic spectra are shown for four fluorine abundanes.

abundance of log ϵ(F) = 6.9 is recommended.

HD 144941. The wavelength regions centered at 3505Å and 3850Å are available and do not show detectable F II lines in the observed spectrum (see Figure 4.7). An upper limit of log ϵ(F) = 5.6 is obtained by each of RMT 1 and RMT 3 lines. This star is clearly very F-poor and similar to the other carbon poor hot EHe star:V652 Her.

LSE 78. The F abundance is provided by the F II lines at 3505.5 Å from RMT

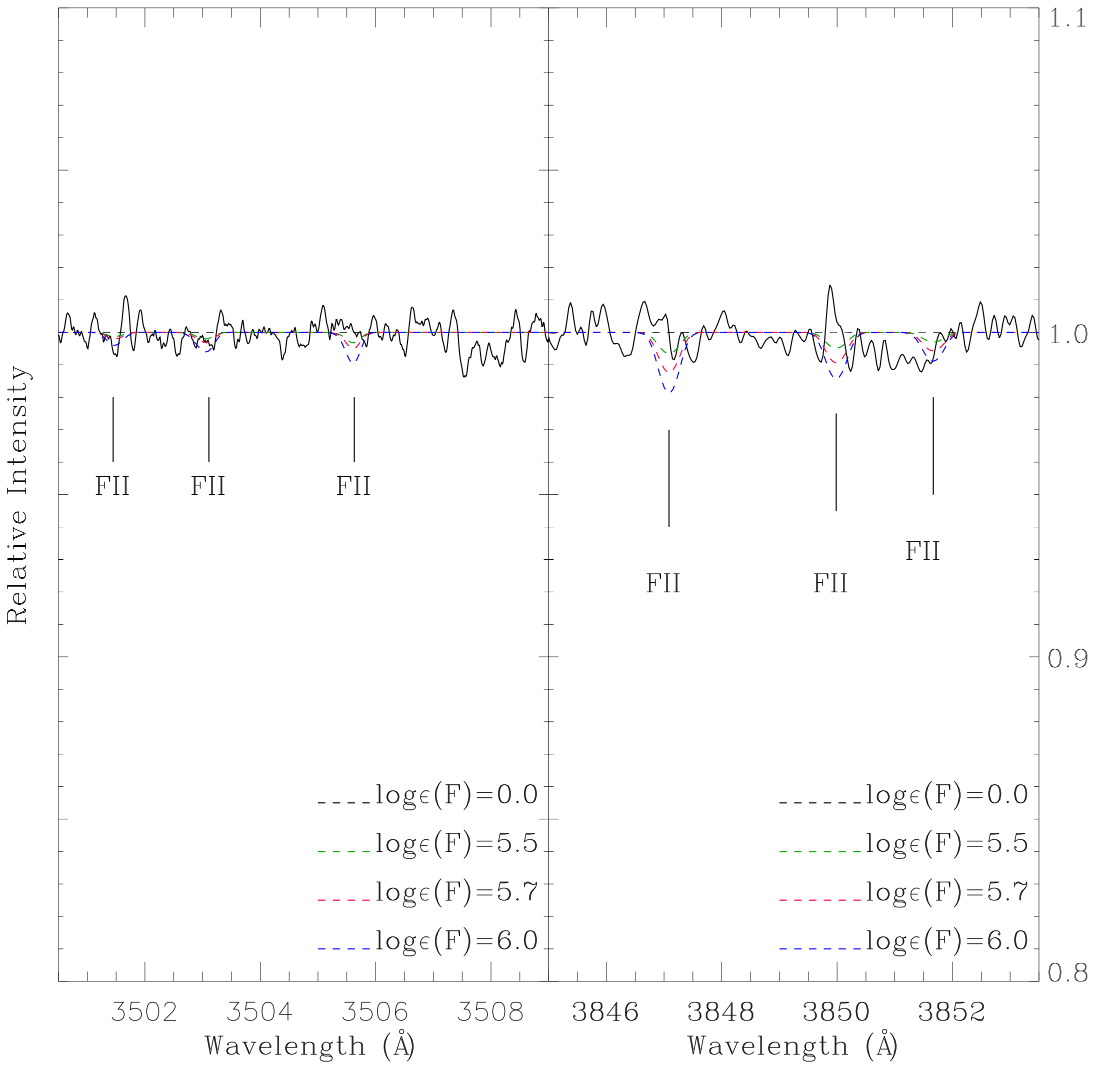

FIGURE 4.7: Observed F II in 3505 Å and 3850 Å wavelength windows of HD 144941 (solid line) with key lines marked. Synthetic spectra are shown for four fluorine abundanes.

3 and the three lines of RMT 1. The F abundance of $\log\epsilon(\mathrm{F}) = 7.4$ reproduces these lines (Figure 4.8).

BD +10° 2179. In both the 3505 Å and 3850 Å windows, the F II lines are weak (Figure 4.9). The 3505.5 Å is not detected and the abundance upper limit for F of $\log\epsilon(\mathrm{F}) = 6.5$ is set. In RMT 3, the cleanest line is at 3851.7 Å and gives the F abundance of about $\log\epsilon(\mathrm{F}) = 6.4$. The other two lines of this RMT are blended but confirm the abundance of 6.4.

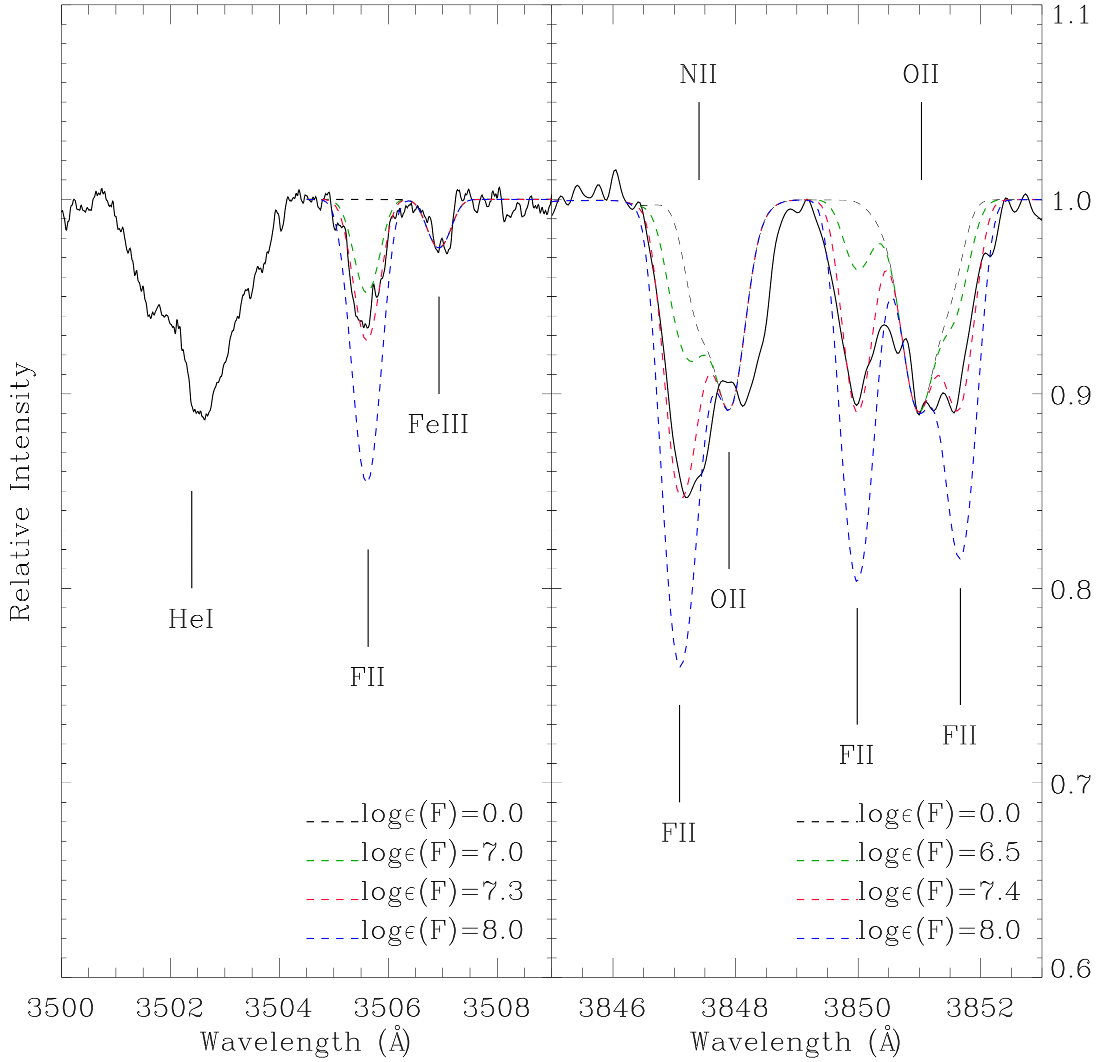

FIGURE 4.8: Observed F II in 3505 Å and 3850 Å wavelength windows of LSE 78 (solid line) with key lines marked. Synthetic spectra are shown for four fluorine abundanes. Note that the He I line at 3502 Å in the left panel of the above figure is not synthesized due to unavailability of log-gf values in NIST database

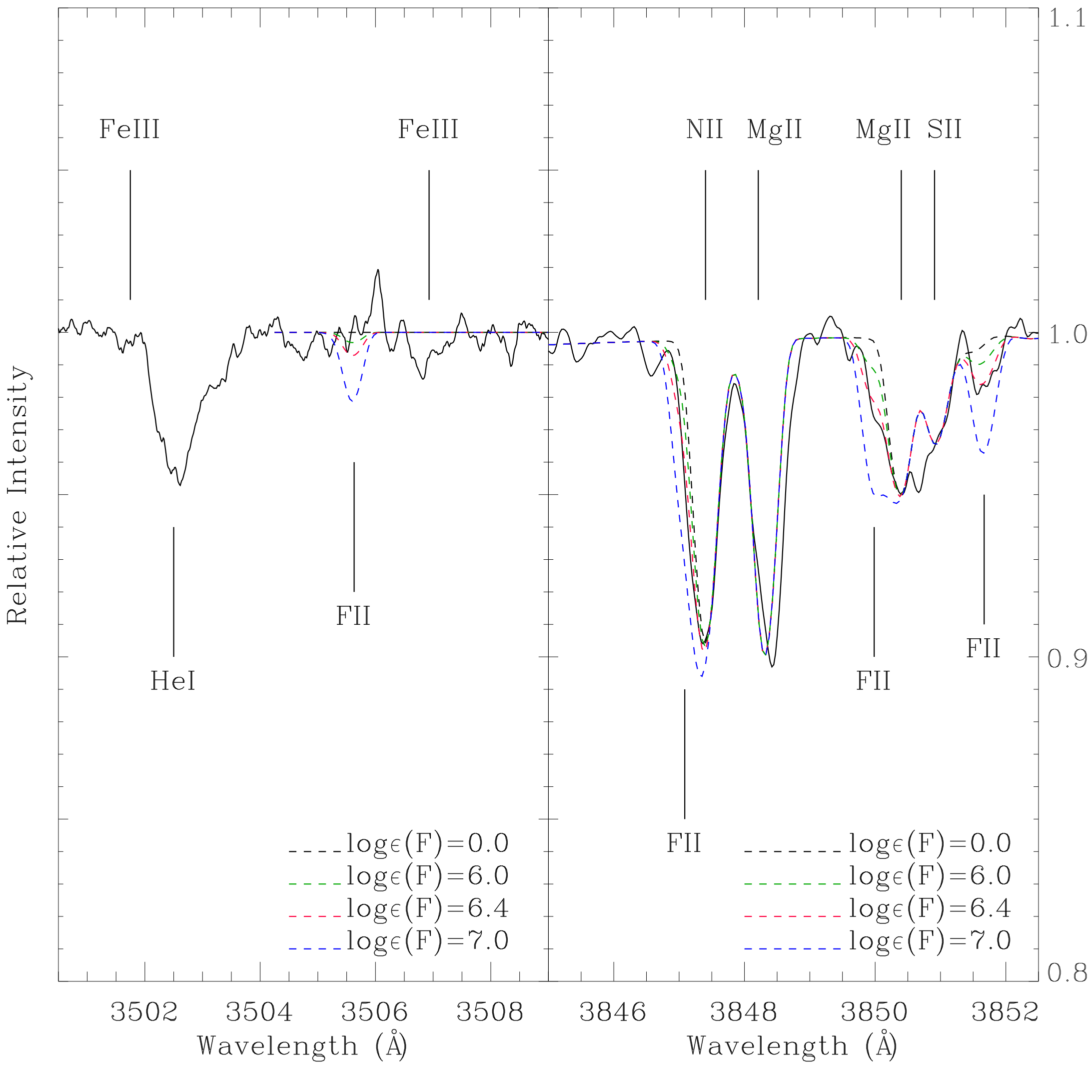

Figure 4.9: Observed F II in 3505 Å and 3850 Å wavelength windows of BD +10° 2179 (solid line) with key lines marked. Synthetic spectra are shown for four fluorine abundanes.

V1920 Cyg. Only the 3850 Å window is available where the three F II lines are blended (Figure 4.10). The least blended line at 3850.0 Å gives the F abundance of $\log \epsilon(\mathrm{F}) = 7.5$, a value consistent with determinations from the two more seriuosly blended lines.

HD 124448. Both wavelength regions are available but neither show evidence for the F II lines (Figure 4.11). The 3505.5 Å is clearly absent. In the 3850 Å window blends are an issue but the 3850.0 Å and 3851.7 Å lines are absent. An

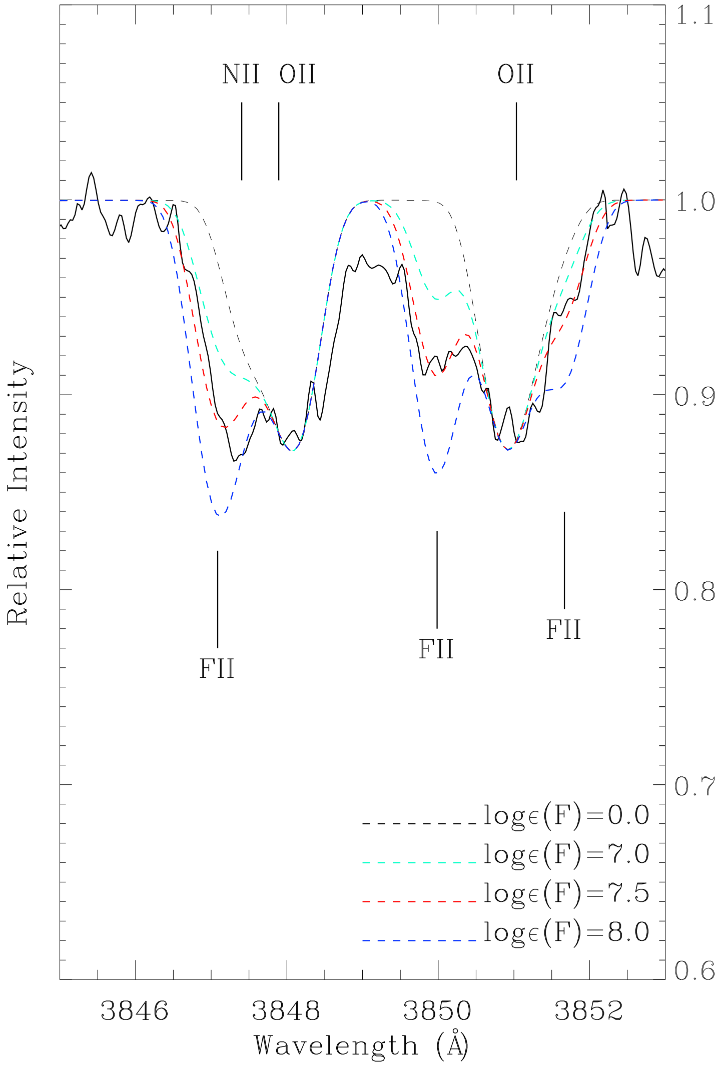

Figure 4.10: Observed F II in 3850 Å wavelength window of V1920 Cyg (solid line) with key lines marked. Synthetic spectra are shown for four fluorine abundances.

upper limit to the F abundance of $\log\epsilon(\mathrm{F}) = 6.0$ may be set.

PV Tel. Only the 3850 Å window is available (Figure 4.12). Spectrum synthesis does not provide convincing detection of a F II line. An upper limit of $\log\epsilon(\mathrm{F}) = 6.5$ is provided by the 3847.1 Å and 3851.7 Å lines.

Our previous investigations of the compositions of hot EHe stars included analyses of the Ne abundance from Ne I and/or Ne II lines. When both neutral and

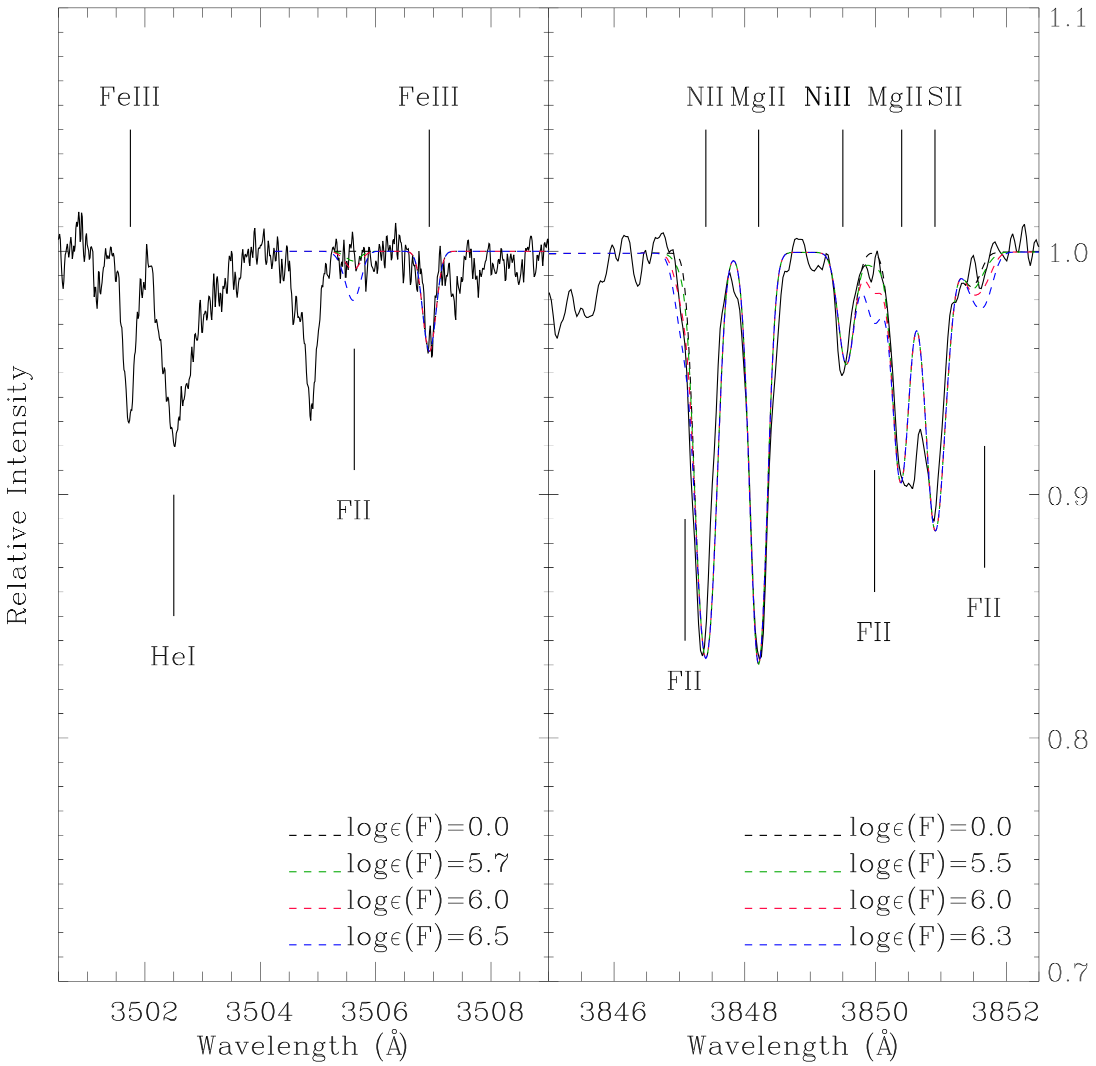

FIGURE 4.11: Observed F II in 3505 Å and 3850 Å wavelength windows of HD 124448 (solid line) with key lines marked. Synthetic spectra are shown for four fluorine abundanes.

singly ionized lines were available, it was found that the Ne abundance from the neutral lines was higher than that from the singly-ionized lines: For example, the LTE neon abundances obtained by Pandey & Lambert (2011) for V2205 Oph from Ne I lines was 0.8 dex higher than obtained from Ne II lines. This difference arises from non-LTE effects principally affecting the Ne I lines, a suggestion thoroughly confirmed by a non-LTE study by Pandey & Lambert (2011). Noting that the atomic structure of the F atom and the detected F I lines are not dissimilar to the Ne atom and the non-LTE affected Ne I lines, we attempted to set limits on the

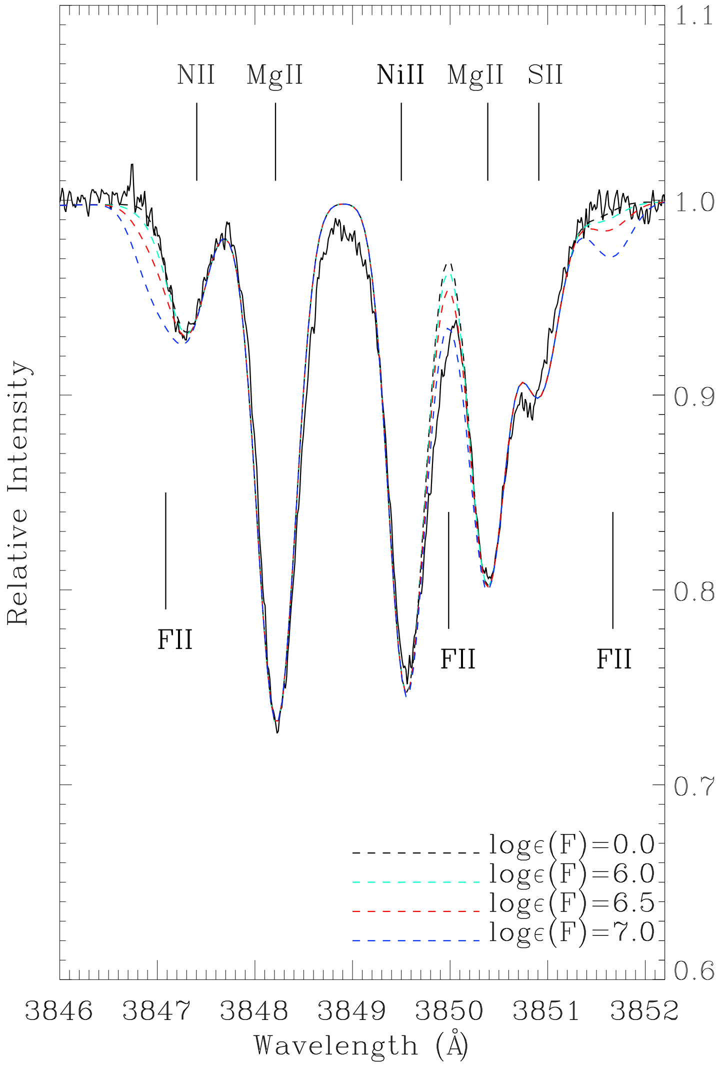

FIGURE 4.12: Observed F II in 3850 Å wavelength window of PV Tel (solid line) with key lines marked. Synthetic spectra are shown for four fluorine abundanes.

non-LTE effects on the F abundances by analysing F I and F II lines in the same star.

In the present sample of hot EHes, examination of the spectrum of V1920 Cyg and LSE 78 led to the detection of the F I at 6856.02 Å line (Figure 4.13 & 4.14) with the estimated F abundance of 7.8 and 7.5, respectively. This F I line at 6856.02 Å is the strongest F I line and the weaker F I lines are consistent with it. The abundance difference between that from the F II and the F I lines is −0.3 and

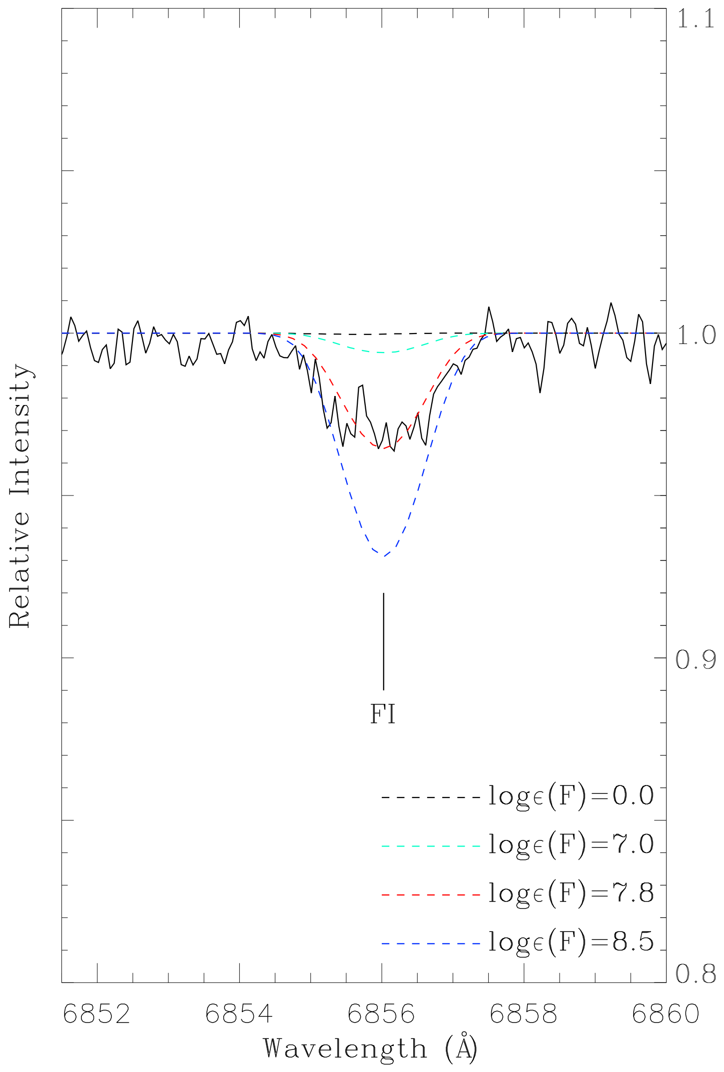

Figure 4.13: Observed F I in 6856 Å region of V1920 Cyg (solid line) with key lines marked. Synthetic spectra are shown for four fluorine abundances.

−0.1 dex for V1920 Cyg and LSE 78, respectively. These differences limit severely the non-LTE effects in the conditions prevailing in both V1920 Cyg and LSE 78. As a complementary effort, we have returned to spectra of the cooler EHes where the F abundance is based on the F I lines to look for F II lines. Two stars had effective temperatures sufficiently high with the available spectra possessing adequate S/N in the blue to provide interesting limits on F II lines: LSS 3378 and PV Tel. For LSS 3378, the F II lines from multiplet 1 provide the upper limit of 8.0 which is consistent with the determination of 7.3 from the F I lines, a comparison which

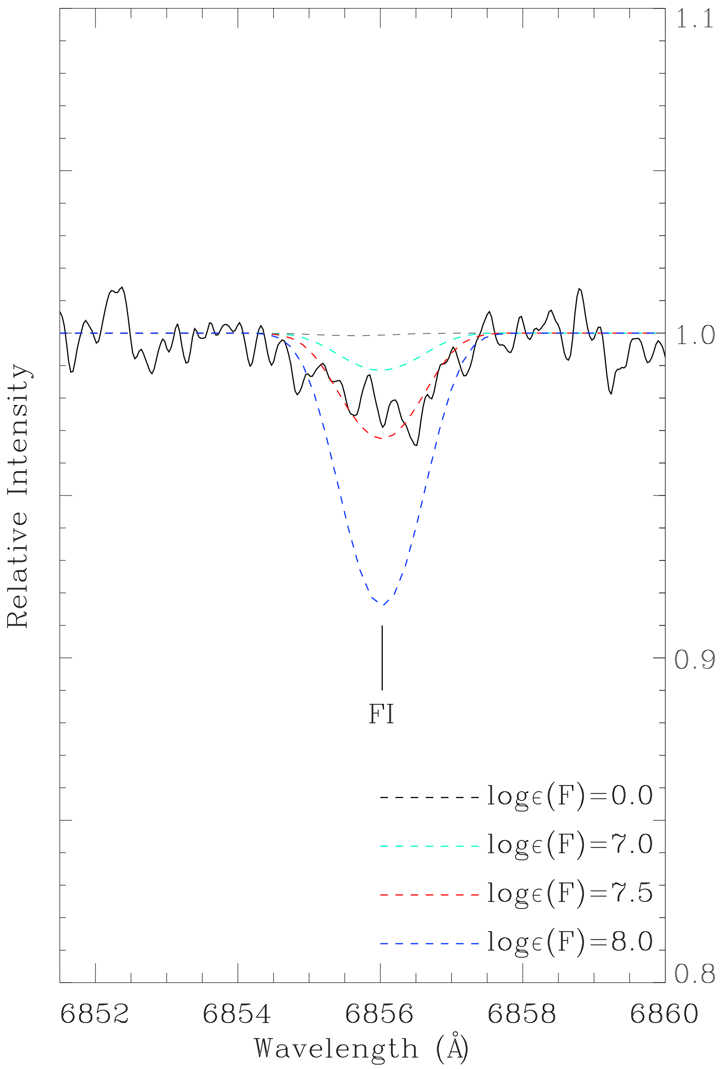

FIGURE 4.14: Observed F I in 6856 Å region of LSE 78 (solid line) with key lines marked. Synthetic spectra are shown for four fluorine abundances.

provides no information on the non-LTE effects. For PV Tel, the F II lines set the upper limit 6.5 which is a significant improvement over the limit (≤ 7.2) reported by Pandey (2006) from the F I lines. Other EHes where - in the future one might get both F I and F II lines are LS IV -1° 002 and LSS 4357. A key point to note is that the level of the F overabundances in the EHes is around a factor of 1000 but the non-LTE effects, if comparable to those on the Ne I lines, are less than a factor of 10. Thus, a very significant overabundance of F in EHes and RCBs is not in doubt because of the present lack of non-LTE calculations for the fluorine atom.

4.4.1 Fluorine enrichment

Fluorine abundances across the sample of ten hot EHes which range from 7.5 to an upper limit of 5.6 are shown in Figure 4.15 as a function of Fe abundance where the two C-poor stars (V652 Her and HD 144941) are distinguished. The F overabundance is remarkable. Fluorine abundances for the cool EHes (Pandey 2006) and the majority and minority RCBs (Pandey et al. 2008; Hema et al. 2017) are added to Figure 4.15. The spread of F abundances across the total sample of H-deficient stars far exceeds the errors of measurement. Figure 4.15 suggests that a few stars may have a F abundance much lower than the typical EHe and RCB. This minority includes the two C-poor hot EHe stars V652 Her and HD 144941, the minority RCB V854 Cen with $\log\epsilon(\mathrm{Fe})=5$, the majority RCB XX Cam and possibly also the hot EHe HD 124448.

In Figure 4.15, the stars' initial F abundance is assumed to correspond to $[\mathrm{F/Fe}] = 0$ over the range $\log\epsilon(\mathrm{Fe})$ from about 7.5 to 5.0 with the trend starting with a solar F abundance of $\log\epsilon(\mathrm{F}) = 4.4$ at $\log\epsilon(\mathrm{Fe}) = 7.5$ (see below). A star's Fe abundance is assumed to be its initial Fe abundance as a H-normal star. Relative to the assumed F-Fe trend, the typical F overabundance at the solar Fe abundance is 500 and this increases to nearly 2000 for the most metal-poor of the H-deficient stars, namely the minority RCBs and the cool EHe FQ Aqr. This is an extraordinary overabundance for any element in any star! The common F overabundance among EHe and RCB stars indicates that, as long suspected, these H-deficient stars are probably closely related. (Fluorine abundances have not been measured for HdC stars.) In sharp contrast, the H-deficient spectroscopic binary KS Per has an upper limit to the F abundance consistent with its initial abundance (Pandey 2006) confirming expectations that massive hot binaries like KS Per have an entirely different evolutionary history to the EHes and their relatives.

Initial abundances for interpretations of F abundances in EHe and RCB stars are based on the solar abundance and abundances in red giants in the Galactic

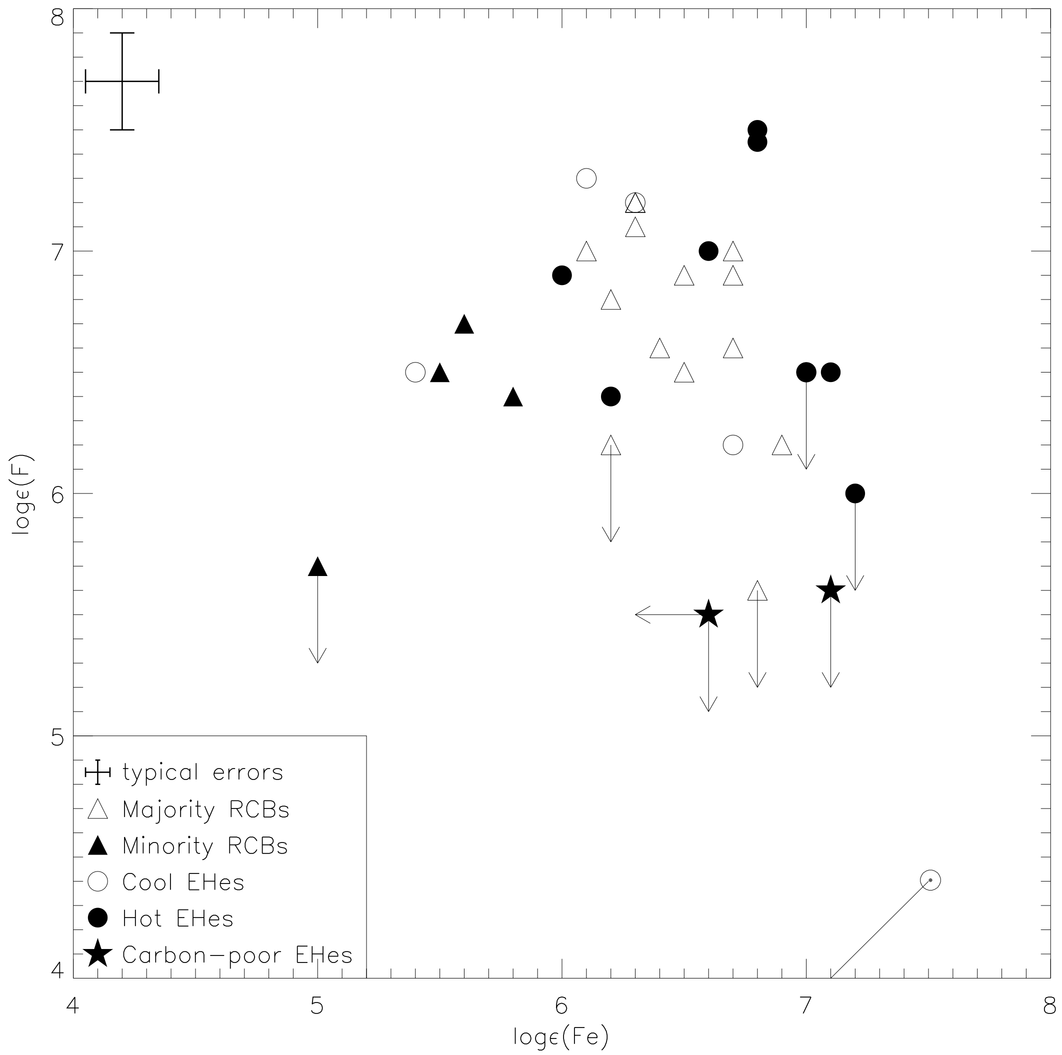

FIGURE 4.15: logϵ(F) versus logϵ(Fe) for hot EHes, cool EHes, and RCBs. The symbols representing different group of stars are showed. The encircled dot symbol represents the sun and the solid line represents locus of the solar F/Fe ratio.

disk. Solar determinations of the F abundance are determined from infrared lines of HF in sunspot spectra: Maiorca et al. (2014) report a solar F abundance of $\log\epsilon(\mathrm{F}) = 4.40\pm0.25$ in fine agreement with the abundance of 4.42 ± 0.06 obtained from meteorites (Lodders et al. 2009). F abundance measurements from HF lines in spectra of red giants in the Galaxy suggest that $[\mathrm{F/Fe}] \simeq 0.0$ over the [Fe/H] interval 0 to -1.5 spanning the interval covered by the EHe and RCB stars (Nault & Pilachowski 2013; Li et al. 2013; Maiorca et al. 2014; Jönsson et al. 2014; Jönsson et al. 2017; Guerço et al. 2019). Current uncertainty in the F vs Fe relation in Galactic normal stars should not affect the comparison of compositions of EHe, RCB and HdC stars with theoretical evolutionary scenarios; the F overabundance, in particular, dwarfs the current uncertainty.

TABLE 4.5: Elemental abundances of hot EHes.

Star name	$\log\epsilon(X)$							Ref
	C	N	O	Ne	F	Fe	Zr	
LS IV+6° 2	9.4	8.3	8.2	8.7	6.5	7.1	⋯	P11[1]
V652 Her	7.0	8.7	7.6	8.1	$\leq$ 5.6	7.1	⋯	P17[2]
V2205 Oph	9.1	7.8	8.0	8.2	7.0	6.6	⋯	P11[1]
DY Cen	9.6	7.8	9.0	8.0	6.9	6.0	⋯	P14[3]
HD 144941	6.9	6.4	7.1	7.2	$\leq$ 5.6	$\leq$ 6.6	⋯	P17[2]
LSE 78	9.4	8.3	9.4	8.7	7.4	6.8	3.5	P11[1]; P06a[4]
BD +10° 2179	9.3	8.1	7.9	7.9	6.4	6.2	$\leq$ 2.6	P11[1]; P06a[4]
V1920 Cyg	9.6	8.6	9.9	8.5	7.5	6.8	3.7	P11[1]; P06a[4]
HD 124448	9.1	8.7	8.3	7.7	$\leq$ 6.0	7.2	2.7	P11[1]; P06a[4]
PV Tel	9.2	8.6	8.8	7.6	$\leq$ 6.5	7.0	3.1	P11[1]; P06a[4]

[1] (Pandey & Lambert 2011)

[2] (Pandey & Lambert 2017)

[3] (Pandey et al. 2014)

[4] (Pandey et al. 2006)

4.4.2 Fluorine and other elements

In searching for an explanation for the hot EHes, the cool EHes and the RCBs, it is helpful to identify relationships, if any, between the abundances of key elements. No modern analysis for elemental abundances is available for the HdC stars whose spectra are dominated by molecular bands. Consideration of the elemental abundances for RCB stars must recognize that the available analyses of Asplund et al. (2000) identified 'the carbon problem'. Opacity in the atmosphere of a RCB star appears to be dominated by continuous absorption from excited levels of the neutral carbon atom. Since the many absorption lines of the neutral carbon atom also arise from excited levels, the predicted strength of weak C I lines is almost independent of the principal atmospheric parameters, that is effective temperature, surface gravity and the C/He ratio: however, the predicted equivalent widths of weak C I lines is a factor of 0.6 dex stronger than observed. This discrepancy defines the carbon problem, e.g., model atmospheres computed for a C abundance of 9.5 (equivalent to a C/He ratio of 1%) return a C abundance of 8.9 from weak C I lines, The carbon problem's implications for abundances and abundance ratios are discussed but not resolved in an extensive investigation of possible solutions by Asplund et al. (2000). Although some proposed resolutions of the carbon problem should have minimal effect on elemental abundances and particularly on abundance ratios, abundances for RCB stars should be used with reservation in effecting comparisons with compositions of EHe stars. EHe stars are not subject to a carbon problem. (Abundances for RCBs are used in Figure 4.15 where it is clear that the F and Fe abundances of EHe and RCB stars provide overlapping distributions; the Fe and F abundances for RCB stars are not both overestimated by 0.6 dex.)

The likely relationship between F abundances and abundances of C, N, O and Ne in EHes are shown in Figure 4.16. Abundances for the RCB stars generally confirm results for the EHes. In the case of C, the spectroscopic C abundances (primarily from Asplund et al. (2000)) are systematically 0.6 dex in the mean lower than for the EHes because of the carbon problem. For N, the N abundances from Asplund et al. (2000) and Hema et al. (2017), and the F abundances from Pandey et al. (2008) and Hema et al. (2017) for the RCBs, overlap well with the abundance spread provided by the EHes. For the EHes, the O-F relation may suggest a positive correlation with the RCB stars possibly superimposed on this correlation

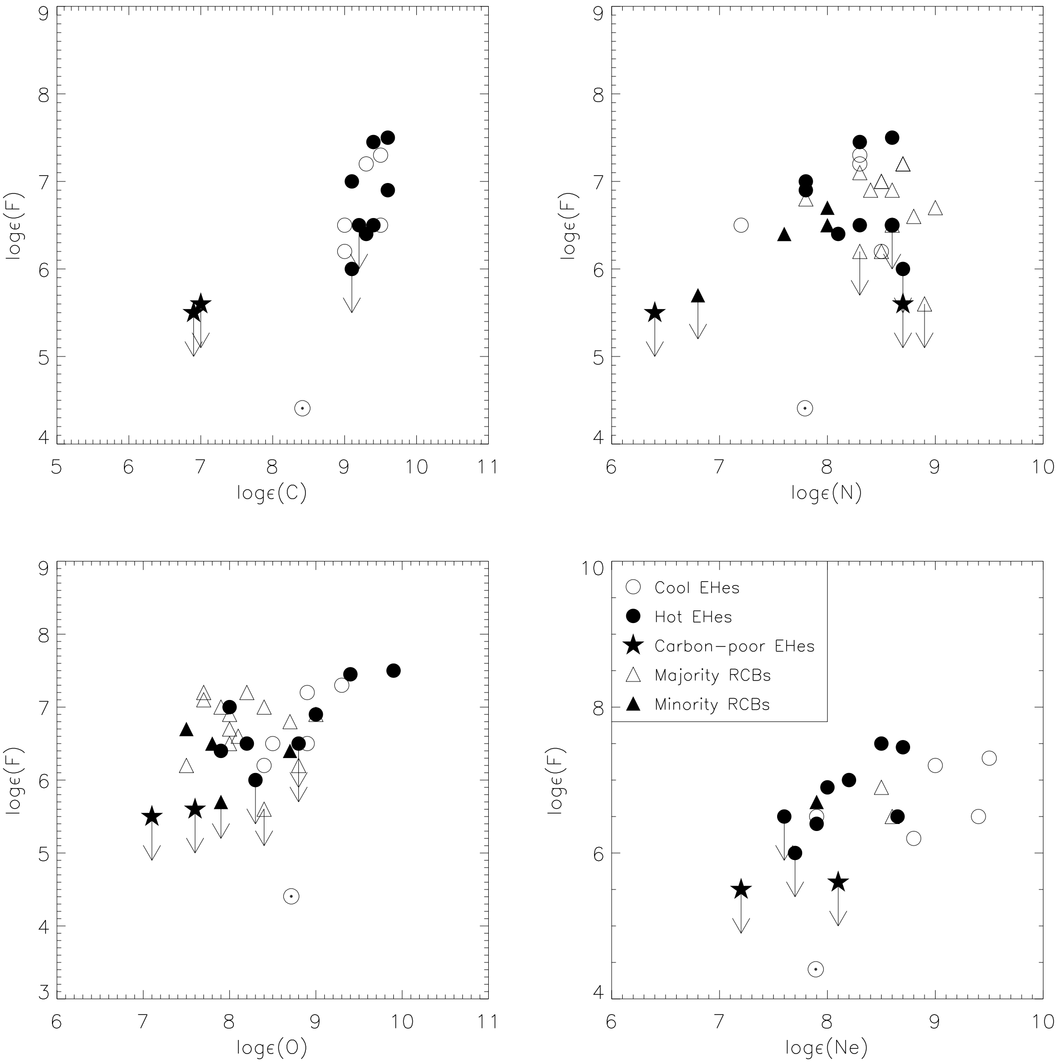

FIGURE 4.16: Observed logϵ(F) versus logϵ(X) for EHes and RCBs from where X = C, N ,O and Ne respectively. The encircled dot symbol represents the sun.

but lacking stars with the extreme O (> 9.1) abundances. Neon abundances are available from LTE analysis of Ne I lines for four RCBs - Y Mus and V3795 Sgr reported by Asplund et al. (2000); V532 Oph and ASAS−RCB−8 by Hema et al. (2017)- but the F abundance has been reported only for three : V3795 Sgr (Pandey et al. 2008), and V532 Oph and ASAS−RCB−8 (Hema et al. 2017). The minority RCB V3795 Sgr with the reported Ne abundance falls amongst the (Ne,F) abundances for hot EHes but an anticipated non-LTE reduction of about 0.7 dex to the Ne abundance would suggest V3795 Sgr is Ne-poor for its F abundance.

Whereas for the two majority RCBs V532 Oph and ASAS−RCB−8, the non-LTE reduction of 0.7 dex, directly places them in (Ne,F) distribution of hot EHes. LTE neon abundances from Ne I lines are available for five cool EHes (Pandey et al. 2001; Pandey, & Reddy 2006) and are compared with fluorine in Figure 4.16. Except for the cool EHe FQ Aqr, the neon abundances w.r.t fluorine for the cool EHes appear systematically higher than (Ne,F) abundances traced by the hot EHes. Clearly, the anticipated non-LTE correction of 0.7 dex will place them with the hot EHes. Also the same non-LTE correction on FQ Aqr would suggest that it is Ne-poor for its F-abundance just like the minority RCB V3795 Sgr.

Independently of the F abundances, relations between the N-Ne-Fe abundances provide clues to the stars' nucleosynthetic history (Figure 4.17). H-burning by the CN-cycle increases the N abundance at the expense of C and the ON-cycle provides additional N at the expense of O. In predicting the N abundance from CNO-cycling, initial C and N abundances are assumed to follow the relation [C/Fe] = [N/Fe] = 0. Initial O abundances are taken from Ryde & Lambert's(2004) [α/Fe] vs [Fe/H] relation for disk stars with O treated as a typical α-element. Nitrogen is supposed here to be the dominant product of CNO-cycling.

Nitrogen abundances as a function of Fe abundances are shown in Figure 4.17 for the cool and hot EHes against three possible relations: (i) the initial N vs Fe relation, (ii) the N abundance vs Fe relation expected if the N abundances arises from the sum of the initial C and N abundances, (iii) the N abundances resulting from the sum of the initial C, N and O abundances. With the clear exception of the C-poor hot EHe HD 144941, the N and Fe abundances are distributed along line (iii) indicating that N is a product of severe CNO-cycling in a H-rich region. Two hot EHe stars appear closer to the CN-cycling than to the CNO-cycling prediction. With the single exception of the C-poor HD 144941, the atmosphere of a hot EHe star appears severely contaminated with material exposed to CNO-cycling or possibly in two stars to CN-cycling.

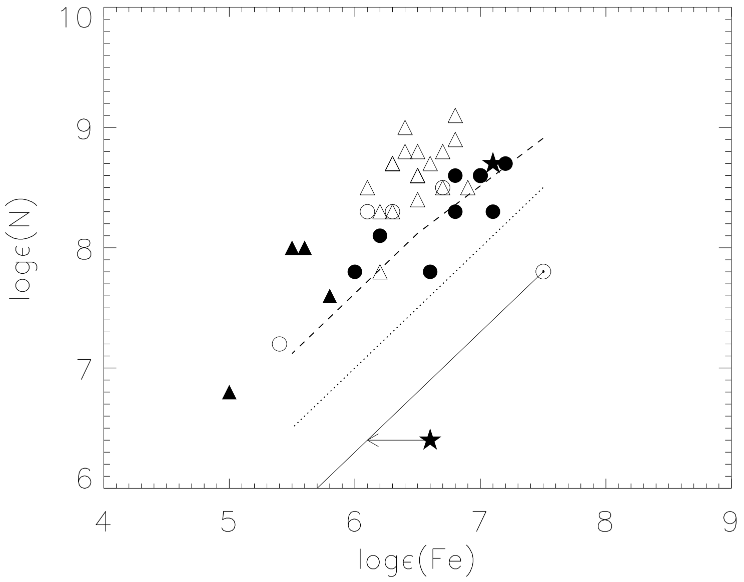

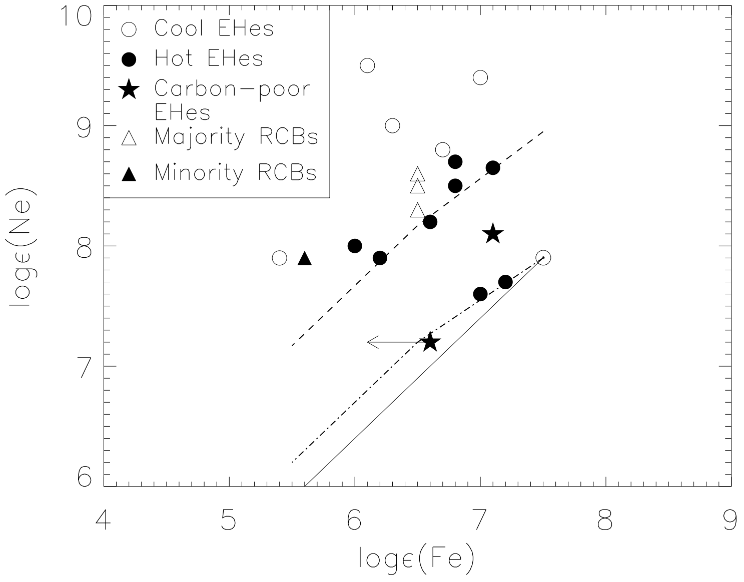

FIGURE 4.17: Observed logϵ(N) and logϵ(Ne) versus logϵ(Fe) for EHes and RCBs. The encircled dot symbol in each plot corresponds to solar value with the solid line giving the locus of solar ratio N/Fe ad Ne/Fe respectively . The dashed line in the plot of logϵ(N) vs logϵ(Fe) is the predicted nitrogen after full conversion of initial C, N and O to nitrogen in CNO cycle where initial O is determined from the relation of [α/Fe] vs [Fe/H] for normal disk and halo stars given by Ryde & Lambert (2004). The dotted line in the same plot is the predicted nitrogen due to conversion of inital C and N to nitrogen in the CN cycle. In the plot of logϵ(Ne) vs logϵ(Fe) the dot-dashed line gives the locus of initial neon values taken from the relation of [α/Fe] vs [Fe/H] for normal disk and halo stars (Ryde & Lambert 2004). In the same figure the dashed line is the locus giving of sum of initial C, N,O and Ne.

LTE nitrogen abundances for cool EHes (Pandey et al. 2001; Pandey, & Reddy 2006) obtained from both N I and N II lines track the N vs Fe trend defined by the majority of the hot EHes from N II lines corrected for non-LTE effects. Nitrogen abundances for RCB stars (Asplund et al. 2000; Hema et al. 2017) from N I lines but not corrected for non-LTE effects provide N abundances higher than those in the cool and hot EHe stars. This offset arises partially from the lack of a correction for non-LTE effects for the RCB stars and mainly be a symptom related to the carbon problem. Correction for non-LTE effects may lower the RCBs N abundances. In summary, the majority of the H-deficient stars in the RCB-EHe sequence have a N abundance indicative of severe CNO-cyling with the N abundance equalling the initial sum of the C, N and O abundances for a star's Fe abundance.

Neon is severely overabundant in EHes: Figure 4.17 (bottom panel) shows the Ne abundances for the hot EHes (Pandey & Lambert 2011; Pandey et al. 2014; Pandey & Lambert 2017) where results come from Ne I lines in all stars and Ne II lines in the few hottest stars. The abundance analysis included non-LTE effects which were substantial for Ne I lines but small for Ne II lines. When lines from the neutral atom and the singly-charged ion were both available, the Ne abundance estimates after non-LTE corrections were in good agreement: see Table 2 of Pandey & Lambert (2011).

As discussed earlier neon abundances from Ne I lines are available for five cool EHe (Pandey et al. 2001; Pandey, & Reddy 2006) and four RCBs (Asplund et al. 2000; Hema et al. 2017). Ne abundances for the cool EHes are clearly systematically higher than for the hot EHes, for example, LS IV -14^o 109 has a Ne abundance of 9.4 for a Fe abundance of 6.9 (Figure 4.17). Such a systematic offset from abundances for the hot EHes is likely due to neglect of the non-LTE effects on the Ne I lines. For the RCBs, Ne with its LTE abundance from Ne I lines, falls in Figure 4.17 slightly above the upper boundary of the points from the hot EHes. Application of the non-LTE corrections should place the RCBs and cool

EHes with the hot EHes. Then, a majority of hot and cool EHes and the RCBs have a Ne abundance corresponding closely to the sum of the initial C + N + O + Ne abundances.

The upper bound for the Ne vs Fe relation is here set by the condition that the Ne abundance is the sum of the initial C + N + O + Ne abundances which differs only slightly from the C + N + O sum used in the N vs Fe panel. Initial Ne abundances are again taken from Ryde & Lambert's (2004) [α/Fe] vs [Fe/H] relation for disk and halo stars. Identification of Ne abundances with this sum implies that material has been exposed to temperatures beyond those generally required for H-burning and the product ^{14}N has been processed by successive α-captures to ^{22}Ne seemingly with near 100% efficiency. The majority of stars in the (Ne,Fe) panel fall along the (C+N+O+Ne) limit. Among the hot EHes, HD 124448 and PV Tel and possibly also the C-poor and Fe-poor HD 144941 display a Ne abundance consistent with the star's initial abundance. HD 124448 and PV Tel have N abundances indicating conversion of initial C + N + O to N by H-burning but both appear to have avoided production of Ne by α-captures. For V652 Her, the other C-poor hot EHe, the lower Ne abundance implies either less than complete burning of the ^{14}N from CNO-cycling to ^{22}Ne and/or partial destruction of the ^{22}Ne by α-captures. Note that, only for four stars, two hot EHes: HD 124448 and PV Tel, and two C-poor hot EHes: V652 Her and HD 144941 where oberved Ne is significantly lower than the initial C + N + O + Ne limit, F II detections are absent and hence, only the upper limits to the fluorine abundance are placed.

With the single exception of HD 144941, the C-poor EHe, the N abundances of the EHe and RCB stars suggest an atmosphere dominated by gas seriously exposed to H-burning such that the initial C, N and O expected from the Fe abundance has been converted to N through the CNO-cycles. The measured Ne abundances of the majority of the hot EHes and the inferred (that is observed non-LTE corrected) Ne abundances for the cool EHes and RCBs indicate that the Ne as ^{22}Ne was most likely produced with near 100% efficiency by α-captures

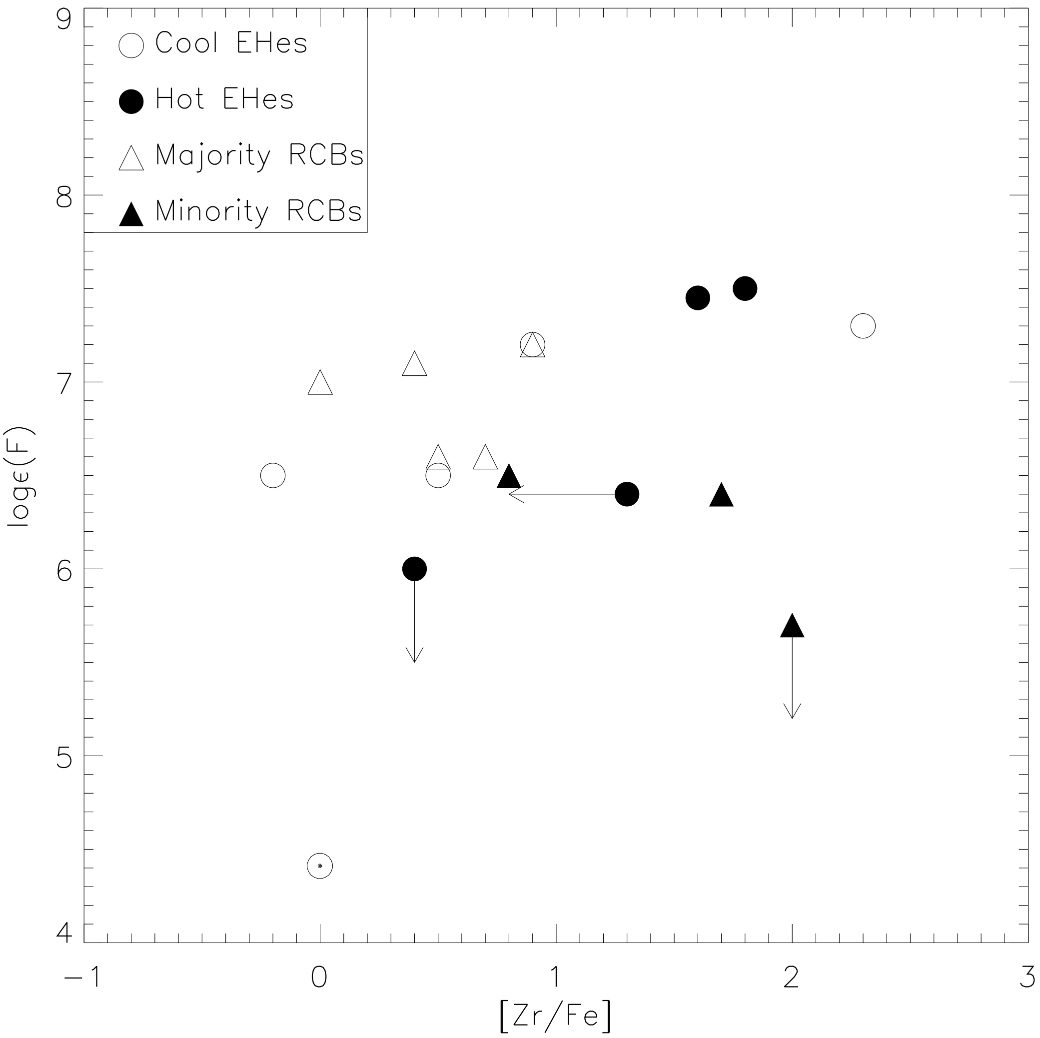

FIGURE 4.18: Observed logϵ(F) with [Zr/Fe] for EHes and RCBs. The encircled dot symbol represents the sun.

from the N by α-captures in gas previously exposed heavily to H-burning. These episodes of H-burning and (partial) He-burning can not have occurred in the same gas: Ne synthesis destroys the N and, in addition, all Ne-rich stars have abundant O. This juxtaposition of abundant N and Ne may be a pointer to distinct regions of nucleosynthesis and, perhaps, to a previous history as a binary system.

Heavy elements offer another signature of nucleosynthesis, namely the *s*-process. Asplund et al. (2000) noted the overabundance of *s*-process elements in some RCB stars. Overabundances of Zr are found for some hot EHes but in so few stars that a dependence of F on the *s*-process can not be determined (Table 4.5). To the hot EHe sample, we add RCB Zr abundances from Asplund et al. (2000) and Hema et al. (2017). Zr for a sample of cool and hot EHes are from Pandey et al. (2006)'s analysis of *HST* ultraviolet spectra and Zr for other cool EHes are from Pandey et al. (2001) and Pandey, & Reddy (2006). The full sample with both F and Zr abundances are shown in Figure 4.18. Severe *s*-process enrichment is certainly present among these H-deficient stars: [Zr/Fe] can exceed +2 but there are also stars lacking in detectable enrichment (i.e., [Zr/Fe] = 0). There is no obvious correlation between the F abundance and [Zr/Fe].

4.5 Double white dwarf mergers and the fluorine abundance

Until recently, two scenarios were in competition to explain the sequence EHe – RCB – HdC: the double-degenerate (DD) and the final-flash (FF) model.

In the FF model (see Chapter-1 Section-1.4.1) , a late or final He-shell flash occurs in a post-AGB star, a star on the white dwarf cooling track, and converts the star to a H-poor cool luminous star (i.e., a HdC or RCB star) which then evolves back at about constant luminosity (i.e., as a EHe star) to the white dwarf cooling track (Iben et al. 1983; Herwig 2001). Nucleosynthesis occuring during and following the He-shell flash shows that a H-poor supergiant may result with features of the composition characteristic of EHe, RCB and HdC stars but it has proven difficult to account for the key features namely, their low $^{16}O/^{18}O$ ratios and their remarkable F overabundances (Clayton et al. 2007; Pandey 2006; Pandey et al. 2008; Hema et al. 2017) (see Chapter-1 Section-1.4.1 for further details) . The FF model may yet be shown to account for other kinds of H-poor stars (Pandey & Lambert 2011) such as V4334 Sgr (Sakurai's object) (Pandey et al. 2008).

In the DD scenario (see Chapter-1 Section-1.4.2) , two white dwarfs merge. In the more favored version of the DD scenario, a He white dwarf is consumed by a more massive C-O white dwarf. In the less favoured version, two He white dwarfs merge. Neither version can account for the exceptional ^{18}O abundances in HdC and RCBs and/or the extraordinary F abundances in RCBs and EHes without episodes of nucleosynthesis accompanying the immediate phase of the merger and/or the post-merger phase. Clearly, the final compositions of the resulting single H-deficient stars are likely to depend on the type of the merger CO+He or He+He and on details of the stars (masses, compositions, etc.) comprising the close white dwarf binary which by loss of gravitational energy merges. A merger results in a matter of minutes in a complex system comprising the core of the more massive white dwarf (i.e., the C-O white dwarf in the C-O+He system) surrounded by a very hot corona (wonderfully dubbed 'the shell of fire') inside a rapidly rotating disk. The disrupted less massive white dwarf is the principal contributor to the corona which may also receive mass from the more massive white dwarf. The less massive white dwarf is the principal contributor to the disk from which He-rich material is accreted by the central star on a slow time scale, say 10^{-4} -10^{-5} yr. After the central star has accreted sufficient material, He-shell burning commences and the star's envelope expands to become a cool supergiant, that is a RCB or a HdC supergiant. The supergiant's surface composition is determined by the compositions of the merging white dwarfs, the nucleosynthesis occurring in the initial brief coronal phase of the merger and in the supergiant's, He-shell burning phase and by the (complex) physics of the whole merger process. Simulations of the merger and post-merger phases have yet to reach the finality to which the commendation '*ab initio*' may be attached appropriately.

Our focus here is on published calculations of the DD scenario and their ability to match the observed F abundances of these H-deficient stars and, in general, their overall compositions including the remarkably low ^{16}O/^{18}O ratios of HdC and RCB stars (Clayton et al. 2007), whose discovery has stimulated much of the theoretical work on these H-deficient stars. For detailed descriptions of the

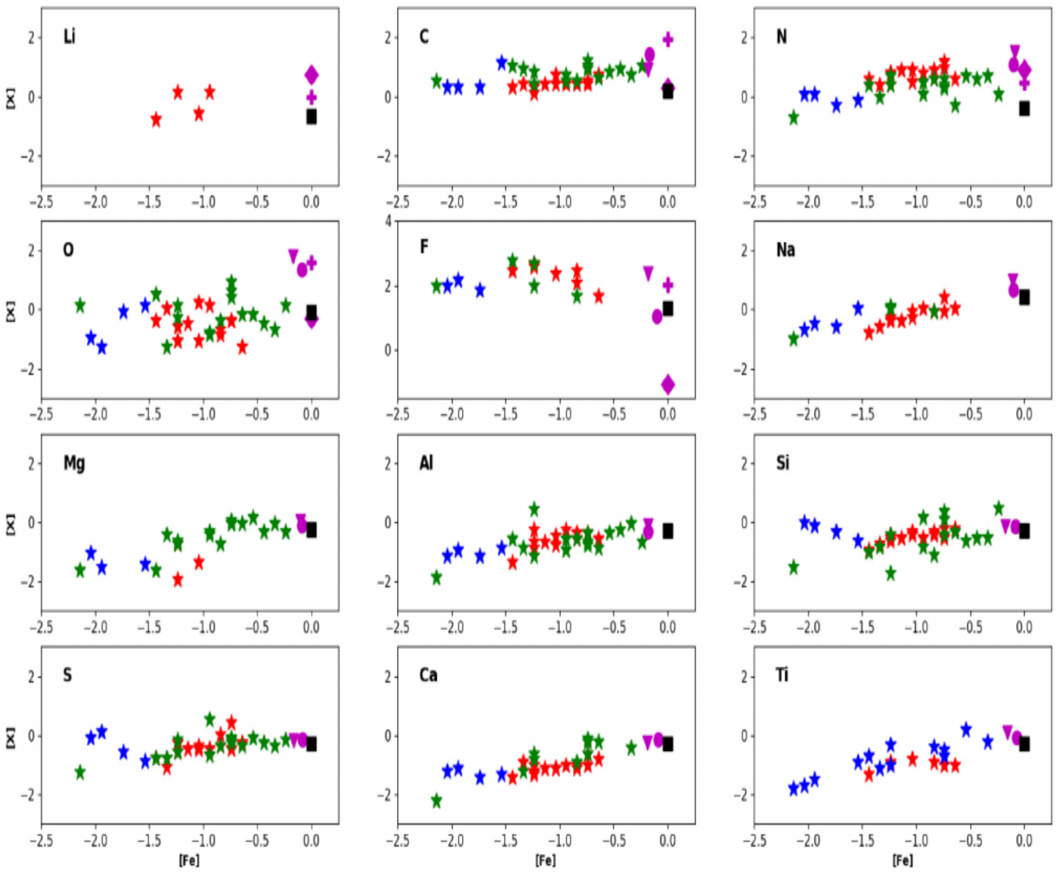

FIGURE 4.19: Comparison of the observed surface abundances of RCBs and EHes obtained from Jeffery et al. (2011), with the result of Lauer et al.'s MESA model A1. [X] represents logarithmic number abundances of an element X relative to solar. The symbols represent majority RCB (red stars), minority RCB (blue stars), and EHe (green stars). The black square in each panel is the abundance from model A1. The magenta symbols correspond to results from other sources in the literature: filled triangle and circle symbols correspond to results presented by Menon et al. (2013), plus symbols to results by Longland et al. (2011) and diamond symbols to results by Zhang et al. (2014). The figure is taken from Lauer et al. (2019).

various theoretical calculations one should consult the original papers. Our principal comparisons are with predictions for CO+He white dwarf mergers provided by Lauer et al. (2019) and by Menon et al. (2013); Menon et al. (2019) and **Crawford et al. (2020)**. Lauer et al. (2019) provide commentary on other calculations of CO+He white dwarf mergers including Longland et al. (2011), Zhang et al. (2014) and Menon et al. (2013); Menon et al. (2019).

Lauer et al. (2019) report on modeling of CO+He white dwarf mergers for stars initially of solar composition, i.e., [Fe] = 0. Most simulations consider a $0.55M_{\odot}$ CO white dwarf leading to a post-merger mass of $0.8M_{\odot}$. Predicted abundances for their principal product of a merger labelled A1 are summarized in Figure-4.19) taken from Lauer et al. (2019). Model A1 deserves a fair pass against the observations of the ^{16}O/^{18}O ratios and the F abundances of HdC, RCB and EHe stars extrapolated to [Fe] $\sim$ 0. Fluorine as synthesized in the hot corona is about a factor of three less than observed. Observed C abundances are slightly under predicted. Model A1 also underpredicts the N abundance. Neon, as ^{22}Ne , is predicted to be overabundant at the surface but quantitative estimates are not provided. For other elements Na to Ti observed and predicted abundances match quite well. Lithium production occurs in the A1 model providing a Li abundance at about the level seen in those few RCBs exhibiting Li.

Crawford et al. (2020) develops upon the models by Lauer et al. (2019) to explore the effects of initial He-shell burning temperature and metallicities on the surface abundances of RCB stars. Their merger models consist of two different metallicities – solar and sub-solar (10% of solar metallicity), with a range in initial He-shell burning temperature (referred by them as T$_{He}$), between 2.1 - 5.4 $\times$ 10^8 K. Predicted surface abundances for their sub-solar model having initial He-shell burning temperature of 3 $\times$ 10^8 K, match well in regards to observed ^{16}O/^{18}O, ^{12}C/^{13}C ratios and F abundances in RCB stars. The main caveat in their models is the prediction of the formation of ^{18}O facilitated by partial helium burning through the reaction $^{14}\mathrm{N}(\alpha,\gamma)^{18}\mathrm{F}(\beta^+,\nu)^{18}\mathrm{O}$ and enrichment of F via the reaction $^{18}\mathrm{O}(p,\gamma)^{19}\mathrm{F}$, with the protons available due to mixing of the remnant H-shell around CO-WD with the disrupted He-rich envelope during the merger event. As a matter of fact, their sub-solar metallicity models that fairly predict enhanced ^{18}O and F, fail to account for the observed enriched N abundances in the RCB atmosphere, due to N being predicted as the main seed for the formation of enhanced ^{18}O and ^{19}F. Though many of their models correctly predict neon over-abundances yet Ne is under-predicted by 1 dex in the sub-solar models that predict enhanced ^{18}O, due to the reaction– $^{14}\mathrm{N}(\alpha,\gamma)^{18}\mathrm{F}(\beta^+,\nu)^{18}\mathrm{O}(\alpha,\gamma)^{22}$Ne being the main controller in determining the abundance of this isotope. For their cooler models, the dominant Ne isotope is ^{20}Ne; however, those models fail to predict enhanced F as F enrichment occurs at higher T_{He}. They also discuss a severe issue on explaining the observed Li abundances as the choice of different metallicity in their models had lead to either under-prediction or over-prediction of Li abundances. While their solar metallicity models predict $\log\epsilon$(Li) between 0.85 and 2.64, the sub-solar models predict $\log\epsilon$(Li) between 3.95 and 6.41; whereas the observed Li abundances lie within 2.6 and 3.5! However, they do argue that the choice of metallicity should not affect the Li abundance, and it mainly depends on the abundance of ^{3}He in the merger progenitors which can produce fresh lithium by the Cameron-Fowler mechanism ($^3\mathrm{He}(\alpha,\gamma)^7\mathrm{Be}(e^-,\nu)^7$Li). Another limitation in their study, is their inability to consider the reaction $^7\mathrm{Li}(\alpha,\gamma)^{11}$B in their simulations, which destroys lithium bringing down the Li abundance, and is about 8 orders of magnitude more effective than α captures on ^{14}N.

Menon et al. in their 2013 paper considered four mergers for stars with initially [Fe]=0 and in their 2019 paper extended their study to merging stars with [Fe]=-1.4, and, thus, spanned the [Fe] range of the observed EHe and RCB stars. Predicted surface compositions for [Fe]=0 and -1.4 with regards to $^{16}\mathrm{O}/^{18}$O and F match observations quite well. The predicted F enrichment reproduces the observed F abundances. Menon et al. (2013) note that one source of F is in the He-burning shell of the post merger star where $^{13}\mathrm{C}(\alpha,n)^{16}$O serves as a neutron source and ^{14}N is both a neutron poison and a F source: $^{14}\mathrm{N}(n,p)^{14}\mathrm{C}(p,\gamma)^{15}\mathrm{N}(\alpha,\gamma)^{19}$F. Predicted C and O abundances exceed observations, an issue discussed by Menon et al. (2019). Note that the reported observed [O] abundances in Figure 5 of Menon et al. (2019) are overestimated by abount 0.7 dex. Predicted N abundances match observations quite well. In the hot corona, neutrons are released in some models and enrichment of s-process heavy elements predicted. Observed s-process enhancements are found in some EHes and RCBs, see Figure 4.18. Predictions for Zr roughly match the observed maximum [Zr/Fe] for the models which release neutrons. The range of light *s*-process enhancements predicted approximately matches the range of [Zr/Fe] shown in Figure 4.18. However, one simulation experiencing severe Zr enrichment also predicted substantial enrichment of heavy *s*-procss elements such as Ba and La, i.e., [Ba/Fe] = 4 which is not observed. Minor changes to the Na and Al abundances were predicted primarily as a result of proton captures. Explicit predictions of the surface Ne abundances were not given but appreciable synthesis of neon as ^{22}Ne occurs in these models. In all published simulations the abundant isotope of neon is ^{22}Ne not the commonly abundant ^{20}Ne isotope.[5]

Considering the complexity of the physics and the variety of initial conditions for the two white dwarfs in the CO+He merger, it seems fair to conclude that the DD scenario with CO+He white dwarf mergers as presently simulated provides an adequate account of the two principal abundance anomalies of RCB and EHe stars, namely the ^{16}O/^{18}O ratios and F abundances, and the C, N, O and Ne abundances without introducing other anomalies that are not matched by observations. It remains to examine if the alternative possibility of He+He white dwarf mergers may also account for the compositions of some RCB and EHe stars. Noting that Zhang & Jeffery (2012b) indicate that production of RCB and EHe stars via the He+He channel may be 14-70 times smaller than from the CO+He channel, H-deficient stars created by the He+He channel may be the exception among the observed population of RCB and EHe stars.

Simulations of He+He white dwarf mergers as an explanation for H-deficient stars appear to be limited to those by Zhang & Jeffery (2012a,b) who explored restricted ranges for the many parameters entering into the simulations. Zhang

---

[5] Although the isotopic wavelength shifts of Ne I and Ne II lines may be measurable with precision in the laboratory, differentiation between the two Ne isotopes in a spectrum of a EHe will not be a trivial matter. A catalog of isotopic shifts between ^{20}Ne and ^{22}Ne for Ne I lines is given by Ohayon et al. (2019) and for Ne II lines by Öberg (2007). The maximum shift for our selection of lines for Ne I is about 1.5 km s^{-1} and for Ne II is about 2.5 km s^{-1}. With a careful selection of comparison lines around the Ne I & Ne II lines it may be possible to show that the stellar Ne lines share the radial velocity of the star provided that the ^{22}Ne wavelengths are adopted. However, the stellar lines for have an FWHM of about 10-30 km s^{-1} and line widths and velocities may differ according to their depth of formation in the stellar atmosphere.

& Jeffery (2012b) considered the merger of two $0.4M_\odot$ He white dwarfs for four metallicities from Z = 0.02 to Z = 0.0001. Predicted surface abundances of the resulting RCB and EHe stars were "in partial agreement" with the observed abundances. In particular, the models showed 'a strong overabundance of F [relative to the initial F abundance]' but not enough to fully agree with the observational data. The disagreement was a factor of 100 at [Fe] = −2 decreasing to a factor of about 20 at [Fe] = −1. In these mergers, the F is synthesized by $^{14}\mathrm{N}(\alpha,\gamma)^{18}\mathrm{F}(p,\alpha)^{15}\mathrm{O}(\alpha,\gamma)^{19}\mathrm{Ne}(\beta^+)^{19}\mathrm{F}$. Enrichment of ^{18}O may be underpredicted too. Minor disagreements between prediction and observation are found for C, N, O and Ne. The RCBs and EHes are predicted to be C-rich not C-poor at all Z. Lithium, which is observed in a few RCBs, is not predicted to be present in the merged star.

In Zhang & Jeffery (2012a), four models of equal-mass pairs of He white dwarfs were followed: total masses considered were 0.5, 0.6, 0.7 and $0.8M_\odot$ for initial compositions Z = 0.02 and 0.001. An aim of the calculations was to examine the effect of 'slow' mergers (the accreted star forms a disk around the accreting star from which gas is accreted at 10^{-5} $M_\odot$ yr^{-1}), 'fast' mergers corresponding to an accretion rate of 10^{-4} $M_\odot$ yr^{-1} for the remaining white dwarf and 'composite' mergers in which about 50 per cent of the donor star's mass is accreted rapidly and the remainder forms a disk from which gas is accreted at the 'slow' rate. Predicted compositions for the merged 0.5 - 0.8 $M\odot$ stars were given for just ^{12}C, ^{14}N, ^{18}O and ^{22}Ne and comparisons with observed compositions were made with helium-rich hot subdwarfs and not RCB and EHe stars. While F was not reported for these simulations, their relevance to our determinations of F abundances may be the conclusion that composite mergers from these equal mass white dwarf pairs show an appreciable C underabundance for combined masses below about $0.6M_\odot$ with little change of N across the mass range of 0.5-$0.8M_\odot$ and thus the N/C ratio is predicted to increase as the mass decreases below about $0.65M_\odot$. This prediction, as Zhang & Jeffery (2012a) note, likely accounts for the two classes of He-sdO stars: the N-rich with N/C >> 20 and the C-rich with N/C $\leq$ 0.1. The same prediction may provide the latitude to account for the C-poor V652 Her and HD 144941 with their different N/C ratios but their masses would have to be between 0.6 and $0.7M_\odot$. One might also put the RCB XX Cam in this narrow range.

4.6 Concluding remarks

With observed determinations of the compositions of the H-deficient stars – HdC, RCB and EHe – and theoretical simulations of the merger of a CO white dwarf with a He white dwarf – the DD scenario – the many decade mystery surrounding compositions of these stars has been resolved. In particular, the large F overabundances for hot EHe stars derived in this work and compatible with F abundances obtained previously for cool EHe and RCB stars are thanks to detailed simulations, e.g., Menon et al. (2013); Menon et al. (2019); Lauer et al. (2019), of the DD scenario known to be quantitatively expected. Indeed, the simulations account well for the observed chemical compositions of the HdC, RCB and EHe sequence including the remarkably low $^{16}O/^{18}O$ ratio (Clayton et al. 2007) which with the F overabundances are *the* outstanding abundance anomalies of these H-deficient stars.

In the future, observers will be challenged to refine the determinations of chemical composition by not only obtaining more accurate analyses for elements previously studied but by searching for the small abundance changes in the elements Na to Zn and in the *s*-process elements predicted by the available quantitative studies of white dwarf mergers. A major lacuna in the abundance analyses concerns the non-LTE formation of the F I and F II lines but this gap in quantitative knowledge does not affect the conclusion the F overabundance in these H-deficient stars is enormous and can be only slightly affected by inclusion of non-LTE effects.

On the theoretical side, exploration of the DD scenario should continue. Predicted abundances of light elements should be tested more thoroughly than hitherto against observed abundance ratios. For example, the puzzles represented in Figure 4.17 deserve close scrutiny: How can N and Ne both have the abundance implied by total conversion of initial C, N and O? Perhaps, the range of chemical compositions of HdC, RCB and EHe stars may be used to set constraints on the boundary conditions for participants in a merger and the physical conditions during and following the merger with ultimate hope of achieving *ab initio* predictions for the family of H-deficient stars.

Chapter 5

Quantitative analysis of the Extreme Helium Star V2205 Oph[1]

An overview

In this work, we report LTE abundance analysis on the optical high-resolution spectrum of the extreme helium star, V2205 Oph obtained using HESP. Through quantitative fine analysis we determine the atmospheric parameters and chemical abundances. Atmospheric parameters are derived from a grid of LTE model atmospheres by using ionization balance of ion pairs such as CII/CIII and NII/NIII, and using spectroscopic indicators like He I line profiles. The LTE stellar parameters derived in this work are: $\mathrm{T}_{eff} = 23900 \pm 900$ K , $\log g = 2.65 \pm 0.1$ (cgs) and $\xi = 28 \pm 2$ kms^{-1}. Most of the chemical abundances determined for 12 elements from H to Fe agree with the previous studies. By exploring the discrepancy of abundances determined from ionic pair of same species we comment that ions of Si and S are heavily affected by departures from LTE. Hence future studies using non-LTE abundance analysis of this star is recommended.

---

[1] The contents of this chapter is based on the publication (Bhowmick et al. 2021)

5.1 Introduction

One of the intriguing factors of Extreme Helium Stars is their distinctive chemical composition. Hydrogen-deficient by nature, the atmosphere of EHes are riddled with unique chemical peculiarities that set them apart from all other stellar objects. One of them is the overabundance of F common to both cool and hot EHes which we explore in Chapter 4. This unique chemical composition plagued with detection of so few EHes (~ 21) gave rise to different stellar evolution theories for their formation and evolution. Two theories explaining their formation and evolution stood the test of time – the DD merger scenario and FF scenario. Currently, with the improvement of a detailed analysis of EHes, the DD-merger scenario is most favoured for the formation of EHes. For detail discussion about the composition of EHes and the likely formation scenarios, please see Chapter-1 Section-1.2.2, and Section- 1.4. All these speculations and inferences are a result from one thing - *"the atmospheric parameters and the observed surface composition of an EHe"*. Continuous improvement of rigorous spectroscopic analysis performed by untiring minds through decades, lead us to the present understanding of these enigmatic objects. However, the exploration is not over yet, as with the continuous improvement of spectroscopic data and analysis tools we get to discover more and more concealed characteristics of these exotic objects. Almost 70 years after the discovery of first EHe in 1942, Pandey (2006) discovered that F relative to Fe is overabundant by about 800-8000 times in the atmosphere of cool EHes. Fourteen years later, we discovered that this overabundance extends even in the regime of hot EHes (Bhowmick et al. 2020)(see Chapter 4). Hence more and more improved spectroscopic analysis plays a very vital role in developing a proper understanding of the origin and evolution of these enigmatic objects.

In this work, we aim to carry out a quantitative spectroscopic analysis of the Extreme Helium Star, V2205 Oph under the assumption of Local Thermodynamic Equilibrium (LTE). Previous studies (see Jeffery & Heber (1992) and references therein) show that V2205 Oph is characterised by light and radial velocity variations. It is also one of the few EHes to show line profile variability (lpv) in their spectra, suggesting non-radial pulsations. The spectrum of V2205 Oph is characterised by both variable absorption and emission lines. Jeffery & Heber (1992) discuss an extensive library of optical and ultraviolet spectra. Their derived surface composition suggests a hydrogen-poor atmosphere having enhanced carbon, phosphorus and argon and possible depletion of oxygen with a severe enrichment of neon, silicon and sulphur ([Ne/Fe] > 2 and [Si/Fe], [S/Fe] > 1). With a better quality of data and better model atmosphere, Pandey & Lambert (2011) did a comparative LTE and non-LTE study of this star. However, their abundance determinations were limited to 5 elements – H, C, N, O and Ne. Their LTE analysis led to the atmospheric parameters: $T_{eff} = 24800$ K and $\log g = 2.85$ while non-LTE analysis gave, $T_{eff} = 24300 \pm 600$ K and $\log g = 2.65 \pm 0.2$. The LTE chemical abundances of the five elements reported by them are consistent within a range of 0.3 dex when compared to Jeffery & Heber's determinations. However, the non-LTE corrections vastly improve on the Ne abundance bringing it down by 0.7 dex. Similar Non-LTE corrections on Si and S may potentially bring down the reported Si and S abundances (Jeffery & Heber 1992). If the level of enrichment of Si and S is found to be consistent with Jeffery & Heber's determinations, then V2205 Oph will be similar to the minority RCB star group having high [Si/Fe] and [S/Fe]. Hence a thorough abundance analysis is necessary to investigate this pressing issue. With the availability of high-quality data obtained from HESP, the main aim of this current work is to improve the previous determinations of atmospheric parameters and chemical abundances of V2205 Oph under the assumption of LTE. This LTE analysis is a preliminary step in the long goal of a complete Non-LTE abundance determinations of V2205 Oph to determine its evolutionary status.

This chapter is organised as follows:- Section-5.2 discusses the observation. Section-5.3 addresses line identification in the spectrum of V2205 Oph. Section-5.4 describes quantitative fine analysis leading to the determination of atmospheric parameters and chemical composition and discusses the results in light of the previous studies. Section-5.5 concludes the chapter with few final remarks.

5.2 Observation

High-resolution optical *é*chelle spectra of V2205 Oph were obtained on the nights of 2017: June 4 and 2018: May 09, May 10, May 20 using the Hanle Echelle Spectrograph (HESP) (see Chapter-2, Section-2.2.1.2 for details) mounted on the 2-m Himalayan Chandra Telescope (HCT) at the Indian Astronomical Observatory (IAO) in Hanle, Ladakh, India. The observational details of V2205 Oph are mentioned in Table-4.1 of Chapter-4. The observing procedure and processing of data are the same as mentioned in Chapter-2, Section-2.3.

The spectrum of V2205 Oph is characterised by variable absorption line profiles and prominent emission features. Hence care is taken to ensure that only those frames are considered for analysis which has symmetric absorption line profiles with minimum core emission. The chosen frames were combined to improve the signal-to-noise ratio. It should be noted that, before combining the different frames, the observed spectra are corrected to rest wavelengths using well known stellar lines. The average SNR at 4500 Å of the combined spectrum, is $\sim$ 220. Our spectrum provides a useful wavelength coverage of 3800-10000 Å in the optical, at a resolution of 29000, determined from the FWHM of telluric lines at 6925 Å . Our observed optical data is a significant improvement over the quality of data used by Jeffery & Heber (1992) (having a discontinuous wavelength coverage of 3900-4800 Å, 4000-4900 Å and 5800-6800 Å) and, Pandey & Lambert (2011) (having a wavelength coverage of 3800-10000 Å with spectral gaps longward of 5500 Å).

5.3 Line identification

The spectrum of V2205 Oph is mainly dominated by absorption lines (with some suggestion of emission) arising from H I, He I, C II, C III, N II, N III, O II, Ne I, Al III, Si II, Si III, Si IV, P III, S II, S III and Ar II with a small collection of weak lines from Ne II and Fe III. Emission lines are mainly from He I, C II and Si II transitions. The H-Balmer lines are also susceptible to overlying variable emission. Line identification from H to Fe, suitable for analysis, is done using the Revised Multiplet Table (RMT) of Moore (1972), Tables of spectra of H, C, N, and O (Moore 1993), the NIST Atomic Spectra Database[2] and the Kurucz database[3].

5.4 Quantitative Fine analysis

The detailed analysis involves the determination of the atmospheric parameters like effective temperature (T_{eff}), surface gravity ($\log g$) and microturbulence, (ξ) before estimating the chemical abundances of the star. The stellar parameters are determined from the absorption line spectrum.

The first step is to determine the microturbulent velocity, ξ (in kms^{-1}). It is determined by using the principle that the abundance determined from a set of lines of the same ion arising from similar excitation potential should be independent of the line's equivalent width. To reduce the temperature dependence, lines of a species arising from similar lower excitation potential (LEP) are used. While the weak lines of any species are least affected by the microturbulent velocity, the strong lines are effected the most. Hence for this exercise, lines of a species having different strengths for a particular LEP are chosen. The derived microturbulent velocity is independent of the T_{eff}, $\log g$, and C/He adopted for the model atmosphere as explored by Pandey et al. (2001).

---

[2] `https://physics.nist.gov/PhysRefData/ASD/lines_form.html`

[3] `http://kurucz.harvard.edu/`

The T_{eff} and $\log g$ are determined by employing the principle of Saha's ionization equilibrium. The ionization equilibrium states that the abundance of an element determined from lines of different stages of ionization should be the same. The imposition of ionization equilibrium for any element having more than one ionized state in the spectrum defines a locus in the $\log g$ − T_{eff} plane. Pairs of ions of a common element provide loci of very similar slope in the $\log g$ − T_{eff} plane. An indicator yielding a locus with a contrasting slope in the $\log g$ − T_{eff} plane is required to break the degeneracy presented by ionization equilibrium. The final values of T_{eff} and $\log g$ are determined from the intersecting loci in the $\log g$ − T_{eff} plane.

The main principle employed in the abundance analysis is that the chemical composition of the adopted model atmosphere must match the observed surface composition from the spectrum. This match is obtained iteratively. One of the most helpful aid in performing the abundance analysis is that the model atmospheres computed for hot EHes with C/He of 0.003%-1% and H/He of 0.0001 to 0.01 have the same atmospheric structure and hence returns the same atmospheric parameters and surface composition as noted by Pandey & Lambert (2011, 2017). This is due to the fact that neutral He is the dominant source for continuum opacity in the hot EHes (see Section-4.4).

Since V2205 Oph is an H-deficient hot EHe, the dominant source of the continuum opacity is provided by the photoionization of neutral helium as explained before. Hence lines of any detected species are sensitive to the abundance ratio of the said element to helium. Abundance of any element X is given by $\log\epsilon(X)$ which is normalized w.r.t $\log \sum \mu_i \epsilon(i) = 12.15$, where μ_X is the atomic weight of element X. Except He since all other elements are in trace amount, the logarithmic He abundance is 11.54 (see Section-4.4 for detailed explanation).

The model atmospheres used in this study are computed under the following classical assumptions: the atmospheric structure consists of horizontally homogeneous, plane-parallel layers in hydrostatic equilibrium with total energy flux (radiation plus convection) constant, under the assumption of Local Thermodynamic Equilibrium (LTE). The grid of LTE model atmospheres used in this work was calculated by Pandey & Lambert (2011) using the code TLUSTY[4]. We employ the spectrum synthesis code SYNSPEC (Hubeny et al. 1994) to generate synthetic absorption line profiles. SYNSPEC solves the radiative transfer problem for spectral lines under the specified LTE (or non-LTE) assumption and calculates the equivalent widths for a given stellar atmospheric model. It requires a given model atmosphere, a line list comprising of line information of elements that has to be calculated and guess abundance of the concerned element as an input. For a given stellar model, the guess abundance is iterated until the calculated equivalent width matches with that of observed equivalent width.

The identified lines are compiled together to create a line list consisting of individual line parameters–like the transitional probability or $\log gf$ values and lower excitation potential for the abundance analysis. The updated $\log gf$ values are mainly adopted from NIST and Kurucz's databases, supplemented by compilations of Podobedova et al. (2009); Kelleher & Podobedova (2008a,b) mainly for S, Si and Al.

5.4.1 Atmospheric parameters

For determining the microturbulent velocity ξ, lines of O II having LEP 23 eV and 25 eV were used as they show a large range of equivalent width. An LTE model atmosphere with $T_{eff} = 24800$ and $\log g = 2.85$, similar to the LTE atmospheric parameters obtained by Pandey & Lambert (2011) for this star, was adopted initially for the determination of microturbulent velocity. A microturbulent velocity, $\xi = 28 \pm 2$ kms^{-1} was obtained for these set of O II lines (see Figure-5.1)

For determining T_{eff} and $\log g$ ionization equilibrium was imposed for the set of available ion pairs such as C II/C III, N II/N III, Si II/Si III, Si III/Si IV, Si II/Si IV

---

[4] `http://tlusty.oca.eu/Tlusty2002/tlusty-frames-guides.html`

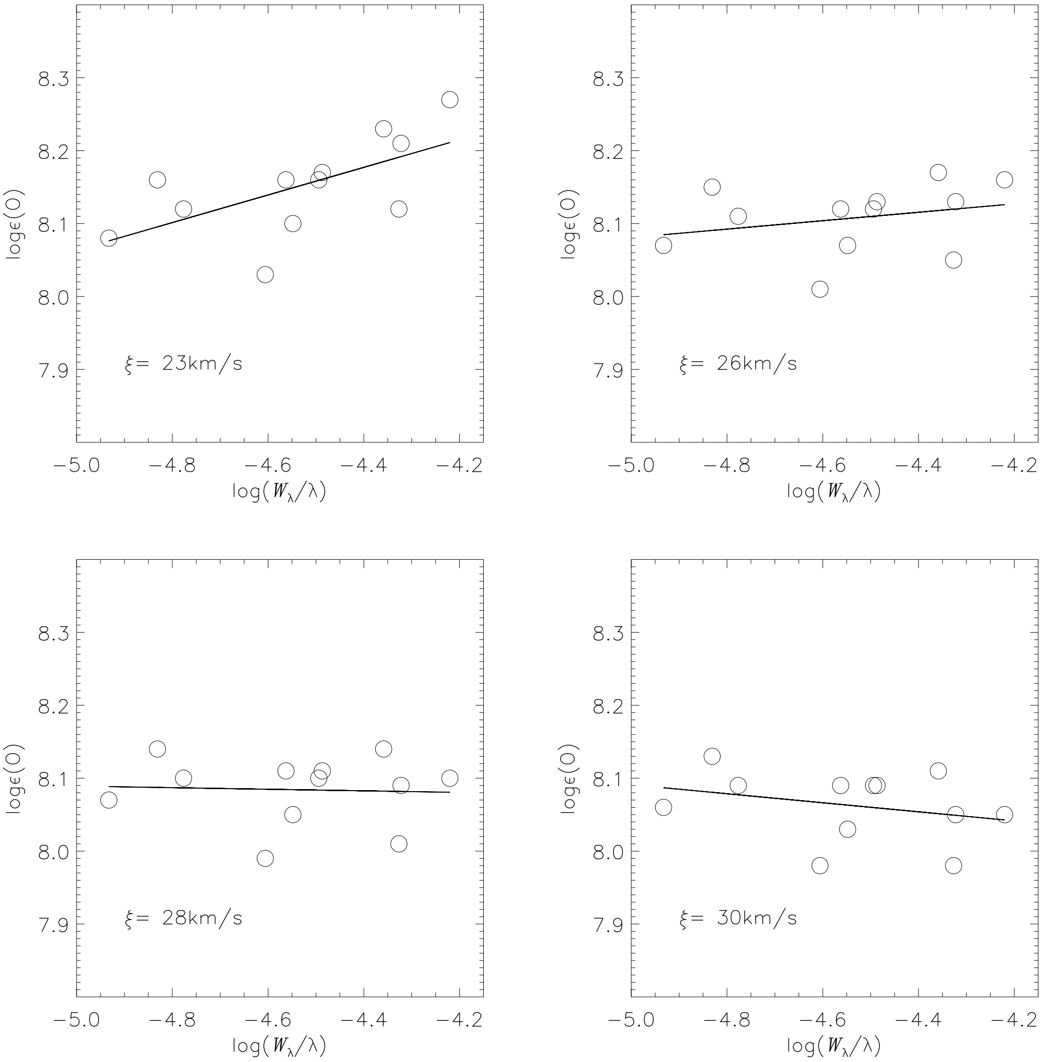

FIGURE 5.1: LTE abundances from O II lines for V2205 Oph vs their reduced equivalent widths (log W_λ/λ). A microturbulent velocity of ξ = 28 kms^{-1} is obtained from this figure.

and S II/S III. However, as observed in Figure-5.5, the loci derived from the ionization equilibrium of various species run almost parallel to each other in the log g − T$_{eff}$ plane. The degeneracy presented by the near-parallel loci of ionization equilibrium of different species presents a problem for arriving at a definite solution. A potential indicator having a locus with contrasting slope are fits to the He I lines in the hot EHes. In the hot EHes neutral helium or He I is the principal contributor to continuum opacity. Hence the He I line strengths are insensitive to T$_{eff}$. Nevertheless, their wings are sensitive to log g on account of pressure broadening due to the presence of quadratic Stark effects on strong He I lines. The locus was derived from the best fits to the Stark-broadened profiles of He I lines at 4026 Å , 4387 Å , and 4921 Å with the line broadening coefficients of He I adopted from Shamey (1969). Sample of observed He I line profiles at 4026 Å , 4387 Å , and 4921 Å are shown in Fig-5.2, 5.3, and 5.4 respectively. Each figure corresponds to predicted LTE profiles for two different temperatures 24000 K and 25000 K, each having two different sets of surface gravities. Note that the synthetic He I line profiles are convolved with the profiles due to instrumental resolution and the stellar rotation. A high rotational velocity ($v \sin i$) of 22 ± 6 km s^{-1} was obtained from the fits to the clean lines of O II after considering instrumental broadening. Note that this value is lower than the projected rotational velocity of 41 ± 3km s^{-1} reported by Jeffery & Heber (1992).

The LTE analysis is affected by many inconsistencies arising due to substantial non-LTE effects on some of the lines. These inconsistencies lead to compromises in selecting the solution for atmospheric parameters and hence in determining the elemental abundances. One of the significant issues are the fits to He I line profiles. The synthesized LTE He I line profiles fail to match the observed cores but provide good fits to the line wings. The principal reason that LTE approximation holds good for the line wings is because they are formed in the deeper layers of atmosphere which are dominated by collision and hence follow Boltzmann distribution. The line cores are formed in the outer optically thin layers which are dominated by scattering, and hence departures from LTE becomes prominent. This phenomenon is beautifully demonstrated by Pandey & Lambert (2017) in their paper on non-LTE and LTE analysis of two hot EHes– V652 Her and HD 144941, with one of the star – V652 Her, having a similar temperature like our programmed star. While their LTE He I line profiles fit the observed line wings but fail to reproduce the core, their non-LTE He I profiles provide good fits to both the core and wings. Hence our exercise to obtain the LTE atmospheric parameters by fits to the He I line wings ignoring the observed core is faithful to the published analysis.

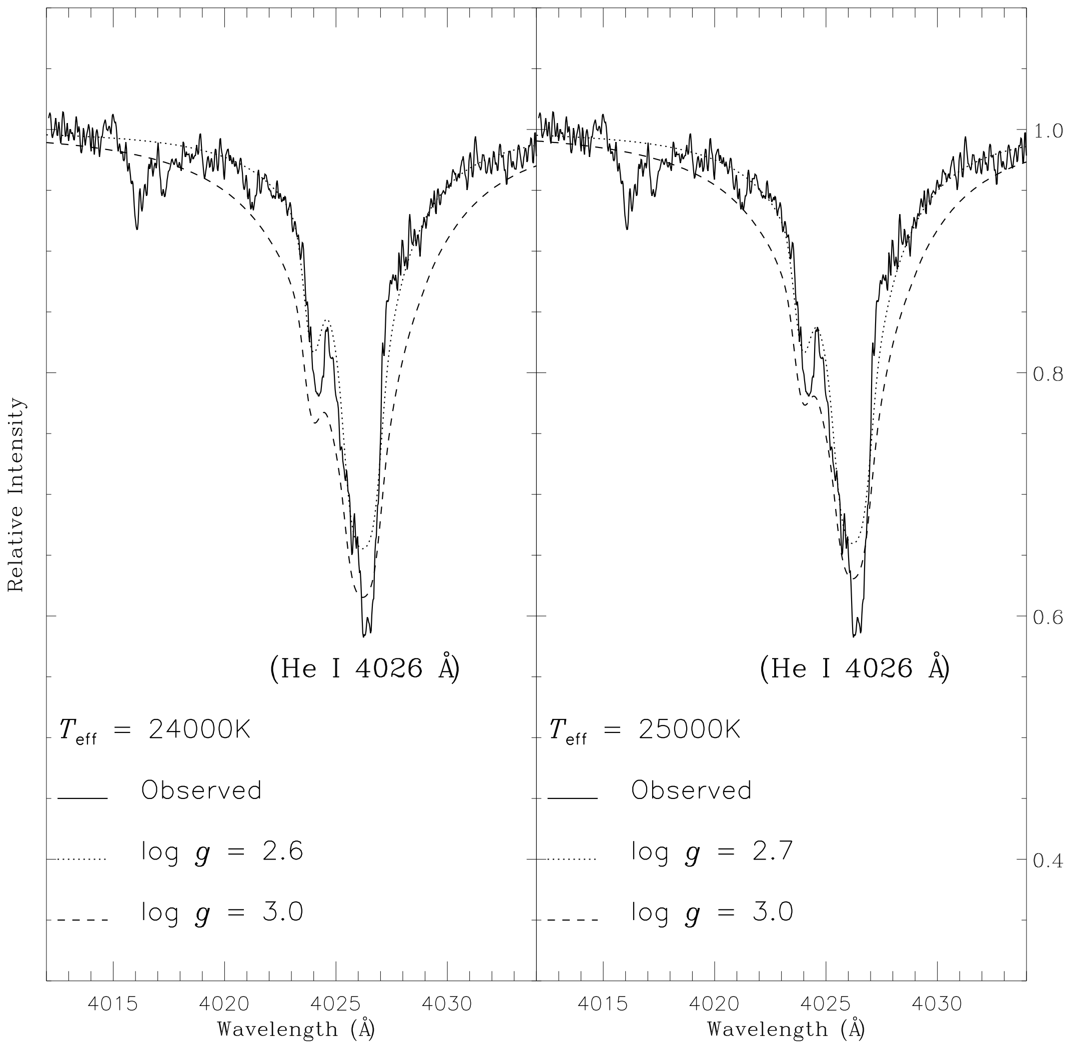

FIGURE 5.2: V2205 Oph's observed and synthesized LTE He I line profile at 4026 Å . In the left panel the LTE He I line profiles are synthesized for T_{eff} = 24000 K for two different $\log g$ values. Similarly in the right panel the LTE He I line profiles are synthesized for T_{eff} = 25000 K for two different $\log g$ – see key on both the panels.

Another issue of substantial non-LTE effects on different species can be checked from the individual loci of the ionization equilibrium of different ion pairs. It is evident from Figure-5.5, the locus set by S II/S III is considerably shifted than the loci obtained from C II/C III and N II/N III. Taking a cue from Pandey & Lambert (2017), we can safely comment, that shift is due to large non-LTE effects. Similarly, when we compare the loci of Si II/Si III, Si II/Si IV and Si III/Si IV in the

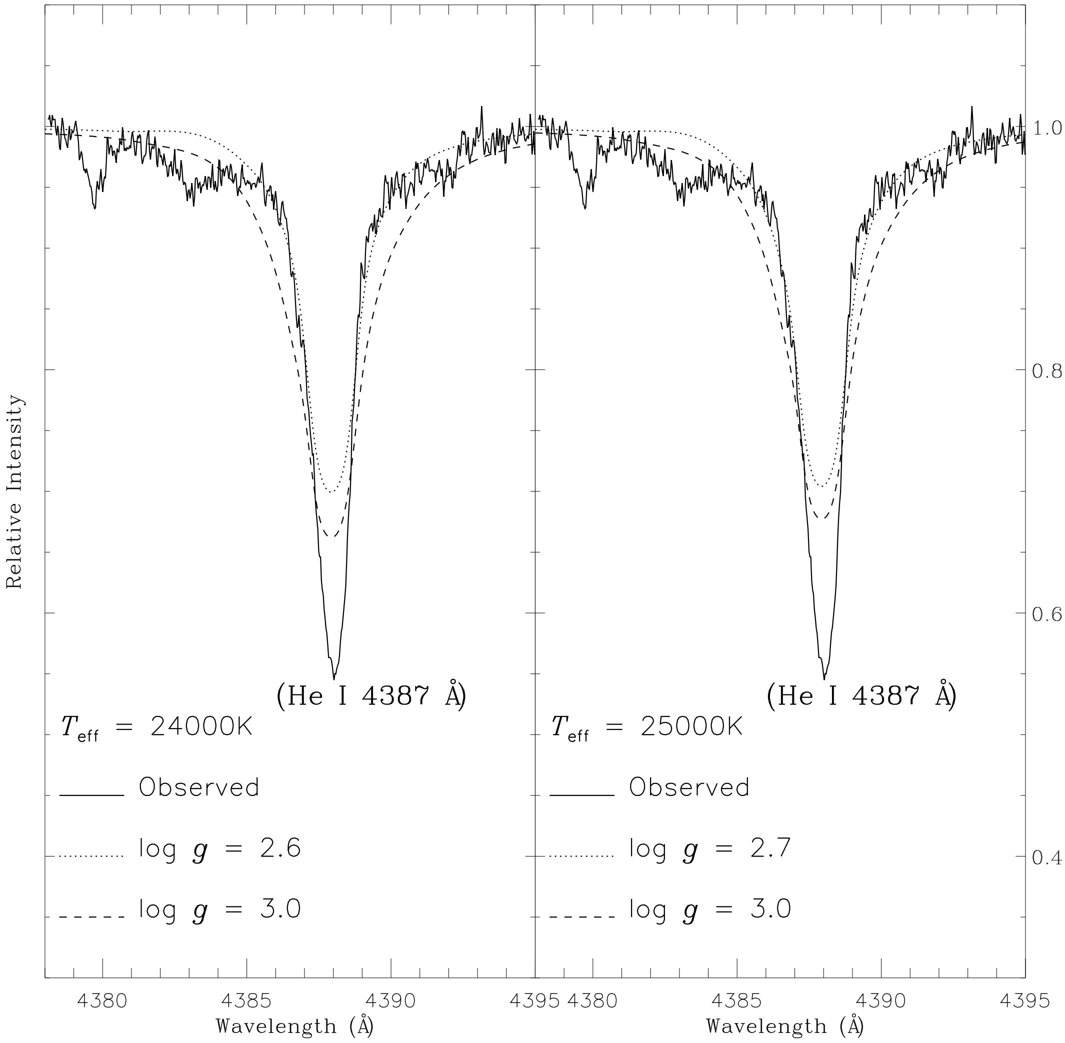

FIGURE 5.3: V2205 Oph's observed and synthesized LTE He I line profile at 4387 Å . In the left panel the LTE He I line profiles are synthesized for T$_{eff}$ = 24000 K for two different log g values. Similarly in the right panel the LTE He I line profiles are synthesized for T$_{eff}$ = 25000 K for two different log g – see key on both the panels.

same Figure, we see that the shift is more for the locus obtained from the lower ionic pairs than the higher ones:– Si II/Si III lies farthest whereas Si III/Si IV lies nearest to the other loci of C II/C III and N II/N III. This pattern is similar to the observed non-LTE effects in Ne by Pandey & Lambert (2011), where the lower ionic species (Ne I) suffers appreciable non-LTE effects than the higher one (Ne II). The Si III lines show a large line-to-line scatter (see Table-5.1). This may also arise due

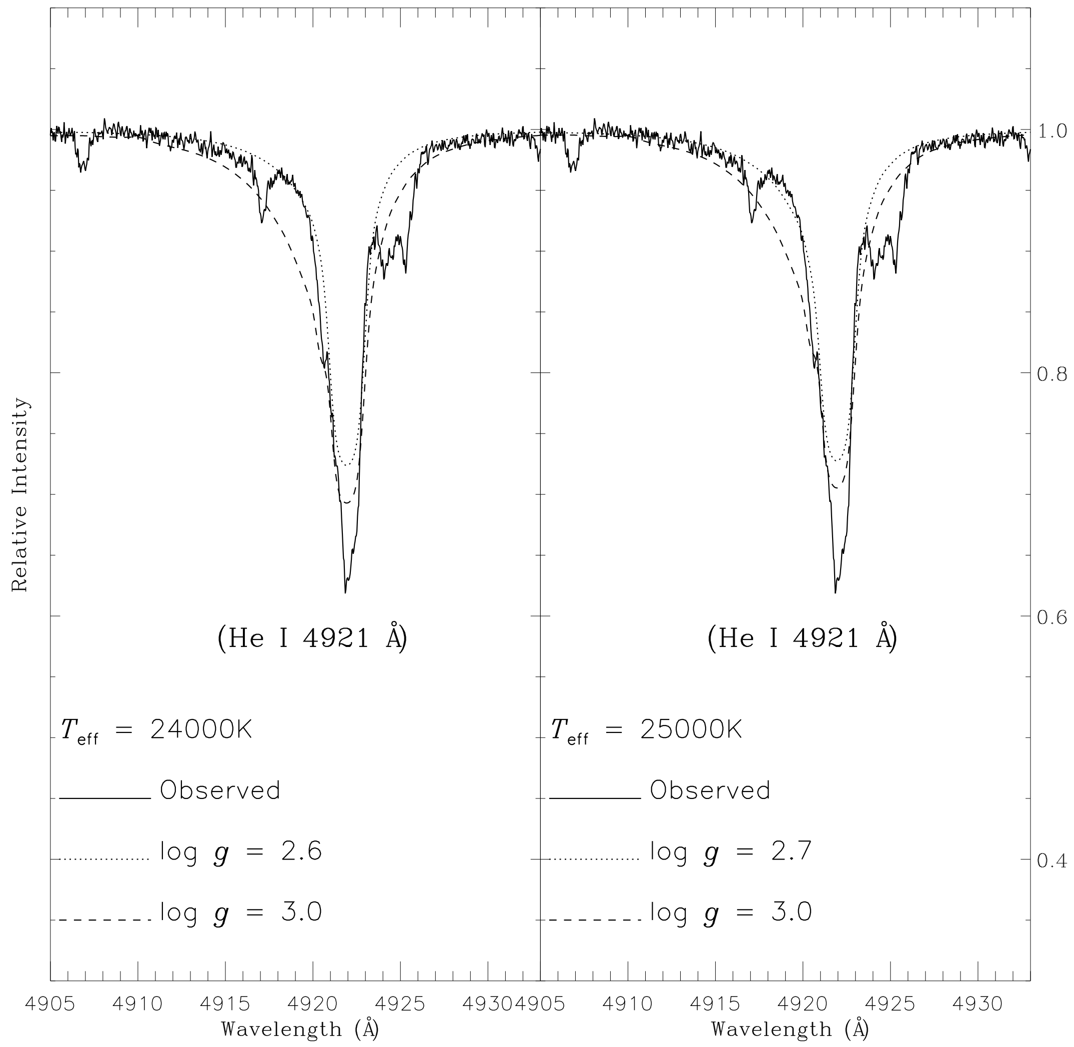

FIGURE 5.4: V2205 Oph's observed and synthesized LTE He I line profile at 4921 Å . In the left panel the LTE He I line profiles are synthesized for T$_{eff}$ = 24000 K for two different log g values. Similarly in the right panel the LTE He I line profiles are synthesized for T$_{eff}$ = 25000 K for two different log g – see key on both the panels.

to the potential non-LTE effects on Si III as commented by Jeffery & Heber (1992) who did not use Si III lines, for the LTE analysis of V2205 Oph. It is also evident from the loci involving Si II, that Si II lines are also affected by non-LTE. However, due to lack of model atoms of Si II in TLUSTY, non-LTE corrections of Si II lines for hot EHes is not readily available in the literature. One attempt was made by Kupfer et al. (2017) in their non-LTE analysis of the hot EHe BD +10° 2179,

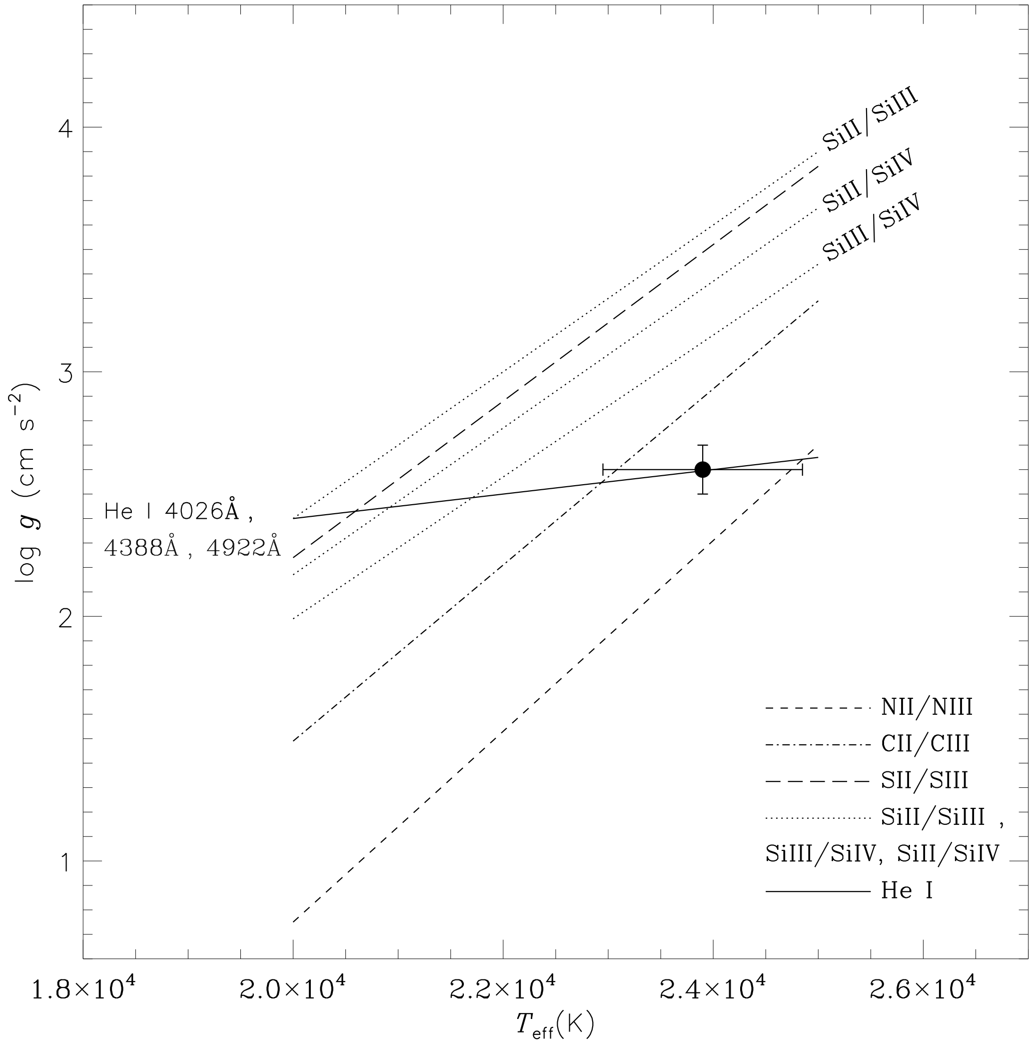

FIGURE 5.5: $\log g$ − T$_{eff}$ plane for V2205 Oph. Loci satisfying the ionization equilibrium are plotted–see the keys on the figure. The cross shows the adopted LTE atmospheric parameters, T$_{eff}$ = 23900 ± 900 K, $\log g$ = 2.65 ± 0.1 (cgs), used in this study.

which is about 7000 K cooler than our programmed star. As they do not report LTE analysis of BD +10° 2179, we can only compare with the LTE abundances reported by Pandey et al. (2006) with a different set of model atmospheres using different spectra. The comparative differences in abundances of different species in BD +10° 2179 obtained by Pandey et al. (2006) through their LTE analysis and Kupfer et al. (2017) by their non-LTE analysis are generally less than 0.3 dex. However, the difference in Si II abundances, obtained by Pandey et al. (2006)

and Kupfer et al. (2017) is $\sim$ 0.6 dex, which is close to the non-LTE correction for Ne I lines ($\sim$ 0.7 dex) for the hot EHes (Pandey & Lambert 2011). Hence we can assume Si II lines are also affected by non-LTE, both from the position of the loci in the $\log g$ − T$_{eff}$ plane and also from comparative literature study of non-LTE and LTE abundances. For determining the final solution for atmospheric parameters, the loci of all species that are subject to appreciable non-LTE effects are not considered. Hence the final LTE atmospheric parameters are determined using the loci defined by C II/C III, N II/N III and fits to the He I line profiles.

The final solution obtained from LTE analysis gives a value of T$_{eff}$ = 23900 ± 900 K , $\log g$ = 2.65 ± 0.1 (cgs) and ξ = 28 ± 2 kms^{-1}. This value is close to the one obtained by Pandey & Lambert (2011), (T$_{eff}$, $\log g$, ξ) = (24800, 2.85, 23), obtained from a different set of spectra and different equivalent widths. Note that, if we incorporate Jeffery & Heber's (1992) approach of including the ionization balance of Si II/Si IV and S II/S III for determining the final solution, we obtain, T$_{eff}$ = 22300 ± 1000 K , $\log g$ = 2.55 ± 0.2 (cgs) and ξ = 28 ± 2 kms^{-1} (see Figure-5.6) which is very similar to their adopted value (T$_{eff}$, $\log g$, ξ) = (22700 ± 1200 , 2.55 ± 0.1, 20 ± 5), even for a different set of spectra employing different model atmospheres. However, we choose to adopt the final value of (23900, 2.65, 28) for the reasons explained before and determine the elemental abundances for the said model.

5.4.2 Chemical composition

The abundance for all of the elements are derived for adopted model atmosphere (T$_{eff}$, $\log g$, ξ) = (23900, 2.65, 28). We report line-by-line LTE chemical abundances along with the measured equivalent width, including the final mean abundance and line-to-line scatter in Table-5.1. The line abundances reported in this study are measured from clean unblended lines. The lines of any species giving significantly deviant abundances are marked by the symbol * in Table-5.1 and are

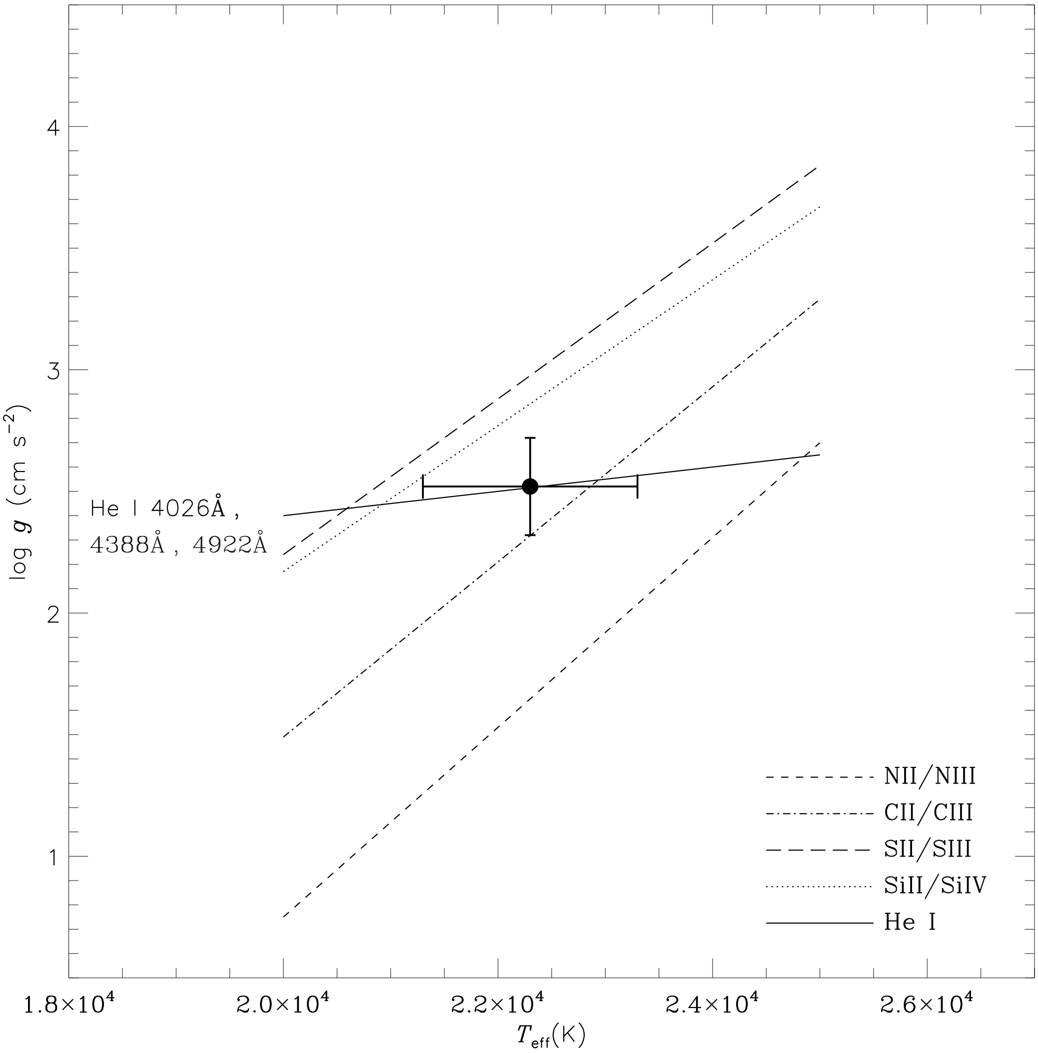

FIGURE 5.6: $\log g$ – T$_{eff}$ plane for V2205 Oph with the cross showing the solution, T$_{eff}$ = 22300 ± 1000 K, $\log g$ = 2.55 ± 0.2 (cgs) , obtained if Jeffery & Heber's (1992) procedure of including the ionization balance of Si II/Si IV and S II/S III lines is followed. The loci satisfying the ionization equilibrium are plotted–see the keys on the figure.

not considered for obtaining the final estimate of the mean. The abundance rms error due to uncertainty in T$_{eff}$ and $\log g$, from C II, C III, N II, N III, O II, Ne I, Ne II, Mg II, Al III, Si II, Si III, Si IV, Pi III, S II, S III, Ar II, Fe III are 0.04, 0.15, 0.07, 0.16, 0.02, 0.07, 0.08, 0.07, 0.06, 0.24, 0.05, 0.16, 0.05, 0.16, 0.01, 0.11, 0.08, respectively.

A comparison of the derived LTE abundances in this work with the measured LTE abundances reported by Pandey & Lambert (2011) and Jeffery & Heber (1992) is given Table-5.2. In the following, we discuss the selected identified elements from H to Fe and their derived abundances from Table-5.1 in light of the LTE studies reported by Pandey & Lambert (2011) and Jeffery & Heber (1992) (see-Table-5.2). Various RMT cited below refer to multiplet number of individual species obtained from Moore (1972).

TABLE 5.1: Photospheric LTE Line Abundances with the Line's Measured Equivalent Width (W_λ) in mÅ for V2205 Oph for the adopted model, (T_{eff}, $\log g$, ξ) = (23900, 2.65, 28)

Line	χ (eV)	log gf	W_λ (mÅ)	logϵ(X)
H I λ3970.072	10.20	-0.993	62	8.84
H I λ4101.734	10.20	-0.753	71	8.68
Mean				8.76 ± 0.10
C II λ3952.057^c	24.28	-0.210	60	9.18
C II λ3980.317^c	24.37	-0.210	52	9.08
C II λ4313.106	23.12	-0.373	92	9.30
C II λ4317.265	23.12	-0.005	155	9.30
C II λ4325.832	23.12	-0.373	···	···
C II λ4326.164	23.12	-0.407	131	9.21
C II λ4374.281^c	24.65	0.660	···	···
C II λ4375.008^c	24.66	-0.610	182	9.06
C II λ4411.152^c	24.60	0.530	···	···
C II λ4411.510^c	24.60	0.690	190	8.78
C II λ4625.639^c	24.79	0.700	72	8.47*
C II λ5035.943^c	20.92	-0.800	40	8.80
C II λ5119.462^c	25.07	0.010	65	9.22
C II λ5137.257	20.70	-0.911	125	9.13
C II λ5139.174	20.70	-0.707	165	9.23

Table 5.1 –*Continued*

Line	χ (eV)	log gf	W_λ (mÅ)	logϵ(X)
C II λ5143.495	20.70	-0.212	388	9.14
C II λ5145.165	20.71	0.189	442	9.20
C II λ5151.085	20.71	-0.179	323	9.75^*
Mean				9.13 ± 0.17
C III λ4067.940	39.92	0.720	84	8.79
C III λ4186.900	40.01	0.918	65	8.40^*
C III λ4515.352	39.40	-0.756	···	···
C III λ4515.811	39.40	-0.279	38	8.96
C III λ4516.788	39.40	-0.058	36	8.83
C III λ4647.418	29.53	0.070	322	8.92
C III λ4651.473	29.53	-0.629	221	9.07
C III λ4665.860	38.23	0.044	35	8.55^*
C III λ4673.953	38.23	-0.433	62	9.49^*
Mean				8.91 ± 0.11
N II λ3994.997	18.50	0.163	200	7.71
N II λ4227.736	21.60	-0.061	35	7.62
N II λ4447.030	20.41	0.228	89	7.55
N II λ4601.478	18.47	-0.452	104	7.87
N II λ4607.153	18.46	-0.522	92	7.87
N II λ4621.393	18.47	-0.538	96	7.91
N II λ4643.086	18.48	-0.371	115	7.84
N II λ4994.360	25.50	-0.164	···	···
N II λ4994.370	20.94	-0.098	34	7.49^*
N II λ5002.703	18.46	-1.022	48	7.71
N II λ5005.150	20.67	0.587	···	···
N II λ5005.300	25.50	-0.912	111	7.38^*
Mean				7.76 ± 0.13

Table 5.1 –*Continued*

Line	χ (eV)	log gf	W_λ (mÅ)	logϵ(X)
N III λ4103.39	27.44	-0.359	90	8.00
N III λ4200.07	36.86	0.250	13	7.90
Mean				7.95 ± 0.07
O II λ3945.038	23.42	-0.727	66	8.11
O II λ3954.362	23.42	-0.396	98	8.00
O II λ3973.256	23.44	-0.015	174	8.03
O II λ4078.842	25.64	-0.284	26	7.70
O II λ4085.112	25.65	-0.189	53	7.96
O II λ4092.929	25.67	-0.308	28	7.77
O II λ4104.724	25.84	-0.302	···	···
O II λ4104.990	25.84	-0.015	72	7.81
O II λ4119.217	25.85	0.452	100	7.73
O II λ4132.800	25.83	-0.065	55	7.90
O II λ4185.440	28.36	0.604	38	7.62
O II λ4303.615[c]	28.86	0.380	···	···
O II λ4303.833[c]	28.82	0.640	40	7.52
O II λ4336.859	22.98	-0.763	64	8.04
O II λ4345.560	22.98	-0.346	123	8.01
O II λ4349.426	23.00	0.060	205	8.01
O II λ4351.260	25.66	0.227	···	···
O II λ4351.457	25.66	-1.004	112	7.97
O II λ4366.895	23.00	-0.348	140	8.11
O II λ4395.935	26.25	-0.167	32	7.84
O II λ4414.899	23.44	0.172	196	7.96
O II λ4416.975	23.42	-0.077	150	7.99
O II λ4452.378	23.44	-0.788	52	8.06
O II λ4590.974	25.66	0.350	120	7.94

Table 5.1 –*Continued*

Line	χ (eV)	log gf	W_λ (mÅ)	logϵ(X)
O II λ4595.957	25.66	-1.033	···	···
O II λ4596.177	25.66	0.200	102	7.95
O II λ4641.810	22.98	0.055	221	8.09
O II λ4649.135	23.00	0.308	280	8.11
O II λ4661.632	22.98	-0.278	150	8.09
O II λ4676.235	23.00	-0.394	128	8.10
O II λ4699.011	28.51	0.418	···	···
O II λ4699.218	26.23	0.270	76	7.71
O II λ4705.346	26.25	0.477	85	7.73
O II λ4710.009	26.23	-0.225	44	8.07
O II λ4906.830	26.30	-0.161	24	7.73
O II λ4941.072	26.55	-0.053	37	7.89
O II λ4943.005	26.56	0.239	64	7.89
Mean				7.92 ± 0.16
Ne I λ5852.488	16.85	-0.490	19	8.63
Ne I λ6143.063	16.62	-0.100	73	8.86
Ne I λ6334.428	16.62	-0.320	48	8.86
Ne I λ6382.991	16.67	-0.240	49	8.81
Ne I λ6402.246	16.62	0.330	140	8.84
Mean				8.8 ± 0.10
Ne II λ4217.169^c	34.61	0.090	8	7.91
Ne II λ4322.368^c	37.89	-0.600	···	···
Ne II λ4322.372^c	37.89	0.360	···	···
Ne II λ4322.749^c	34.77	0.060	23	8.32*
Ne II λ4379.400	34.80	-0.340	···	···
Ne II λ4379.552	34.80	0.800	40	8.06
Ne II λ4413.217^c	34.86	0.520	15	7.86

Table 5.1 –*Continued*

Line	χ (eV)	log gf	W_λ (mÅ)	logϵ(X)
Ne II λ4430.905^c	34.83	0.070	···	···
Ne II λ4430.946^c	34.75	0.310	27	8.17
Ne II λ4442.686^c	34.84	0.030	10	8.16
Mean				8.03 ± 0.14
Mg II λ4481.126	8.86	0.749	···	···
Mg II λ4481.150	8.86	-0.553	···	···
Mg II λ4481.325	8.86	0.594	198	7.24
Al III λ4479.885^c	20.78	0.901	···	···
Al III λ4479.971^c	20.78	1.020	···	···
Al III λ4480.009^c	20.78	-0.530	45	5.70
Al III λ4512.565	17.81	0.410	30	5.67
Al III λ4528.945	17.82	-0.291	···	···
Al III λ4529.189	17.82	0.663	44	5.56
Al III λ5722.730	15.64	-0.071	99	6.29*
Mean				5.64 ± 0.07
Si II λ4128.054	9.84	0.360	145	8.37
Si II λ4130.872	9.84	-0.783	···	···
Si II λ4130.894	9.84	0.552	130	8.02
Mean				8.20 ± 0.25
Si III λ3924.468	25.40	0.858	190	7.29
Si III λ4338.500	19.02	-0.905	45	6.67*
Si III λ4567.840	19.02	0.068	485	7.94*
Si III λ4574.757	19.02	-0.409	358	7.78
Si III λ4683.021	28.12	0.135	···	···
Si III λ4683.794	28.09	-0.440	32	7.47
Si III λ4813.333	25.98	0.708	130	7.32
Si III λ4819.712	25.98	0.823	···	···

Table 5.1 –*Continued*

Line	χ (eV)	log gf	W_λ (mÅ)	logϵ(X)
Si III λ4819.814	25.98	-0.353	175	7.4
Si III λ4828.951	25.99	0.937	···	···
Si III λ4829.111	25.99	-0.354	180	7.32
Si III λ5739.734	19.72	-0.096	473	8.3*
Mean				7.43 ± 0.18
Si IV λ4116.104	24.05	-0.110	179	7.28
Si IV λ4212.396	36.14	0.380	···	···
Si IV λ4212.414	36.14	0.540	···	···
Si IV λ4212.414	36.14	-0.760	18	7.04
Si IV λ4654.312^c	36.43	1.130	···	···
Si IV λ4654.312^c	36.43	1.220	···	···
Si IV λ4654.312^c	36.43	-0.520	35	6.95
Mean				7.09 ± 0.17
P III λ3978.285^c	22.15	0.840	···	···
P III λ3978.341^c	22.15	0.950	···	···
P III λ3978.372^c	22.15	-0.590	55	5.90
P III λ4057.449	14.49	-1.040	42	6.24
P III λ4059.312	14.49	-0.050	150	5.96
P III λ4080.089	14.49	-0.310	90	5.90
P III λ4222.198	14.61	0.210	290	6.34
P III λ4246.720	14.61	-0.120	225	6.39
Mean				6.12 ± 0.23
S II λ4162.301	17.40	0.161	···	···
S II λ4162.665	15.94	0.780	98	7.91
S II λ4267.762	16.10	0.290	42	8.05
S II λ4294.402	16.13	0.580	65	7.99
S II λ4524.718	15.07	-0.746	···	···

Table 5.1 –*Continued*

Line	χ (eV)	log gf	W_λ (mÅ)	logϵ(X)
S II λ4524.941	15.07	0.033	42	7.99
S II λ4815.552	13.67	0.068	100	8.13
S II λ5009.567	13.62	-0.234	85	8.33
Mean				8.07 ± 0.15
S III λ3961.559	18.29	-1.177	64	7.34
S III λ3983.766	18.31	-0.590	120	7.13
S III λ3985.963	18.29	-0.856	100	7.27
S III λ3997.924	18.84	-1.108	39	7.14
S III λ4099.225	18.40	-1.430	56	7.55
S III λ4253.589	18.24	0.107	336	7.44
S III λ4284.979	18.19	-0.233	265	7.45
S III λ4332.692	18.19	-0.564	184	7.41
S III λ4354.566	18.31	-0.959	135	7.59
S III λ4361.527	18.24	-0.606	170	7.36
S III λ4364.747	18.32	-0.805	98	7.20
S III λ4418.836	18.24	-1.662	38	7.56
S III λ4499.245	18.29	-1.640	30	7.44
S III λ5219.322	18.40	-0.135	260	7.42
Mean				7.38 ± 0.15
Ar II λ4426.001	16.75	0.158	59	7.38
Ar II λ4735.906	16.64	-0.110	29	7.29
Ar II λ4806.021	16.64	0.210	69	7.39
Ar II λ4847.809	16.75	-0.220	38	7.55
Ar II λ4879.863	17.14	0.246	72	7.50
Mean				7.42 ± 0.10
Fe III λ4164.731[c]	23.61	0.923	···	···
Fe III λ4164.916[c]	27.63	1.011	37	6.68

Table 5.1 –*Continued*

Line	χ (eV)	log gf	W$_\lambda$ (mÅ)	logϵ(X)
Fe III λ5127.387^c	8.66	-2.218	···	···
Fe III λ5127.631^c	8.66	-2.564	35	6.81
Fe III λ5156.111^c	8.64	-2.018	42	6.85
Fe III λ5243.306^c	18.27	0.405	25	6.53
Mean				6.72 ± 0.14

[c] Kurucz gf-value

[*] Line omitted for mean abundance

Hydrogen. Most of the H-lines are affected by emission. The derived H abundance from the selected Balmer lines is 8.76, which is consistent with the LTE values obtained by Pandey & Lambert (2011) and Jeffery & Heber (1992).

Carbon. Carbon is well represented by both C II and C III lines. C II lines appear in the spectra as both absorption lines (in the blue) and emission lines (in the red). Significant number of clean C II absorption lines return the LTE line abundance 9.13 which differs by $\sim$ 0.1 dex from Pandey & Lambert's and Jeffery & Heber's determination. The derived C III LTE line abundances ignoring the three features at 4186.900 Å , 4665.860 Å , and 4673.953 Å returns a value of 8.9, consistent with Pandey & Lambert's determination but differing from Jeffery & Heber's value by $\sim$ 0.4 dex.

Nitrogen. The main contributor to nitrogen abundances are the abundances derived from N II lines with only two lines of N III detected. The LTE abundances returned by both N II and N III lines show a systematic offset of around $\sim$ 0.2 dex from the LTE values reported by Pandey & Lambert (2011) and Jeffery & Heber (1992).

Table 5.2: Comparison of stellar parameters and derived photospheric abundances from LTE analysis of V2205 Oph from different studies.

	This work	Pandey & Lambert (2011)	Jeffery & Heber (1992)
T_{eff} (K)	23900 ± 900	24800	22700 ± 1200
$\log g$ (cms^{-2})	2.65 ± 0.1	2.85	2.55 ± 0.1
ξ (kms^{-1})	28 ± 2	23	20 ± 5
H I	8.76 ± 0.10	8.79 ± 0.10	8.74 ± 0.08
C II	9.13 ± 0.17	9.22 ± 0.19	9.00 ± 0.22
C III	8.91 ± 0.11	8.99 ± 0.25	9.34 ± 0.38
N II	7.76 ± 0.13	7.95 ± 0.04	7.92 ± 0.12
N III	7.95 ± 0.07	8.14 ± 0.26	8.15 ± 0.18
O II	7.92 ± 0.16	7.95 ± 0.20	7.90 ± 0.21
Ne I	8.80 ± 0.10	8.78 ± 0.07	8.76 ± 0.09
Ne II	8.03 ± 0.14	8.03 ± 0.02	···
Mg II	7.24	···	7.25
Al III	5.64 ± 0.07	···	5.55 ± 0.11
Si II	8.20 ± 0.25	···	8.06 ± 0.13
Si III	7.43 ± 0.18	···	8.02 ± 0.61
Si IV	7.09 ± 0.17	···	7.61 ± 0.01
P III	6.12 ± 0.23	···	6.21 ± 0.31
S II	8.07 ± 0.15	···	7.93 ± 0.10
S III	7.38 ± 0.15	···	7.64 ± 0.13
Ar II	7.42 ± 0.10	···	7.24 ± 0.12
Fe III	6.72 ± 0.14	···	6.57 ± 0.36

Oxygen. A plethora of O II lines arising from several multiplets are detected in the spectrum. These lines return a mean LTE oxygen abundance of 7.92 which is consistent with the LTE oxygen abundances reported by both Pandey & Lambert (2011) and Jeffery & Heber (1992).

Neon. Neon is primarily represented by moderate to weak lines of Ne I with few weak lines of Ne II.
Ne I. Neutral Ne is represented by lines of weak to moderate strength from multiplets RMT 1, 3, and 6 in the red. The mean LTE Ne I abundance from these lines is consistent with LTE Ne I abundances obtained by both Pandey & Lambert (2011) and Jeffery & Heber (1992).
Ne II. Six very weak Ne II features from RMT 52, 56, 57 and 63 are detected in the spectrum. The mean LTE abundance obtained from this set of lines is 8.03 which is equal to Ne II abundance reported by Pandey & Lambert (2011).
The LTE Ne I and Ne II abundances shows a discrepancy of ~ 0.8 dex confirming the non-LTE effects on Ne I lines as demonstrated by Pandey & Lambert (2011).

Magnesium. Magnesium abundance is derived from the sole feature at 4481 Å (RMT 4), returning an LTE abundance of 7.24 consistent with Jeffery & Heber's determination.

Aluminium. Aluminium is represented in the spectra by four Al III lines from RMT 2, 3, and RMT 8. Except for the feature at 5722 Å (RMT 2), the mean LTE aluminium abundance is estimated to be 5.64 which differs from Jeffery & Heber's reported value by less than 0.1 dex. The Al III line at 5722 Å returns an LTE abundance of 6.29 which is more than 0.6 dex higher than the mean value, suggesting the presence of serious non-LTE effects.

Silicon. LTE silicon abundances derived in this work presents an interesting case. Silicon is represented in the spectra by three ionic stages–Si II, Si III, Si IV with Si III having the maximum contribution.
Si II. Most of the Si II lines are in emission in red, and hence the Si II abundances

are determined from the two detected absorption lines at 4128 Å and 4130 Å from RMT 3, giving a very high value of 8.20, similar to the one reported by Jeffery & Heber, 8.1.

Si III. The abundances derived from well-resolved Si III lines present a very curious scenario. The Si III line abundances have a large line-to-line scatter ranging from a minimum of 6.67 dex obtained from the RMT 3 line at 4338 Å, to a maximum of 8.3 dex obtained from the RMT 4 line at 5739 Å, a difference of 1.6 dex! This discrepancy may arise due to the presence of large non-LTE effects on the Si III lines as pointed by Jeffery & Heber who did not use Si III line abundances in their final analysis. The features centered at 4338 Å (RMT 3), 4567 Å (RMT 2), and 5739 Å (RMT 4) were not considered for the determination of final Si III abundances. The remaining lines from RMT 2, 9 and 13, gives a consistent Si III abundance of 7.43 dex with a scatter less than 0.2 dex. The derived Si III abundance is less than by a factor of 0.6 dex Jeffery & Heber's reported value. However, they also report a line-to-line scatter of 0.6 dex in their Si III abundance.

Si IV. Similar trend is noticed in abundance derived from Si IV lines. The derived Si IV line abundances give a mean value of 7.09 dex which is again 0.6 dex lower than that reported by Jeffery & Heber. Note that our Si IV line abundances are determined from three features centered at 4116 Å (RMT 1), 4212 Å (RMT 5), and 4654 Å (RMT 7). Another strong Si IV feature is present at 4088 Å (RMT 1), however, as it is heavily blended with an O II line of RMT 48, as noted by Jeffery & Heber, hence is not used for further analysis.

Phosphorus. Six P III features are observed arising from RMT 1, 3 and 8. The LTE phosphorus abundance obtained from these lines returns a mean value of 6.12, which is similar to Jeffery & Heber's P abundance, 6.21.

Sulphur. Sulphur is well represented in the spectrum by S II and S III lines.

S II. The main S II lines detected in the spectrum are from RMT 7, 9, 40, 43, 44 and 49. These lines gives an LTE abundance of 8.07 which is 0.1 dex higher than the abundance reported by Jeffery & Heber.

S III. The trend is reversed in case of S III lines where we obtain a mean abundance of 7.38, a value 0.3 dex lower than obtained by Jeffery & Heber. The S III lines used in the analysis are from RMT 4, 7, 8 and 9.
The difference between the abundances obtained from S II and S III lines is around $\sim$ 0.7 dex suggesting a possible presence of non-LTE effects on S II lines similar to that observed in Ne I. One of the principal reason, Jeffery & Heber's S II and S III abundances appear closer ($\sim$0.3 dex) than our analysis ($\sim$0.7 dex) is due to the fact that they used a model atmosphere having stellar parameters determined using S II and S III ionization equilibrium which we ignore in our determination.

Argon. Argon is detected in the form of five Ar II lines belonging to RMT 6, 7 and 14. The final Argon abundance obtained from these lines gives a mean value of 7.42, which is about 0.1 dex higher than the Argon abundance obtained by Jeffery & Heber.

Iron. Iron abundance is determined from four weak lines of Fe III in the spectrum belonging to RMT 5, 113 and 118, returning a value of 6.72 dex, a value 0.15 dex higher than Jeffery & Heber's adopted value. The $\log gf$ values are taken from Kurucz.

5.5 Conclusion

We have performed a detailed LTE fine analysis of high-quality spectra of the Extreme Helium Star – V2205 Oph. The atmospheric parameters derived in this work is in close agreement with the previous LTE analysis of Pandey & Lambert (2011); the star appears hotter and compact than Jeffery & Heber (1992)'s LTE analysis. Though we also obtain a higher microturbulence and lower rotational velocity than the previous two analysis. In terms of chemical composition, most of the derived abundances are similar to the abundances obtained by Pandey & Lambert (2011) and Jeffery & Heber (1992). In comparison with Pandey & Lambert's analysis involving five elements, H, C, N, O and Ne our abundances are pretty similar with maximum difference obtained in the estimates of nitrogen of about ~ 0.2 dex. While comparing our derived abundances with Jeffery & Heber's analysis, which reports abundances of twelve elements, H, C, N, O, Ne, Mg, Al, Si, P, S, Ar and Fe, the average difference is 0.2 dex with the notable exception of Si and S for which the difference is around 0.6 dex and 0.3 dex, respectively. The loci of ionization equilibrium and the abundance estimates suggest the presence of strong non-LTE effects on lines of Si II, Si III, and S II. Considering the assumption that the elements which remain unaffected by evolution mainly S, Si, and Fe, the high values of [Si/Fe] and [S/Fe] $>$ 1 dex obtained by Jeffery & Heber (1992) appears highly discrepant. Our results are an improvement on this aspect and show non-consideration of non-LTE effects on S and Si can result in such discrepancies. This makes a strong case for the need of a quantitative non-LTE analysis for elements beyond Ne, for V2205 Oph which is not reported in any earlier studies.

Chapter 6

Summary and Future prospects:

Summary:

This thesis represents observational studies of low mass hydrogen-deficient supergiants to explore evolutionary connections between them. Though two proposed formation scenarios existed–the FF scenario and the DD merger scenario, the evolutionary history of these exotic objects were shrouded in mystery until the fortuitous discovery of enhanced $^{12}C^{18}O$ in the NIR spectra of cool RCBs and HdCs by Clayton et al. (2007) and enriched F in the atmosphere of cool EHes and warm RCBs by Pandey (2006); Pandey et al. (2008). RCBs and HdCs were also characterised by weak ^{13}C in their spectra (Hema et al. 2012; Asplund et al. 2000). These detections convinced that these stars are evolutionarily connected and put considerable emphasis behind DD merger scenario as the principal source of formation. However, the information of such chemical peculiarities was incomplete across the entire sequence of these supergiants, mainly the coolest DY Persei variables and the hot Extreme Helium Stars (EHes). While the status of DY Persei variables as the cooler member of H-deficient supergiants or the H-normal cool carbon giants were not clear. Similarly, the status of F in hot EHes and the subsequent evolutionary connection with cool EHes and RCBs were not explored.

Hence we devoted our studies to these two extreme members of the group– the DY Persei variables and the hot EHes.

In the first part of the study, we explored the problem **"Are DY Per stars cooler cousins of RCBs?"** using the low-resolution NIR spectra of these objects to investigate the presence of enhanced ^{18}O in their atmospheres. Low ^{16}O/^{18}O and high ^{12}C/^{13}C is the principal feature of cool RCBs and HdCs. Whereas for H-normal stars, it is just the opposite. If DY Persei variables exhibit any of these features, then we can arrive at an idea about their nature. The entire exercise can be done by comparing band strengths of CO isotopic molecules like ^{12}C^{16}O, ^{12}C^{18}O and ^{13}C^{16}O which appears in the NIR region. IIA observing facilities at Indian Astronomical Observatory(IAO), Hanle, Ladakh, India provided the opportunity for low-resolution NIR studies using TIRSPEC mounted on the 2m Himalayan Chandra Telescope (HCT). The entire work is based on low-resolution NIR spectroscopic observations from this setup. Data had been collected in the period:2014 through 2017. As the number of observable true DY Per stars from this facility are few we also included DY Per suspects, a class of cool carbon stars which appears spectroscopically similar to DY Per stars, in our study. Obtaining a clear result from a low-resolution NIR spectroscopic study is difficult for these cool giants due to overcrowding of molecular features in their spectra. However, a comparative study with NIR spectra of RCBs and cool carbon giants would give an idea about the presence of such anomalies. Hence we also observed low-resolution NIR spectra of RCBs and H-normal cool carbon-rich AGBs. Our analysis confirmed the presence of strong ^{12}C^{18}O and no ^{13}C^{16}O bands in the spectra of RCB and HdC stars. Similarly, strong ^{13}C^{16}O and no ^{12}C^{18}O bands were observed in H-normal cool carbon-rich AGBs. For DY Persei and DY Persei suspects the result was mixed. Five of these stars including DY Persei itself, showed suggestions of ^{12}C^{18}O bands with no ^{13}C^{16}O in their spectra, which are the main spectroscopic signatures of RCBs and HdCs. However, two of the stars didn't show either detections. We attempted to determine lower limits to ^{16}O/^{18}O and ^{12}C/^{13}C ratios by comparing band strengths of CO and its isotopic molecules. The results of these abundance ratios for the observed RCBs, HdCs and cool carbon giants were found to be in line with those reported in the literature. While the observed RCBs and HdCs gave low ^{16}O/^{18}O and high ^{12}C/^{13}C ratios, the cool carbon giants showed low ^{12}C/^{13}C with no detection of ^{18}O. For the five DY Per affiliated stars which showed suggestions of ^{12}C^{18}O and no ^{13}C^{16}O bands, the abundance ratios conform to the values reported for the RCBs rather than the cool carbon stars. These results project that DY Per type stars maybe evolutionary connected with the RCBs, HdCs and other H-deficient supergiants. However, as the results were not uniform across the entire sample, high-resolution NIR studies for a greater number of DY Per samples are required to firmly classify these objects and establish whether these stars are the cooler cousins of RCBs or just a counterpart of normal carbon-rich AGBs.

In the second part of the project, we explored the **"Detection of fluorine in atmospheres of hot EHes"**. In the cool EHes enhanced F was detected in the form of neutral fluorine lines (F I) in the optical. If F being present in the atmosphere of hot EHes, it would be detected in the form of ionised fluorine lines mostly F II lines, due to their higher effective temperature. These lines appear at 3500Å and 3850Å window. Hence we obtained high resolution optical *é*chelle spectra of hot EHes using a number of telescope/spectrograph combination. This includes spectroscopic observations made using HESP mounted on HCT, IAO and data from ESO Archives. HESP observations were carried out in the period:2017 through 2018. 6 out of 10 hot EHes showed clear detection of F II. In order to obtain F estimates, F II lines of different abundances were synthesised for the corresponding model atmospheres of individual stars. F abundance corresponding to the best fit is obtained as the final result. The contribution of blending components, if present, were included for determining accurate F abundance estimates. Upper limits were obtained in those stars in which F II was not detected. The final F estimates obtained, show F is enhanced relative to Fe by a factor of 100−10000 times than those for normal stars. This result is perfectly in line to those obtained for cool EHes and warm RCBs, placing all three of them – the RCBs, cool EHes and hot EHes firmly in a common evolutionary sequence. These hot stars are susceptible to non-LTE effects, and a prime example was abundance mismatch between LTE abundances of neutral Ne (Ne I) and singly ionised Ne lines (Ne II) by 0.8 dex, as reported by Pandey & Lambert (2011). We suspected the atomic structure of F being very similar to Ne might also suffer from the said non-LTE effects. Hence to check for the presence of non-LTE effects in F II lines, abundance estimates from F I lines were also obtained for the coolest members of the hot EHe group in which both F I and F II lines lines were visible. The abundance estimates of F from F I matches closely with those obtained from F II lines, effectively ruling out non-LTE effects. Even if non-LTE effects were present, the level of F overabundances is too high, 100-10000 times, compared to the non-LTE correction factor which is less than a factor 10. Hence, the enhancement of F in hot EHes are not in doubt, effectively solving the decades-old mystery surrounding their formation and composition. It is established that the RCBs, cool EHes and hot EHes are evolutionarily connected and the DD merger scenario is the most probable formation scenario of these enigmatic objects as it successfully predicts F overabundances (Menon et al. 2013; Menon et al. 2019; Lauer et al. 2019). While the observed trends of F with other elemental abundances did not throw much light into the nucleosynthetic processes that result in F-enrichment, yet the trend of N with Ne and its connection with F enrichment was a startling discovery. The observed N in the majority of the hot EHes is the end product of the CNO cycle during H-burning at early stages of evolution of the merger progenitors. Whereas the observed Ne in the majority of the hot EHes indicate that Ne is a direct result of a complete conversion of CNO processed N through successive α captures during He-burning. Moreover, we also note that F is enriched in only those hot EHes in which Ne is enhanced and is a result of a complete conversion of N. One of the principal nucleosynthetic channels proposed by Menon et al. (2013) for F enrichment during DD mergers is – F is produced from neutron captures on N. Hence this dilemma of simultaneous enhancement of F and Ne without any visible depletion of N is a burning question that needs to be explored through further theoretical simulations.

In the third project, we performed a **"Quantitative analysis of the Extreme Helium Star, V2205 Oph"**. The optical high-resolution spectroscopic data is obtained using HESP during the period from 2017 to 2018. Through quantitative fine analysis, we determine the atmospheric parameters and corresponding chemical abundances. Using a grid of LTE model atmospheres, we determine the atmospheric parameters of V2205 Oph, from the imposition of ionization balance of ion pairs such as C II/C III and N II/N III and using spectroscopic indicators like He I line profiles. The adopted stellar parameters: T_{eff} = 23900 ± 900 K, $\log g$ = 2.65 ± 0.1 (cgs) and ξ = 28 ± 2 kms^{-1}, is very close to the LTE parameters obtained by Pandey & Lambert (2011). We derive a higher microturbulence and lower rotational velocity than the earlier two studies of (Jeffery & Heber 1992; Pandey & Lambert 2011). We report LTE chemical abundances of 12 elements from H to Fe, which mostly agrees with the previous two studies. However, the loci of the ionization equilibrium for the Si and S ions in the $\log g - T_{eff}$ plane, suggest departures from LTE. The abundance analysis confirms this fact, with ions belonging to the same species of Si and S showing significant abundance difference of more than 0.5 dex. Based on the prevalent assumption, that the elements which remain unaffected by evolution are mainly S, Si, and Fe yet Jeffery & Heber (1992) obtain a high value of [Si/Fe] and [S/Fe], > 1 dex. Our results lead to the inference that non-consideration of non-LTE effects on Si and S can give rise to such discrepant abundances as reported by Jeffery & Heber (1992). Hence a dedicated non-LTE analysis for elements beyond Ne, for V2205 Oph is needed.

Through this work, dedicated mainly towards the two extreme members of the group, we firmly establish evolutionary connections along the entire sequence of H-deficient supergiants – the DY Pers, the HdCs, the RCBs, the cool and hot EHes. Though few questions remain for the individual star types, it can be rightly inferred from the observational studies that DD merger scenario is the principal formation scenario of these exotic objects.

Future prospects:

The studies in this thesis opened up a scope for further studies in many important areas.

- **High-resolution studies of NIR spectra of DY Persei variables**. From the low-resolution NIR studies we got an idea that DY Per stars maybe related to cool RCBs and HdCs through the suggestions of $^{12}C^{18}O$ in their spectra. However, the level of ^{18}O enhancement can only be accurately determined through high resolution studies of DY Persei stars. The NIR spectra of cool DY Pers are rich in molecular features. Especially the *K*-band region of NIR, centred around 2.2 μm is a valuable window for several spectroscopic studies of these cool stars. The rovibrational band heads of $^{12}C^{16}O$, $^{12}C^{18}O$ and $^{13}C^{16}O$ appear in this region which can be used for determination $^{16}O/^{18}O$ and $^{12}C/^{13}C$ ratios. Due to the high flux in the NIR region for such cool stars any abundance determinations made from this region will be accurate. The *K* band region also contains the elusive HF (1-0) R9 line at 2.3357 μm from which the fluorine abundances of normal H-rich stars are determined. If the HF line is detected in the spectra of DY Persei variables it can potentially answer two questions– i) the level of hydrogen in the atmosphere of these stars which is difficult to determine from the optical spectra due to the absence of H Balmer lines and CH bands due to the stars having cooler effective temperatures and ii) F abundance estimates, whether it conforms to enhanced F in RCBs and EHes or more like normal cool-carbon giants. Hence, the high resolution *K*-band spectroscopy can potentially answer all three pertinent problems related to DY Persei variables– 1) the status of $^{16}O/^{18}O$ and $^{12}C/^{13}C$ abundance ratios – 2) the status of H-deficiency in these stars and finally, 3) the status of fluorine abundances in light of the other H-deficient supergiants.

- **Investigating the non-LTE effects on F abundances through the determination of F II and F III abundances for the hotter EHes.** The non-LTE effects on F II for cooler members of the hot EHe group was successfully ruled out by comparison of F I and F II abundance estimates. However, the same was not obtainable for the hotter members of the group due to the absence of F I lines. But in these hot stars having enriched fluorine, it can appear as both F II lines in optical blue and F III lines in UV. The determinations of F III as well as the F II abundances can be used for determining the level of non-LTE effects on F abundance of these stars. Moreover, the exploration of F enrichment in the entire sample of 22 EHes is not complete due to the lack of high-resolution observational analysis for all the sample stars. The results from the ten hot EHes and five cool EHes put firm constraints regarding F enrichment in these stars. A complete survey along the entire sample will test the applicability of such constraints.

- **Exploration of F in hot H-deficient subdwarfs.** Fluorine is found to be enhanced across the majority sample of hot and cool EHes and RCBs which are essentially H-deficient supergiants. Werner et al. (2005) found enhanced F in the form of F V and F VI lines in the PG 1159 stars which are a type of H-deficient central stars of Planetary Nebulae. Lying between these two H-deficient star groups belonging to two distinct evolutionary stages are the H-deficient hot subdwarfs. The investigation of F in the hot H-deficient subdwarfs will enable us to explore the connections between H-deficient star groups belonging to different evolutionary stages.

- **Investigating the non-LTE effects on Ne I lines in cool EHes**. The analysis of Pandey & Lambert (2011) showed pronounced non-LTE effects on Ne I lines in hot EHes. The non-LTE correction factor is about 0.8 dex from the LTE Ne I abundances. For cool EHes, the observed abundances of Ne are determined from LTE analysis of Ne I lines. From the Ne vs Fe plot in Chapter 4-Figure 4.17 it is clear that there is a systematic offset between the Ne abundances of cool EHes derived from LTE analysis of Ne I lines with those of the hot EHes, determined from non-LTE analysis of Ne I and Ne II lines. This systematic offset of Ne abundances for cool EHes can be attributed to non-LTE effects on Ne I lines and a predicted correction of 0.8 dex (determined for hot EHes) brings the Ne abundance down and places them in the region of hot EHes. Similar for the case of few warm RCBs for which Ne abundance is reported from LTE analysis of Ne I lines. Hence it is clear non-LTE effects on Ne I lines in cool EHes and RCBs are pronounced and an accurate determination is the need of the hour. If for cool EHes and RCBs, Ne overabundances are an effective addition to the list of abundance anomalies, reliable estimates are necessary. The new non-LTE corrected Ne abundances for cool EHes and RCBs will join other abundances as a probe to explore the evolutionary origins of the H-deficient supergiants.

Bibliography

Abbott, D. C. & Conti, P. S. 1987, ARA&A, 25, 113. doi:10.1146/annurev.aa.25.090187.000553

Ahmad, A. & Jeffery, C. S. 2004, A&A, 413, 323

Alcock, C., Allsman, R. A., Alves, D. R., et al. 2001, ApJ, 554, 298

Alksnis, A. 1994, Baltic Astronomy, 3, 410

Althaus, L. G. & Benvenuto, O. G. 1997, ApJ, 477, 313

Asplund, M., Gustafsson, B., Lambert, D. L., et al. 1997, A&A, 321, L17

Asplund, M., Gustafsson, B., Kameswara Rao, N., et al. 1998, A&A, 332, 651

Asplund, M., Gustafsson, B., Lambert, D. L., et al. 2000, A&A, 353, 287

Berman, L. 1935, ApJ, 81, 369

Bhowmick, A., Pandey, G., Joshi, V., et al. 2018, ApJ, 854, 140. doi:10.3847/1538-4357/aaaae4

Bhowmick, A., Pandey, G., & Lambert, D. L. 2020, ApJ, 891, 40. doi:10.3847/1538-4357/ab6e6d

Bhowmick, A., Pandey, G. 2021, ApJ, (under preparation)

Bowers, R. L. & Deeming, T. 1984, Research supported by the University of Texas, Los Alamos National Laboratory, and Digicon Geophysical Corp. Boston, MA, Jones and Bartlett Publishers, Inc., 1984, 378 p.

Cameron, A. G. W. & Fowler, W. A. 1971, ApJ, 164, 111

Clayton, G. C. 1996, PASP, 108, 225

Clayton, G. C. & De Marco, O. 1997, AJ, 114, 2679

Clayton, G. C., Herwig, F., Geballe, T. R., et al. 2005, ApJ, 623, L141

Clayton, G. C., Kerber, F., Pirzkal, N., et al. 2006, ApJ, 646, L69

Clayton, G. C., Geballe, T. R., Herwig, F., Fryer, C., & Asplund, M. 2007, ApJ, 662, 1220

Clayton, G. C., Sugerman, B. E. K., Stanford, S. A., et al. 2011, ApJ, 743, 44

Clayton, G. C. 2012, Journal of the American Association of Variable Star Observers (JAAVSO), 40, 539

Clayton, G. C., Bond, H. E., Long, L. A., et al. 2013, ApJ, 771, 130. doi:10.1088/0004-637X/771/2/130

Crawford, C. L., Clayton, G. C., Munson, B., et al. 2020, MNRAS, 498, 2912. doi:10.1093/mnras/staa2526

Cutri, R. M., Skrutskie, M. F., van Dyk, S., et al. 2003, 2MASS All Sky Catalog of point sources.

Duerbeck, H. W., Liller, W., Sterken, C., et al. 2000, AJ, 119, 2360

Drilling, J. S. & Hill, P. W. 1986, IAU Colloq. 87: Hydrogen Deficient Stars and Related Objects, 499

Drilling, J. S. & Bergeron, L. E. 1995, PASP, 107, 846. doi:10.1086/133631

Drilling, J. S. 1996, Hydrogen Deficient Stars, 96, 461

Drilling, J. S., Jeffery, C. S., & Heber, U. 1998, A&A, 329, 1019

Drilling, J. S., Moehler, S., Jeffery, C. S., et al. 2003, The Garrison Festschrift, 27

Eyres, S. P. S., Evans, A., Geballe, T. R., et al. 1998, MNRAS, 298, L37

Feast, M. W., Carter, B. S., Roberts, G., et al. 1997, MNRAS, 285, 317

Fleming, W. P. 1891, Astronomische Nachrichten, 126, 165.

Fujimoto, M. Y. 1977, PASJ, 29, 331

García-Hernández, D. A., Hinkle, K. H., Lambert, D. L., & Eriksson, K. 2009, ApJ, 696, 1733

García-Hernández, D. A., Lambert, D. L., Kameswara Rao, N., Hinkle, K. H., & Eriksson, K. 2010, ApJ, 714, 144

García-Hernández, D. A., Zamora, O., Yagüe, A., et al. 2013, A&A, 555, L3

Geiss, J., Gloeckler, G., & Charbonnel, C. 2002, ApJ, 578, 862

Gonzalez, G., Lambert, D. L., Wallerstein, G., et al. 1998, ApJS, 114, 133

Goswami, A. & Reddy, B. E. 2010,Principles and Perspectives in Cosmochemistry: Lecture Notes of the Kodai School on 'Synthesis of Elements in Stars' held at Kodaikanal Observatory, India, April 29 - May 13, 2008, Astrophysics and Space Science Proceedings, 16

Goswami, A., Karinkuzhi, D., & Shantikumar, N. S. 2010, ApJ, 723, L238

Green, R. F., Schmidt, M., & Liebert, J. 1986, ApJS, 61, 305

Greenstein, J. L. 1940, ApJ, 91, 438

Guerço, R., Cunha, K., Smith, V. V., et al. 2019, ApJ, 876, 43

Hajduk, M., Zijlstra, A. A., Herwig, F., et al. 2005, Science, 308, 231

Hema, B. P., Pandey, G., & Lambert, D. L. 2012a, ApJ, 747, 102

Hema, B., Pandey, G., & Lambert, D. L. 2012b, Nuclei in the Cosmos (NIC XII), 195

Hema, B. P., Pandey, G., Kamath, D., et al. 2017, PASP, 129, 104202

Herwig, F., Blöcker, T., Langer, N., et al. 1999, A&A, 349, L5

Herwig, F. & Langer, N. 2001, Nucl. Phys. A, 688, 221

Herwig, F. 2001, Ap&SS, 275, 15

Herwig, F. 2005, ARA&A, 43, 435

Herzberg, G. 1950, Molecular spectra and molecular structure. Vol.1: Spectra of diatomic molecules

Hubeny, I., Lanz, T., & Jeffery, C. 1994, Newsletter on Analysis of Astronomical Spectra (Univ. of St. Andrews)

Hunger, K. & Groote, D. 1999, A&A, 351, 554

Iben, I. 1974, ARA&A, 12, 215

Iben, I., Jr., Kaler, J. B., Truran, J. W., & Renzini, A. 1983, ApJ, 264, 605

Iben, I. & Renzini, A. 1983, ARA&A, 21, 271

Iben, I., Jr., & Tutukov, A. V. 1984, ApJS, 54, 335

Iben, I. 1990, ApJ, 353, 215

Iben, I. & MacDonald, J. 1995, White Dwarfs, 48

Jeffery, C. S., Drilling, J. S., & Heber, U. 1987, MNRAS, 226, 317

Jeffery, C. S., Heber, U., Hill, P. W., et al. 1988, MNRAS, 231, 175. doi:10.1093/mnras/231.2.175

Jeffery, C. S. & Heber, U. 1992, A&A, 260, 133

Jeffery, C. S. 1993, A&A, 279, 188

Jeffery, C. S. & Heber, U. 1993, A&A, 270, 167

Jeffery, C. S., Heber, U., Hill, P. W., et al. 1996, in Astronomical Society of the Pacific Conference Series, Vol. 96, Hydrogen Deficient Stars, ed. C. S. Jeffery & U. Heber, 471

Jeffery, C. S. 1998, MNRAS, 294, 391

Jeffery, C. S. & Aznar Cuadrado, R. 2001, A&A, 378, 936

Jeffery, C. S. 2008, Hydrogen-Deficient Stars, 391, 3

Jeffery, C. S. 2008, Hydrogen-Deficient Stars, 391, 53

Jeffery, C. S., Karakas, A. I., & Saio, H. 2011, MNRAS, 414, 3599

Jeffery, C. S. 2014, Precision Asteroseismology, 301, 297

Jeffery, C. S. 2017, MNRAS, 470, 3557

Jeffery, C. S., Rao, N. K., & Lambert, D. L. 2020, MNRAS, 493, 3565. doi:10.1093/mnras/staa406

Jönsson, H., Ryde, N., Harper, G. M., et al. 2014, ApJ, 789, L41

Jönsson, H., Ryde, N., Spitoni, E., et al. 2017, ApJ, 835, 50

Jorissen, A., Smith, V. V., & Lambert, D. L. 1992, A&A, 261, 164

Keenan, P. C., & Barnbaum, C. 1997, PASP, 109, 969

Kelleher, D. E. & Podobedova, L. I. 2008a, Journal of Physical and Chemical Reference Data, 37, 1285. doi:10.1063/1.2734566

Kelleher, D. E. & Podobedova, L. I. 2008b, Journal of Physical and Chemical Reference Data, 37, 709. doi:10.1063/1.2734564

Kupfer, T., Przybilla, N., Heber, U., et al. 2017, MNRAS, 471, 877

Kwok, S. 2000, The origin and evolution of planetary nebulae / Sun Kwok. Cambridge ; New York : Cambridge University Press, 2000. (Cambridge astrophysics series ; 33)

Lambert, D. L. 1986, IAU Colloq. 87: Hydrogen Deficient Stars and Related Objects, 127

Lattanzio, J. & Forestini, M. 1999, Asymptotic Giant Branch Stars, 191, 31

Lauer, A., Chatzopoulos, E., Clayton, G. C., Frank, J., & Marcello, D. C. 2019, MNRAS, 488, 438

Li, H. N., Ludwig, H.-G., Caffau, E., et al. 2013, ApJ, 765, 51

Lisker, T., Heber, U., Napiwotzki, R., et al. 2004, Ap&SS, 291, 351

Lockyer, J. N. 1868, Proceedings of the Royal Society of London Series I, 17, 91

Lodders, K., Palme, H., & Gail, H.-P. 2009, Landolt Börnstein, 712

Longland, R., Lorén-Aguilar, P., José, J., et al. 2011, ApJ, 737, L34

Ludendorff, H. 1906, Astronomische Nachrichten, 173, 1

Lundmark, K. 1921, PASP, 33, 314

Luyten, W. J. 1945, ApJ, 101, 131

Maiorca, E., Uitenbroek, H., Uttenthaler, S., et al. 2014, ApJ, 788, 149

Mantz, A. W., Maillard, J.-P., Roh, W. B., & Narahari Rao, K. 1975, Journal of Molecular Spectroscopy, 57, 155

Menon, A., Herwig, F., Denissenkov, P. A., et al. 2013, ApJ, 772, 59

Menon A., Karakas A. I., Lugaro M., Doherty C. L., Ritter C., 2019, MNRAS, 482, 2320

Mendez, R. H., Herrero, A., Manchado, A., et al. 1991, A&A, 252, 265

Mendez, R. H. 1991, Evolution of Stars: the Photospheric Abundance Connection, 145, 375

Miller, A. A., Richards, J. W., Bloom, J. S., et al. 2012, ApJ, 755, 98

Moore, C. E. 1972, A multiplet table of astrophysical interest - Pt.1: Table of multiplets - Pt.2: Finding list of all lines in the table of multiplets

—. 1993, Tables of Spectra of Hydrogen, Carbon, Nitrogen, and Oxygen Atoms and Ions

Naslim, N., Jeffery, C. S., Ahmad, A., et al. 2010, MNRAS, 409, 582

Nault, K. A., & Pilachowski, C. A. 2013, AJ, 146, 153

Nousek, J. A., Shipman, H. L., Holberg, J. B., et al. 1986, ApJ, 309, 230

Ninan, J. P., Ojha, D. K., Ghosh, S. K., et al. 2014, Journal of Astronomical Instrumentation, 3, 1450006

Öberg, K. J. 2007, European Physical Journal D, 41, 25

Ohayon, B., Rahangdale, H., Geddes, A. J., et al. 2019, Phys. Rev. A, 99, 042503

Pavlenko, Y. V., Geballe, T. R., Evans, A., et al. 2004, A&A, 417, L39

Pandey, G., Kameswara Rao, N., Lambert, D. L., Jeffery, C. S., & Asplund, M. 2001, MNRAS, 324, 937

Pandey, G., Lambert, D. L., Rao, N. K., et al. 2004, ApJ, 602, L113

Pandey, G., Lambert, D. L., Jeffery, C. S., & Rao, N. K. 2006, ApJ, 638, 454

Pandey, G., & Reddy, B. E. 2006, MNRAS, 369, 1677

Pandey, G. 2006, ApJ, 648, L143

Pandey, G., Lambert, D. L., & Kameswara Rao, N. 2008, ApJ, 674, 1068

Pandey, G., & Lambert, D. L. 2011, ApJ, 727, 122

Pandey, G., Kameswara Rao, N., Jeffery, C. S., & Lambert, D. L. 2014, ApJ, 793, 76

—. 2017, ApJ, 847, 127

Payne-Gaposchkin, C., & Gaposchkin, S. 1938, Harvard Observatory Monographs, 5

Percy, J. R., Bandara, K., Fernie, J. D., et al. 2004, Journal of the American Association of Variable Star Observers (JAAVSO), 33, 27

Podobedova, L. I., Kelleher, D. E., & Wiese, W. L. 2009, Journal of Physical and Chemical Reference Data, 38, 171. doi:10.1063/1.3032939

Popper, D. M. 1942, PASP, 54, 160

Rao, N. K. & Lambert, D. L. 1996, Hydrogen Deficient Stars, 96, 43

Kameswara Rao, N., Lambert, D. L., Adams, M. T., et al. 1999, MNRAS, 310, 717

Rao, N. K. & Lambert, D. L. 2008, MNRAS, 384, 477

Ramsay, G., Hakala, P., & Cropper, M. 2002, MNRAS, 332, L7

Rauch, T., Dreizler, S., & Wolff, B. 1998, A&A, 338, 651

Renzini, A. 1979, in Astrophysics and Space Science Library, Vol. 75, Stars and star systems, ed. B. E. Westerlund, 155–171

Renzini, A. 1990, Confrontation Between Stellar Pulsation and Evolution, 11, 549

Ryde, N., & Lambert, D. L. 2004, A&A, 415, 559

Saio, H., & Jeffery, C. S. 2002, MNRAS, 333, 121

Salaris, M. & Cassisi, S. 2005, Evolution of Stars and Stellar Populations, by Maurizio Salaris, Santi Cassisi, pp. 400. ISBN 0-470-09220-3. Wiley-VCH , December 2005., 400

Schonberner, D. 1996, Hydrogen Deficient Stars, 96, 433

Shamey, L. J. 1969, Ph.D. Thesis

Solheim, J. E. 1996, Hydrogen Deficient Stars, 96, 309

Solheim, J.-E. 2010, PASP, 122, 1133

Soszyński, I., Udalski, A., Szymański, M. K., et al. 2009, Acta Astron., 59, 335

Sriram, S., Kumar, A., Surya, A., et al. 2018, Proc. SPIE, 107026K

Stalin, C. S., Hegde, M., Sahu, D. K., et al. 2008, Bulletin of the Astronomical Society of India, 36, 111

Struve, O. & Sherman, F. 1940, ApJ, 91, 428

Tanaka, M., Letip, A., Nishimaki, Y., et al. 2007, PASJ, 59, 939

Tisserand, P., Marquette, J. B., Beaulieu, J. P., et al. 2004, A&A, 424, 245

Tisserand, P., Marquette, J. B., Wood, P. R., et al. 2008, A&A, 481, 673

Tisserand, P., Wood, P. R., Marquette, J. B., et al. 2009, A&A, 501, 985

Tisserand, P. 2012, A&A, 539, A51

Tisserand, P., Clayton, G. C., Welch, D. L., et al. 2013, A&A, 551, A77

Tisserand, P., Clayton, G. C., Bessell, M. S., et al. 2020, A&A, 635, A14

Tull, R. G., MacQueen, P. J., Sneden, C., & Lambert, D. L. 1995, PASP, 107, 251

van der Hucht, K. A. 2001, New A Rev., 45, 135

van Genderen, A. M. & Gautschy, A. 1995, A&A, 294, 453

Wolff, S. C., Pilachowski, C. A., & Wolstencroft, R. D. 1974, ApJ, 194, L83

Warner, B. 1967, MNRAS, 137, 119

Webbink, R. F. 1984, ApJ, 277, 355

Werner, K., Rauch, T., Barstow, M. A., et al. 2004, A&A, 421, 1169

Werner, K., Rauch, T., & Kruk, J. W. 2005, A&A, 433, 641. doi:10.1051/0004-6361:20042258

Wiese, W. L., Smith, M. W., & Glennon, B. M. 1966, Atomic transition probabilities. Vol.: Hydrogen through Neon. A critical data compilation

Wolf, C. J. E. & Rayet, G. 1867, Academie des Sciences Paris Comptes Rendus, 65, 292

Wesemael, F., Greenstein, J. L., Liebert, J., et al. 1993, PASP, 105, 761

Zhang, X., & Jeffery, C. S. 2012a, MNRAS, 419, 452

Zhang, X., & Jeffery, C. S. 2012b, MNRAS, 426, L81

Zhang, X. & Jeffery, C. S. 2012, MNRAS, 419, 452. doi:10.1111/j.1365-2966.2011.19711.x

Zhang, X., Jeffery, C. S., Chen, X., & Han, Z. 2014, MNRAS, 445, 660

Yakovina, L. A., Pugach, A. F., & Pavlenko, Y. V. 2009, Astronomy Reports, 53, 187

Začs, L., Mondal, S., Chen, W. P., et al. 2007, A&A, 472, 247